LUND UNIVERSITY

Quantum Optical Description of High-order Harmonic Generation

Isabel Moreno Babuglia

Thesis submitted for the degree of Master of Science
Project duration: 3.5 months

Supervised by David Busto and Anne L'Huillier

Department of Physics
Division of Atomic Physics
December 2023

Abstract

High-order Harmonic Generation (HHG) is a highly non-linear process in which an atom interacts with a strong laser field. The laser field lowers the atomic potential barrier allowing bound electrons to escape into the continuum through tunnel ionization, propagate, and, with some probability, recombine with the parent ion. As a result, coherent eXtreme UltraViolet (XUV) radiation is emitted in the form of ultrashort pulses with attosecond durations. This phenomenon has been successfully described with semi-classical models that consider the atoms as quantum systems and the radiation as a classical wave. However, there have been recent efforts to develop a fully quantum mechanical theory of HHG in which the radiation is also described as a quantum system. This quantum optical description has opened the doors to several applications of HHG radiation in quantum technology and fundamental physics research. In this thesis work, the newly developed Strong Field Quantum Electrodynamics (SFQED) theory applied to HHG is reviewed. The effects of considering a spatial distribution for the atoms and radiation's intensity are investigated using this framework. To do this, two Python simulations, where SFQED and the Strong Field Approximation (SFA) are used, were created. One of them considers single atom generation, and the other one considers few atoms generation using a Gaussian beam intensity profile. It is found that the spatial distribution affects the shape of the spectrum, but does not affect the final radiation state's statistics or purity. Several avenues to further explore the application of SFQED to HHG include applications in quantum technology, HHG driven by quantum light, and generation in more complex targets, such as diatomic molecules.

List of Abbreviations

HHG	High-order Harmonic Generation
XUV	Extreme Ultraviolet
QED	Quantum Electrodynamics
SFQED	Strong Field Quantum Electrodynamics
TDSE	Time-Dependent Schrödinger Equation
SFA	Strong Field Approximation
CSS	Coherent State Superposition
SAE	Single Active Electron

Contents

Chapter 1

Introduction

1.1 High-Order Harmonic Generation

Lasers have been extensively used to study light-matter interactions since they were invented by Maiman in 1960 [1, 2]. This light source made it possible to achieve intensities never reached before, allowing the observation of new optical processes, like the generation of optical harmonics by atoms. When the intensity of a non-resonant driving laser is low compared to the atomic potential, harmonic generation is achieved through the absorption of n consecutive photons and the emission of the nth harmonic of the driving field. This phenomenon was first observed by Franken et al. in 1961 [3], who detected second harmonic generation in a solid target. In subsequent studies, low-order harmonics were generated in plasma and gas targets. The conversion efficiencies were found to decrease exponentially with the harmonic order of the emission. These results can be explained by perturbation theory, which is often adequate to describe harmonic generation in the low-intensity regime, i.e., when the laser field is weak enough to be considered a perturbation to the field-free Hamiltonian.

With the development of ultrashort high-power lasers, previously unknown optical processes were observed during the 80s. In 1987, two separate laboratories, Chicago [4] and Saclay [5], discovered that by focusing an intense picosecond laser on a gas target, one may observe the emission of light pulses consisting of a superposition of high-order odd harmonics. This process, now known as High-order Harmonic Generation (HHG), produces coherent eXtreme UltraViolet (XUV) light pulses with attosecond durations (Figure 1.1). These characteristics make HHG of interest for applications in fundamental physics and material science research [6].

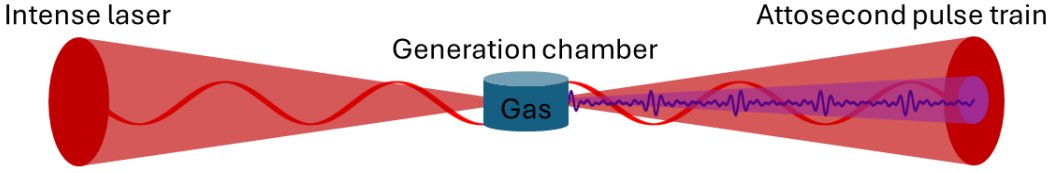

Figure 1.1: Schematic representation of HHG. An intense laser is focused on a gas. In principle, the driving laser can be a continuous wave laser. In practice, to achieve the required high intensities, the driving laser is a finite duration pulse of a few femtoseconds. As a result of the light-atom interaction, high-order harmonics of the fundamental frequency are emitted producing an Attosecond Pulse Train (ATP).

Unlike low-harmonic generation, HHG cannot be described perturbatively, and when it was first observed, there was no theoretical framework available. In the years following its discovery, a few theoretical models and numerical methods were developed to understand and describe HHG. The first theoretical framework that accomplished this is known as the 3-step model, which was proposed by Kulander et al. [7] and Corkum [8] in 1993. It describes the light-matter interaction as follows. HHG happens when the electric potential of the driving laser is of the order of the atomic potential. Under such conditions, (1) an electron can escape the confining potential through tunneling, (2) undergo propagation in the continuum, and finally, (3) recombine with the parent ion (Figure 1.2). As the photoelectron is accelerated by the driving field in the continuum, it gains kinetic energy. When it recombines with the parent ion it emits highly energetic photons: $\hbar\omega = I_p + E_{kin}$ where $\hbar$ is Plank's reduced constant, ω is the angular frequency of the light, I_p is the atom's ionization energy, and E_{kin} is the electron's kinetic energy. This process repeats itself every half cycle, creating constructive and destructive interference that generates an XUV Attosecond Pulse Train (APT).

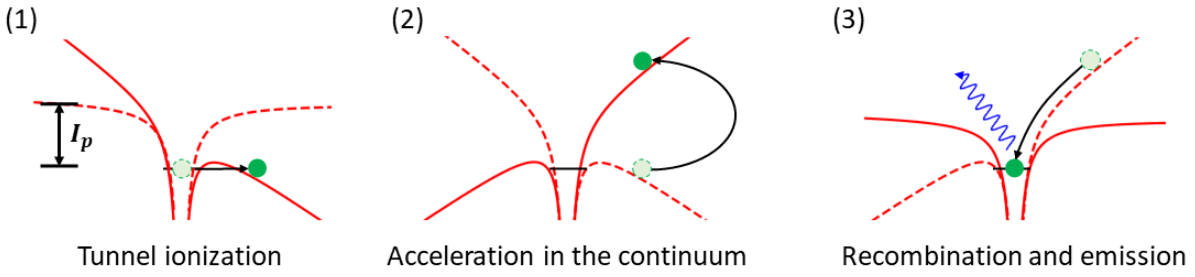

Figure 1.2: Schematic representation of the 3-step model for a linearly polarized driving laser. The figures represent (1) tunnel ionization, (2) propagation in the continuum, and (3) recombination and emission. The solid red lines represent the potential present in each step, including the atomic and radiation potentials. The dashed red lines represent the potential present in the previous step, or in the case of (1), the atomic potential in the absence of the laser. The electron is represented with dots, in bright green for the electron at the current step, and light green for the electron in the previous step. The emitted photon is represented with a blue wave.

The HHG spectrum (Figure 1.3) consists of a comb of frequencies presenting the expected exponential decrease in efficiency for the low-order harmonics (perturbative regime), followed by a nearly constant efficiency plateau for the high-order odd harmonics (nonperturbative regime) that ends abruptly at some cut-off frequency. This cutoff is related to the maximum kinetic energy an electron following a classical trajectory may gain while propagating in the continuum. On the other hand, the isotropy of the atomic system, as well as the periodic oscillation of the driving field result in the emission of only odd harmonics (ionization may occur when the field is positive or negative).

The observed cutoff energy depends on the driving laser parameters, and with the development of shorter-duration higher-intensity pulses, the plateau has been extended into the hundreds of harmonics. With the 3-step model, it was shown that the cutoff position follows the universal law $E_{cutoff} \cong I_p + 3.2U_p$, where $U_p = (e^2/8\pi^2\varepsilon_0 c^3 m_e) I\lambda^2$ is the ponderomotive energy, proportional to the driving laser intensity I times its square wavelength λ^2. This model constitutes a simple and intuitive way of understanding HHG. Furthermore, quantum mechanical models recover the cutoff law found with it, making it a good quantitative description as well [9, 10].

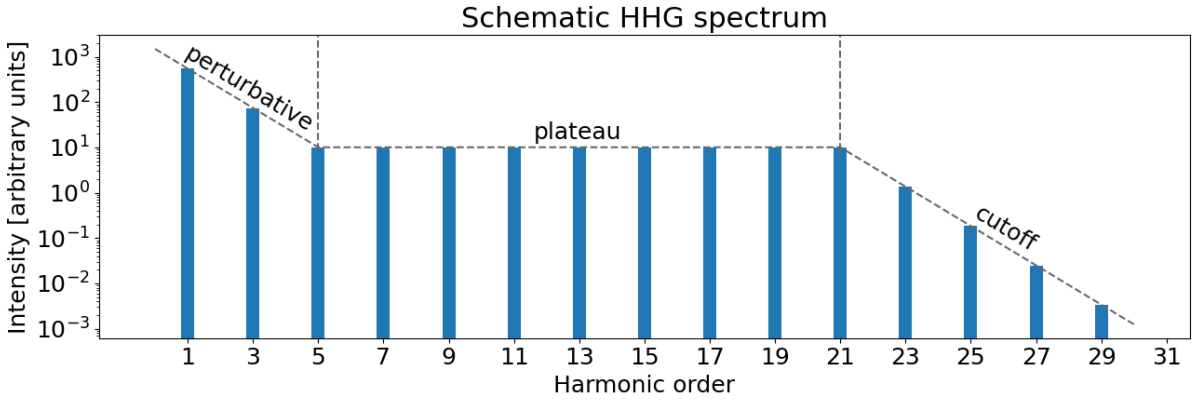

Figure 1.3: Schematic representation of an HHG spectrum in logarithmic scale. The spectrum consists of three distinct parts (exaggerated for clarity): the perturbative regime for low orders, the plateau for intermediate orders, and the cutoff region at the highest orders.

A formal approach to the complete treatment of matter in intense laser fields relies on solving the Time-Dependent Schrödinger Equation (TDSE). Numerical solutions for simple systems, e.g., HHG on a hydrogen atom or a hydrogen molecule, were developed shortly after the discovery of HHG [11, 12]. Nevertheless, this requires extensive computational power, and for realistic laboratory conditions where several more complicated atoms/molecules participate in the HHG process, solving the TDSE exactly is unfeasible. Under these circumstances, approximate methods are necessary.

An approximate method of particular relevance is the Strong Field Approximation (SFA). It was first suggested for HHG by Ehlotzky in 1992 [13], and later successfully formulated by Lewenstein et al. in 1994 [10]. In this framework three key assumptions are made: (1) the strong laser field only couples to the atomic ground state $|g\rangle$ (no internal resonances), (2) the time-dependent amplitude of the ground state is considered to be $a(t) \cong 1$ (no depletion), and (3) the continuum states are taken to be the exact solutions for a free electron propagating in a laser field $|\boldsymbol{p}(t)\rangle$ (the atomic potential is neglected). SFA is valid in the regime of low laser frequency and high intensity, where the ionization happens through tunneling and the effects of the atomic potential on the dynamics of the electron in the continuum can be neglected. These characteristics make it an adequate tool for describing HHG as a simple and efficient model widely used by experimentalists [10, 14, 15].

Until recently, it was consensus that a Quantum Electrodynamics (QED) formulation of HHG wasn't necessary, given that it is a coherent process where many photons participate. Nevertheless, there has been an effort to develop a quantum optical description and recent work confirms that, after the interaction, both the driving field and the harmonic radiation possess quantum features that may play an important role in experiments [16, 17, 2, 18, 19, 20].

In these newly published papers, a Strong Field Quantum Electrodynamics (SFQED) theory is developed treating both the atoms and the radiation as quantum systems [16, 17]. In this new framework, it is possible to separate the light-matter interaction into a 'classical coupling' and its 'quantum corrections'. The 'classical coupling' between the driving laser field and the atoms governs the dynamics of the electronic system. Meanwhile, the 'quantum corrections' describe the dynamics of the radiation field, including the emission

of the harmonics and the back-action on the driving laser. This allows for the use of the previously developed methods to solve the 'classical' part of the problem. Afterward, this partial solution can be used to find the back-action and the amplitudes of the emitted harmonics, effectively solving the full problem. Additionally, these papers suggest promising applications of this theory in quantum technology and attosecond science [2]. Particularly, the engineering of high photon number Schrödinger Cat states with quantum HHG is discussed along with proposals for an experimental setup to generate, characterize, and control them, as it may represent a potential tool for quantum computation [18, 19, 20].

In the literature, macroscopic effects in HHG have not been addressed in detail using the new framework. In realistic laboratory conditions, the atoms and the laser used for HHG have a spatial distribution. Therefore, atoms at different positions experience different intensities from the radiation field. This raises the question of whether there are macroscopic effects on the generated radiation due to the different contributions from each atom to the spectrum. If there are important macroscopic effects, it is crucial to consider them in the theory, since they may have significant implications for the applications mentioned before.

1.2 Scope of this work

For this degree project, I joined the Attolab group from the Atomic Physics Division at Lund University, which mainly focuses on studying attosecond photoionization using photoelectron interferometry. To do quantum state tomography of the photoionized electron wave packets, the Attolab group developed the KRAKEN technique where the attosecond radiation is considered fully coherent and any loss of purity of the electron state is attributed to coupling to environmental degrees of freedom or partial measurements of entangled states [21, 22]. In HHG, macroscopic effects play a major role and can affect the spatial and temporal properties of the emitted XUV radiation. So far, there has been no discussion of these effects in the framework of SFQED. This work aims to investigate how macroscopic effects modeled within SFQED can affect the properties of the XUV radiation's final quantum state. To do this, I have written a Python simulation considering generation in a single hydrogen atom. In this simulation, SFA is used to solve the semi-classical part of the problem, and the emitted radiation is modeled and characterized using the results from the SFQED formalism. Subsequently, I expanded this simulation to describe the HHG process in four atoms considering their spatial distribution. The results of the two simulations are presented and discussed in this thesis work. The knowledge acquired through this project will aid the Attolab group in determining the relevance of the new quantum theory for their line of research and in developing experiments where macroscopic effects may be measured, provided they play an important role.

1.3 Outline

The content of this thesis is structured as follows. In Chapter 1, a brief introduction to HHG and its history is provided. A general description of the project's goals and methods is given. In Chapter 2, the theoretical background necessary to formulate the quantum optical description of HHG is laid out. The SFQED theory applied to HHG is reviewed in

detail, and the fundamentals and main results of SFA are presented. Chapter 3 explains in detail the considerations and methods of the numerical implementation. The results of each simulation are presented and analyzed in depth. In Chapter 4, a summary and conclusions of this thesis work are provided. Different possible avenues to continue this research are discussed. Lastly, Chapter 5 contains the acknowledgments.

Chapter 2

Theoretical Framework

2.1 The Quantum Description of light

In this section, the fundamental formalism needed to describe radiation within quantum theory is introduced. The electromagnetic fields are quantized. Classical and quantum representations of light are discussed and contrasted. The quantum description of coherent states of light is laid out. The statistical characterization of different states of light is discussed. The content of this section closely follows the work presented in [23, 24, 25, 26], where the reader may find additional details.

2.1.1 States of Light: Waves and Particles

The heart of classical electromagnetism is Maxwell's equations. In SI units, these equations read:

$$\boldsymbol{\nabla} \cdot \boldsymbol{B} = 0, \tag{2.1a}$$

$$\boldsymbol{\nabla} \times \boldsymbol{E} = -\frac{\partial \boldsymbol{B}}{\partial t}, \tag{2.1b}$$

$$\boldsymbol{\nabla} \cdot \boldsymbol{E} = \frac{\rho}{\varepsilon_0}, \tag{2.1c}$$

$$\boldsymbol{\nabla} \times \boldsymbol{B} = \mu_0 \boldsymbol{J} + \frac{1}{c^2}\frac{\partial \boldsymbol{E}}{\partial t}. \tag{2.1d}$$

Classical free radiation states (or light waves) are given by the electric and magnetic fields that solve equations 2.1 in the absence of charges ($\rho = 0$) and currents ($\boldsymbol{J} = 0$). In such a case, the solutions are plane waves, which may be written in the following way:

$$\boldsymbol{E}(\boldsymbol{r}, t) = \boldsymbol{E}_0 e^{i\varphi} e^{i(\boldsymbol{k}\cdot\boldsymbol{r} - \omega t)}, \tag{2.2a}$$

$$\boldsymbol{B}(\boldsymbol{r}, t) = \boldsymbol{B}_0 e^{i\varphi} e^{i(\boldsymbol{k}\cdot\boldsymbol{r} - \omega t)}, \tag{2.2b}$$

where $\boldsymbol{E}_0$ and $\boldsymbol{B}_0$ are the field amplitudes, $\boldsymbol{k}$ is the wave vector, ω is the angular frequency, and φ is the phase. The field amplitudes fulfill the relation $|\boldsymbol{E}_0|/|\boldsymbol{B}_0| = c$, making the electric field much stronger than the magnetic field.

Poynting's Theorem [27] states that the total energy density stored in the electromagnetic field is given by:

$$u = \frac{1}{2}\left(\varepsilon_0 |\boldsymbol{E}|^2 + \frac{1}{\mu_0}|\boldsymbol{B}|^2\right). \tag{2.3}$$

Therefore, the free field Hamiltonian function is:

$$H = \frac{1}{2}\int d^3r \left(\varepsilon_0|\boldsymbol{E}|^2 + \frac{1}{\mu_0}|\boldsymbol{B}|^2\right). \tag{2.4}$$

On the other hand, the electric and magnetic fields may be written in terms of a scalar potential field $U(\boldsymbol{r},t)$ and a vector potential field $\boldsymbol{A}(\boldsymbol{r},t)$ in the following way:

$$\boldsymbol{E}(\boldsymbol{r},t) = -\boldsymbol{\nabla}U(\boldsymbol{r},t) - \frac{\partial \boldsymbol{A}(\boldsymbol{r},t)}{\partial t}, \tag{2.5a}$$

$$\boldsymbol{B}(\boldsymbol{r},t) = \boldsymbol{\nabla}\times\boldsymbol{A}(\boldsymbol{r},t), \tag{2.5b}$$

These expressions are invariant under gauge transformations:

$$\boldsymbol{A}(\boldsymbol{r},t) \longrightarrow \boldsymbol{A'}(\boldsymbol{r},t) = \boldsymbol{A}(\boldsymbol{r},t) + \boldsymbol{\nabla}f(\boldsymbol{r},t), \tag{2.6a}$$

$$U(\boldsymbol{r},t) \longrightarrow U'(\boldsymbol{r},t) = U(\boldsymbol{r},t) - \partial_t f(\boldsymbol{r},t), \tag{2.6b}$$

where f is a scalar function of time and position. In particular, it is possible to choose f such that $\boldsymbol{\nabla}\cdot\boldsymbol{A} = 0$ and $U = 0$. The first condition is known as the Coulomb gauge, and it will be used throughout this thesis unless stated otherwise. In this case, the Hamiltonian function can be written as:

$$H = \frac{1}{2}\int d^3r \left(\varepsilon_0\left|\partial_t\boldsymbol{A}\right|^2 + \frac{1}{\mu_0}\left|\boldsymbol{\nabla}\times\boldsymbol{A}\right|^2\right). \tag{2.7}$$

If the Hamiltonian function is Fourier transformed into reciprocal space where $\boldsymbol{\nabla}\to\boldsymbol{k}$, and the transformed $\mathcal{A}(\boldsymbol{r},t)$ and $\boldsymbol{\pi}(\boldsymbol{r},t) = \varepsilon_0\partial_t\mathcal{A}(\boldsymbol{r},t) = -\varepsilon_0\mathcal{E}(\boldsymbol{r},t)$ are considered as the generalized coordinates analogous to position $\boldsymbol{r}$ and momentum $\boldsymbol{p}$, then equation 2.7 looks remarkably similar to the Hamiltonian function for a harmonic oscillator[1] [23, 24]:

$$H_{HO} = \frac{1}{2}\left(\frac{\boldsymbol{p}^2}{m} + m\omega^2\boldsymbol{r}^2\right). \tag{2.8}$$

To formulate a quantum description of light, it is necessary to postulate the vector field and its conjugate momentum field as operators. Motivated by the similarities with the harmonic oscillator, it is proposed that [28]:

$$\left[\hat{\boldsymbol{A}}(\boldsymbol{r}), \hat{\boldsymbol{\Pi}}(\boldsymbol{r'})\right] = i\hbar\delta(\boldsymbol{r}-\boldsymbol{r'}), \tag{2.9}$$

and

$$\hat{\boldsymbol{A}}(\boldsymbol{r}) = \sum_l \int d^3k \sqrt{\frac{\hbar}{2\varepsilon_0 ck(2\pi)^3}}\left[\hat{a}_{\boldsymbol{k},l}\boldsymbol{\epsilon}_{\boldsymbol{k},l}e^{i\boldsymbol{k}\cdot\boldsymbol{r}} + H.c.\right], \tag{2.10a}$$

$$\hat{\boldsymbol{\Pi}}(\boldsymbol{r}) = \sum_l \int d^3k \sqrt{\frac{\hbar\varepsilon_0 ck}{2(2\pi)^3}}\left[-i\hat{a}_{\boldsymbol{k},l}\boldsymbol{\epsilon}_{\boldsymbol{k},l}e^{i\boldsymbol{k}\cdot\boldsymbol{r}} + H.c.\right], \tag{2.10b}$$

where $(\boldsymbol{\epsilon}_{\boldsymbol{k},l})_m = \delta_{lm}$ are the polarization vectors ($l,m\in\{1,2,3\}$), and $\hat{a}_{\boldsymbol{k},l}, \hat{a}^\dagger_{\boldsymbol{k},l}$ are the annihilation and creation operators corresponding to mode $\boldsymbol{k}$ and polarization l, which fulfill the commutation relations $[\hat{a}_{\boldsymbol{k},l}, \hat{a}^\dagger_{\boldsymbol{k'},l'}] = \delta(\boldsymbol{k}-\boldsymbol{k'})\delta_{ll'}$. [2]

[1] In reciprocal space, the Coulomb gauge implies $\boldsymbol{k}\perp\mathcal{A}$.

[2] The operators in 2.10 are defined in the Schrödinger picture, where the time dependence is embedded in the states rather than the operators.

The free radiation quantized Hamiltonian is obtained substituting equations 2.10 in 2.7:

$$\hat{H}_{FR} = \sum_l \int d^3k \; \hbar\omega_{\boldsymbol{k}} \left(\hat{a}^\dagger_{\boldsymbol{k},l} \hat{a}_{\boldsymbol{k},l} + \frac{1}{2} \right), \tag{2.11}$$

where $\omega_{\boldsymbol{k}} = ck$ is the angular frequency and $\hat{a}^\dagger_{\boldsymbol{k},l}\hat{a}_{\boldsymbol{k},l} = \hat{N}_{\boldsymbol{k},l}$ is known as the number operator. Equation 2.11 shows that the Hamiltonian operator for free radiation corresponds to the sum of individual harmonic oscillators for each mode $\boldsymbol{k}$ and polarization l. Therefore, the solutions will be given by the number states $|n\rangle_{\boldsymbol{k},l}$ such that:

$$\hat{H}_{FR}|n\rangle_{\boldsymbol{k},l} = \hbar\omega_{\boldsymbol{k}} \left(n + \frac{1}{2} \right) |n\rangle_{\boldsymbol{k},l}, \tag{2.12}$$

where the action of the creation and annihilation operators on the number states (also known as Fock states) is given by:

$$\hat{a}^\dagger_{\boldsymbol{k},l}|n\rangle_{\boldsymbol{k},l} = \sqrt{n+1}|n+1\rangle_{\boldsymbol{k},l}, \tag{2.13a}$$

$$\hat{a}_{\boldsymbol{k},l}|n\rangle_{\boldsymbol{k},l} = \sqrt{n}|n-1\rangle_{\boldsymbol{k},l}, \tag{2.13b}$$

$$\hat{a}_{\boldsymbol{k},l}\hat{a}^\dagger_{\boldsymbol{k},l}|n\rangle_{\boldsymbol{k},l} = \hat{N}|n\rangle_{\boldsymbol{k},l} = n|n\rangle_{\boldsymbol{k},l}. \tag{2.13c}$$

The classical description of light is fully deterministic with a definite value of the magnetic and electric fields for each time and position. In quantum theory, position and momentum are conjugate variables that obey Heissenberg's uncertainty principle $\Delta x \Delta p \geq \hbar/2$, where $\Delta x = \sqrt{\langle x^2 \rangle - \langle x \rangle^2}$. This means the expected values for the analogous field operators spread across an interval instead of having a definite value, i.e., $\Delta \boldsymbol{A}(\boldsymbol{r}, t) \Delta \boldsymbol{E}(\boldsymbol{r}, t) \geq \hbar/2$.

2.1.2 Coherent States

Coherent states of light are defined as:

$$|\alpha_{\boldsymbol{k},l}\rangle = e^{-\frac{|\alpha_{\boldsymbol{k},l}|^2}{2}} \sum_{n=0}^{\infty} \frac{\alpha^n_{\boldsymbol{k},l}}{\sqrt{n!}} |n\rangle_{\boldsymbol{k},l}, \tag{2.14}$$

where $\alpha_{\boldsymbol{k},l}$ is a complex number[3]. These states are a superposition of number states, and therefore they are solutions of the Hamiltonian $\hat{H}_{FR}$. Furthermore, $\hat{a}_{\boldsymbol{k},l}|\alpha_{\boldsymbol{k},l}\rangle = \alpha_{\boldsymbol{k},l}|\alpha_{\boldsymbol{k},l}\rangle$, i.e., they are eigenstates of $\hat{a}_{\boldsymbol{k},l}$ with eigenvalue $\alpha_{\boldsymbol{k},l}$ (see Appendix A.1).

To simplify the notation, the subscript $\boldsymbol{k}, l$ that labels the mode and polarization corresponding to each Hilbert space will be omitted in the discussion that follows. Nevertheless, the reader should keep in mind that each mode and polarization have their own set of operators and basis states.

The annihilation operator $\hat{a}$ is not Hermitian; hence, its eigenvalues α are not observables. Nevertheless, the number operator $\hat{N}$ is a Hermitian operator with measurable eigenvalues. The probability of measuring n photons given a coherent state $|\alpha\rangle$ is:

$$P(n) = |\langle n|\alpha\rangle|^2 = \left| e^{-|\alpha|^2/2} \frac{\alpha^n}{\sqrt{n!}} \right|^2 = e^{-|\alpha|^2} \frac{|\alpha|^{2n}}{n!}. \tag{2.15}$$

[3]Here there is a slight abuse of notation, as it is considered that the undefined number 0^0 is equal to 1 so that the Fock vacuum state $|n = 0\rangle$ and the coherent vacuum state $|\alpha = 0\rangle$ coincide.

Equation 2.15 is known as a Poissonian distribution, characterized by $\Delta n = \sqrt{\langle n \rangle}$. For a coherent state $|\alpha\rangle$, $\Delta n = \sqrt{\langle n \rangle} = |\alpha|$ (see Appendix A.2).

Although the annihilation operator is not Hermitian, it can be shown that the coherent states fulfill the completeness relation [26]:

$$\frac{1}{\pi} \int d^2\alpha |\alpha\rangle\langle\alpha| = \mathbb{1}, \tag{2.16}$$

where $d^2\alpha = d(\mathrm{Re}\,\alpha) d(\mathrm{Im}\,\alpha)$. This implies that for any Fock state $|n\rangle$:

$$|n\rangle = \frac{1}{\pi} \int \langle\alpha|n\rangle |\alpha\rangle d^2\alpha. \tag{2.17}$$

Thus, any arbitrary state may be decomposed in terms of coherent states. Nevertheless, coherent states are not orthogonal to each other:

$$\begin{aligned} \langle\alpha|\beta\rangle &= e^{-|\alpha|^2/2 - |\beta|^2/2} \sum_{n,m} \frac{\alpha^{*n} \beta^m}{\sqrt{n!m!}} \langle n|m\rangle \\ &= e^{-|\alpha|^2/2 - |\beta|^2/2 + \alpha^*\beta} \neq 0 \quad \forall \alpha, \beta \in \mathbb{C}. \end{aligned} \tag{2.18}$$

This means that the set of all coherent states is linearly dependent and any arbitrary state decomposition is not unique [26]. Then, $\{|\alpha\rangle : \alpha \in \mathbb{C}\}$ constitutes an over-complete basis of the Hilbert space.

The photon number is not the only observable of a coherent state. Drawing from the analogy with harmonic oscillators, Hermitian quadrature operators may be defined as:

$$\hat{x} = \sqrt{\frac{\hbar}{2\omega}} (\hat{a}^\dagger + \hat{a}), \tag{2.19a}$$

$$\hat{p} = i\sqrt{\frac{\hbar\omega}{2}} (\hat{a}^\dagger - \hat{a}). \tag{2.19b}$$

The expected values of these quadrature operators are then given by:

$$\langle x \rangle = \sqrt{\frac{2\hbar}{\omega}} \langle\alpha|(\hat{a}^\dagger + \hat{a})|\alpha\rangle = \sqrt{\frac{\hbar}{2\omega}} (\alpha^* + \alpha) = \sqrt{\frac{2\hbar}{\omega}}\, \mathrm{Re}\,\alpha, \tag{2.20a}$$

$$\langle p \rangle = i\sqrt{\frac{\hbar\omega}{2}} \langle\alpha|(\hat{a}^\dagger - \hat{a})|\alpha\rangle = i\sqrt{\frac{\hbar\omega}{2}} (\alpha^* - \alpha) = i\sqrt{2\hbar\omega}\, \mathrm{Im}\,\alpha. \tag{2.20b}$$

Thus, the coherent states' phase space is in direct correspondence with the complex plane of eigenvalues α, which provides a powerful tool for the graphic representation of these states and their dynamics (Figure 2.1). Furthermore, the quadrature operators' fluctuations are given by:

$$\Delta x = \sqrt{\langle x^2 \rangle - \langle x \rangle^2} = \sqrt{\frac{\hbar}{2\omega}(4\mathrm{Re}^2\,\alpha + 1) - \frac{2\hbar}{\omega}\mathrm{Re}^2\,\alpha} = \sqrt{\frac{\hbar}{2\omega}}, \tag{2.21a}$$

$$\Delta p = \sqrt{\langle p^2 \rangle - \langle p \rangle^2} = \sqrt{\frac{\hbar\omega}{2}(4\mathrm{Im}^2\,\alpha + 1) - 2\hbar\omega\mathrm{Im}^2\,\alpha} = \sqrt{\frac{\hbar\omega}{2}}, \tag{2.21b}$$

such that $\Delta x \Delta p = \hbar/2$. Therefore, although coherent states are quantum states, they possess minimum uncertainty, bringing this description as close as possible to classical localization.

In many sources, the quadrature operators are defined as the 'normalized' operators [24]:

$$\hat{x} = \frac{1}{2}(\hat{a}^\dagger + \hat{a}), \tag{2.22a}$$

$$\hat{p} = \frac{i}{2}(\hat{a}^\dagger - \hat{a}). \tag{2.22b}$$

Then $[\hat{x}, \hat{p}] = i/2$, $\Delta x = \Delta p = 1$, and $\alpha = \langle\alpha|\hat{x}|\alpha\rangle + i\langle\alpha|\hat{p}|\alpha\rangle$. These definitions make the representation of coherent states in the optical phase space symmetrical in both quadratures. From this point on, the quadrature operators considered in this thesis will be those from equations 2.22.

It is of interest to investigate the temporal evolution of coherent states in the phase space representation. According to Schrödinger's equation, the coherent states evolve in time as:

$$|\alpha(t)\rangle = \hat{U}(t)|\alpha(0)\rangle \tag{2.23}$$

where $\hat{U}(t) = e^{-i\hat{H}_{FR}t/\hbar}$ is the time evolution operator. Here, it is convenient to momentarily switch to the Heisenberg picture and consider the time evolution of the annihilation operator $\hat{a}(t) = \hat{U}^\dagger(t)\hat{a}(0)\hat{U}(t)$ instead. The Heisenberg equation that governs the time evolution reads:

$$\begin{aligned}\frac{d}{dt}\hat{a}(t) &= \frac{i}{\hbar}\left[\hat{H}_{FR}(t), \hat{a}(t)\right] = \frac{i}{\hbar}\hbar\omega\left[\hat{a}(t)\hat{a}^\dagger(t), \hat{a}(t)\right] \\ &= i\omega\left(\hat{a}(t)[\hat{a}^\dagger(t), \hat{a}(t)] + [\hat{a}(t), \hat{a}(t)]\hat{a}^\dagger(t)\right) = -i\omega\hat{a}(t).\end{aligned} \tag{2.24}$$

Therefore, $\hat{a}(t) = e^{-i\omega t}\hat{a}(0)$, and $\hat{a}(t)|\alpha\rangle = e^{-i\omega t}\alpha|\alpha\rangle$. Then, returning to the Schrödinger picture, the evolution of the eigenvalues will be $\alpha(t) = e^{-i\omega t}\alpha(0)$, such that:

$$\hat{a}|\alpha(t)\rangle = e^{-i\omega t}\alpha(0)|\alpha(t)\rangle. \tag{2.25}$$

2.1.3 The Displacement Operator

The coherent states understood as eigenstates of the annihilation operator are an abstract mathematical description of light. Nevertheless, a lot of insight can be gained from an intuitive understanding of coherent states. To achieve this, one can think of the most elementary light source: an electric current distribution $\boldsymbol{J}(\boldsymbol{r}, t)$ coupled to the electric field through the vector potential $\boldsymbol{A}(\boldsymbol{r}, t)$. Then, in the interaction picture with respect to $\hat{H}_{FR}$, the evolution of the radiation state $|\psi(t)\rangle$ is described by:

$$i\hbar\frac{d}{dt}|\psi(t)\rangle = \int d^3r \boldsymbol{J}(\boldsymbol{r}, t)\cdot\hat{\boldsymbol{A}}(\boldsymbol{r}, t)|\psi(t)\rangle. \tag{2.26}$$

The solution will be given by $|\psi(t)\rangle = \hat{U}(t)|\psi(0)\rangle$ with

$$\hat{U}(t) = \mathcal{T}\exp\left[-\frac{i}{\hbar}\int_0^t dt' \int d^3r \boldsymbol{J}(\boldsymbol{r}, t')\cdot\hat{\boldsymbol{A}}(\boldsymbol{r}, t')\right], \tag{2.27}$$

where $\mathcal{T}$ denotes the time-ordering of the terms in the exponential expansion. Plugging the definition from equation 2.10a into equation 2.27 and defining the following quantity:

$$\alpha_{\boldsymbol{k},l}(t) = \frac{i}{\hbar}\sqrt{\frac{\hbar}{2\varepsilon_0 ck(2\pi)^3}}\int_0^t dt' \int d^3r \boldsymbol{J}(\boldsymbol{r}, t')\cdot\boldsymbol{\epsilon}_{\boldsymbol{k},l}\, e^{-i(\omega_{\boldsymbol{k}}t' - \boldsymbol{k}\cdot\boldsymbol{r})}, \tag{2.28}$$

the evolved state may be expressed as:

$$|\psi(t)\rangle = \mathcal{T}\exp\left[\sum_l \int d^3k \left[\alpha_{\boldsymbol{k},l}(t)\hat{a}^\dagger_{\boldsymbol{k},l} - \alpha^*_{\boldsymbol{k},l}(t)\hat{a}_{\boldsymbol{k},l}\right]\right]|\psi(0)\rangle. \tag{2.29}$$

Notice that the numbers $\alpha_{\boldsymbol{k},l}(t)$ are the Fourier transform of the classical current $\boldsymbol{J}(\boldsymbol{r},t)$. Now, using the Zassenhaus formula [4] equation 2.29 becomes:

$$|\psi(t)\rangle = \bigotimes_{\boldsymbol{k},l} e^{i\varphi_{\boldsymbol{k},l}(t)}\exp\left[\alpha_{\boldsymbol{k},l}(t)\hat{a}^\dagger_{\boldsymbol{k},l} - \alpha^*_{\boldsymbol{k},l}(t)\hat{a}_{\boldsymbol{k},l}\right]|\psi(0)\rangle, \tag{2.30}$$

where $\bigotimes_{\boldsymbol{k},l}$ represents the infinite tensor product over all modes, and the phase is given by the commutator of the exponential argument at different times $0 < t' < t$:

$$\begin{aligned}\exp\left(i\varphi_{\boldsymbol{k},l}(t)\right) &= \exp\left[(\alpha_{\boldsymbol{k},l}(t)\hat{a}^\dagger_{\boldsymbol{k},l} - \alpha^*_{\boldsymbol{k},l}(t)\hat{a}_{\boldsymbol{k},l}), (\alpha_{\boldsymbol{k}',l'}(t')\hat{a}^\dagger_{\boldsymbol{k}',l'} - \alpha^*_{\boldsymbol{k}',l'}(t')\hat{a}_{\boldsymbol{k}',l'})\right] \\ &= \exp\left(i\,2\,\mathrm{Im}\left[\alpha_{\boldsymbol{k},l}(t)\alpha^*_{\boldsymbol{k},l}(t')\right]\right).\end{aligned} \tag{2.31}$$

From equation 2.30, it is clear that the dynamics of the radiation state $|\psi(t)\rangle$ are completely determined by the exponential operators in the product. Motivated by this, it is convenient to define a set of unitary operators given by:

$$\hat{D}_{\boldsymbol{k},l}(\alpha_{\boldsymbol{k},l}) = \exp\left[\alpha_{\boldsymbol{k},l}\hat{a}^\dagger_{\boldsymbol{k},l} - \alpha^*_{\boldsymbol{k},l}\hat{a}_{\boldsymbol{k},l}\right]. \tag{2.32}$$

These are known as the displacement operators for reasons that will become evident soon. If the initial radiation state is considered to be the vacuum, then the action of a given displacement operator $\hat{D}_{\boldsymbol{k},l}(\alpha_{\boldsymbol{k},l})$ on that state will generate $|\alpha_{\boldsymbol{k},l}\rangle$:

$$\begin{aligned}\hat{D}_{\boldsymbol{k},l}(\alpha_{\boldsymbol{k},l})|0_{\boldsymbol{k},l}\rangle &= \exp\frac{|\alpha_{\boldsymbol{k},l}|^2}{2}\exp\left(\alpha_{\boldsymbol{k},l}\hat{a}^\dagger_{\boldsymbol{k},l}\right)\exp(\alpha^*_{\boldsymbol{k},l}\hat{a}_{\boldsymbol{k},l})|0_{\boldsymbol{k},l}\rangle \\ &= \exp\frac{|\alpha_{\boldsymbol{k},l}|^2}{2}\exp\left(\alpha_{\boldsymbol{k},l}\hat{a}^\dagger_{\boldsymbol{k},l}\right)|0_{\boldsymbol{k},l}\rangle = e^{\frac{|\alpha_{\boldsymbol{k},l}|^2}{2}}\sum_{n=0}^{\infty}\frac{\alpha^n_{\boldsymbol{k},l}\hat{a}^{\dagger n}_{\boldsymbol{k},l}}{n!}|0_{\boldsymbol{k},l}\rangle \\ &= e^{\frac{|\alpha_{\boldsymbol{k},l}|^2}{2}}\sum_{n=0}^{\infty}\frac{\alpha^n_{\boldsymbol{k},l}}{\sqrt{n!}}|n\rangle_{\boldsymbol{k},l} = |\alpha_{\boldsymbol{k},l}\rangle,\end{aligned} \tag{2.33}$$

where in the first line of equation 2.33, the Zassenhaus formula was used again. Visualized in the coherent state phase space, this corresponds to a displacement of the vacuum state in the complex plane (Figure 2.1). In that sense, any coherent state can be understood as the displaced vacuum.

The action of the displacement operator $\hat{D}_{\boldsymbol{k},l}(\beta_{\boldsymbol{k},l})$ on an arbitrary coherent state $|\alpha_{\boldsymbol{k},l}\rangle$ can be obtained using that[5]:

$$\hat{D}_{\boldsymbol{k},l}(\beta_{\boldsymbol{k},l})\hat{D}_{\boldsymbol{k},l}(\alpha_{\boldsymbol{k},l}) = e^{i2\,\mathrm{Im}\left[\beta_{\boldsymbol{k},l}\alpha^*_{\boldsymbol{k},l}\right]}\hat{D}_{\boldsymbol{k},l}(\beta_{\boldsymbol{k},l} + \alpha_{\boldsymbol{k},l}). \tag{2.34}$$

[4]The Zassenhaus formula is an immediate consequence of the better known Baker-Campbell-Haussdorff formula. It states:

$$\exp(\hat{X}+\hat{Y}) = \exp(\hat{X})\exp(\hat{Y})\exp(\frac{1}{2}[\hat{X},\hat{Y}])\exp(\frac{1}{3}[\hat{Y},[\hat{X},\hat{Y}]] + \frac{1}{6}[\hat{X},[\hat{X},\hat{Y}]])\cdots.$$

[5]Equation 2.34 is a direct application of the Baker-Campbell-Hausdorff formula, which states:

$$\exp(\hat{X})\exp(\hat{Y}) = \exp\left(\hat{X}+\hat{Y}+\frac{1}{2}[\hat{X},\hat{Y}] + \frac{1}{12}[\hat{X},[\hat{X},\hat{Y}]]\cdots\right).$$

Then $\hat{D}_{\boldsymbol{k},l}(\beta_{\boldsymbol{k},l})|\alpha_{\boldsymbol{k},l}\rangle = \hat{D}_{\boldsymbol{k},l}(\beta_{\boldsymbol{k},l})\hat{D}_{\boldsymbol{k},l}(\alpha_{\boldsymbol{k},l})|0\rangle = e^{i2\,\mathrm{Im}\,[\beta_{\boldsymbol{k},l}\alpha^*_{\boldsymbol{k},l}]}|\beta_{\boldsymbol{k},l} + \alpha_{\boldsymbol{k},l}\rangle$.

For a given set $\boldsymbol{\alpha} = \{\alpha_{\boldsymbol{k},l}\}$, where a complex number has been chosen for each available mode and polarization, the transformation defined as:

$$\hat{\mathcal{D}}\left[\boldsymbol{\alpha}\right] = \bigotimes_{\boldsymbol{k},l} \hat{D}_{\boldsymbol{k},l}(\alpha_{\boldsymbol{k},l}) \tag{2.35}$$

fulfills the properties:

$$\hat{\mathcal{D}}^{\dagger}\left[\boldsymbol{\alpha}\right]\hat{\mathcal{D}}\left[\boldsymbol{\alpha}\right] = \mathbb{1}, \tag{2.36a}$$

$$\hat{\mathcal{D}}^{\dagger}\left[\boldsymbol{\alpha}\right]\hat{a}_{\boldsymbol{k'},l'}\hat{\mathcal{D}}\left[\boldsymbol{\alpha}\right] = \hat{a}_{\boldsymbol{k'},l'} + \alpha_{\boldsymbol{k'},l'}, \tag{2.36b}$$

$$\hat{\mathcal{D}}\left[\boldsymbol{\alpha}\right]\hat{a}_{\boldsymbol{k'},l'}\hat{\mathcal{D}}^{\dagger}\left[\boldsymbol{\alpha}\right] = \hat{a}_{\boldsymbol{k'},l'} - \alpha_{\boldsymbol{k'},l'}. \tag{2.36c}$$

Additionally, the action of the operator $\hat{\mathcal{D}}$ on the vacuum is given by:

$$\hat{\mathcal{D}}\left[\boldsymbol{\alpha}\right]\bigotimes_{\boldsymbol{k},l}|0_{\boldsymbol{k},l}\rangle = \bigotimes_{\boldsymbol{k},l}|\alpha_{\boldsymbol{k},l}\rangle. \tag{2.37}$$

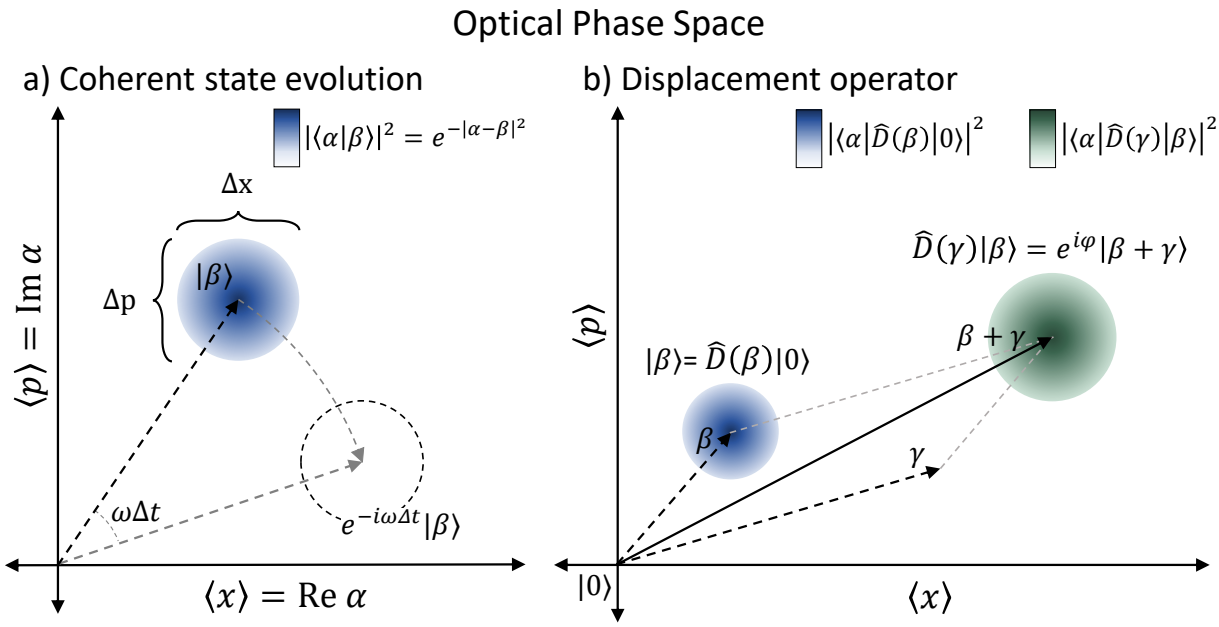

Figure 2.1: a) Optical phase space representation of a coherent state and its dynamics. A coherent state $|\beta\rangle$ is represented as a Gaussian function over the phase space (colored with a blue gradient) alongside its time evolution after a period of length Δt (outlined with a dashed line). b) Optical phase space representation of the action of the displacement operator. The vacuum state $|0\rangle$ is displaced to position β generating a state $|\beta\rangle$ (colored with a blue gradient). The state $|\beta\rangle$ is displaced to position $\beta+\gamma$ generating the state $e^{i\varphi}|\beta+\gamma\rangle$, where $\varphi = 2\mathrm{Im}\gamma\beta^*$ (colored with a green gradient). As a coherent state is displaced further away from the vacuum state, the Gaussian distribution widens.

2.1.4 Squeezed States

As discussed in subsection 2.1.2, coherent states are minimum uncertainty states that present equal uncertainty in both quadratures. Nevertheless, through certain non-linear optical interactions, it is possible to produce states of light with a reduced uncertainty

in one quadrature at the cost of enlarging the uncertainty in the other. These states are called squeezed states of light and are represented as an ellipse-shaped Gaussian in the optical phase space. Mathematically, similarly to how coherent states can be understood as the displaced vacuum, the squeezed states $|\alpha, \zeta\rangle$ can be modeled as the displaced 'squeezed vacuum':

$$|\alpha, \zeta\rangle = \hat{D}(\alpha)\hat{S}(\zeta)|0\rangle, \tag{2.38}$$

where $\hat{S} = \exp[1/2(\zeta^* \hat{a}^2 - \zeta \hat{a}^{\dagger 2})]$ is the squeezing operator and $\zeta = re^{i\theta}$ a complex number. Then the uncertainty in the new (rotated) quadrature operators $\hat{x}_\zeta = \hat{x}e^{i\theta/2}$ and $\hat{p}_\zeta = \hat{p}e^{i\theta/2}$ is given by $\Delta\hat{x}_\zeta = e^{-r}/2$ and $\Delta\hat{p}_\zeta = e^r/2$.

2.1.5 Coherent State Superposition

Another example of quantum states of light is Coherent State Superpositions (CSS):

$$|\psi\rangle = \sum_i c_i |\alpha_i\rangle. \tag{2.39}$$

A particular case of special interest for applications in quantum technology is the Schrödinger Cat state. This is a quantum superposition of 2 coherent states with opposite phases:

$$|cat\rangle = c_1|\alpha\rangle + c_2|-\alpha\rangle. \tag{2.40}$$

Since the time evolution of coherent states remains coherent, these states can be used to engineer qbits with long coherence times. Another interesting feature of cat states is that they are quantum superpositions of two classically distinguishable states, effectively realizing Schrödinger's thought experiment right in the limit between the quantum and the classical.

2.1.6 Thermal States

Quantum formalism can be used to describe what is known as thermal or chaotic states of light, which are also well described by black-body radiation. Thermal light is electromagnetic radiation emitted by moving charged particles in matter. All matter with non-zero temperature emits thermal light. Thermal states are described by an incoherent mixture of different Fock states. For a single-mode field in thermal equilibrium at temperature T:

$$\hat{\rho} = \frac{\exp(-\beta\hat{H})}{\mathrm{Tr}[\exp(-\beta\hat{H})]} = \sum_n \rho_{nn}|n\rangle\langle n|, \tag{2.41}$$

where $\beta = 1/\kappa_B T$ and $\hat{H} = \hbar\omega(\hat{a}^\dagger\hat{a} + 1/2)$. Then the average photon number will be given by:

$$\langle n\rangle = \mathrm{Tr}(\hat{\rho}\hat{N}) = \sum_n n\rho_{nn} = \frac{1}{e^{\beta\hbar\omega} - 1}, \tag{2.42}$$

and the probability of measuring n photons is:

$$P(n) = \rho_{nn} = (1 - e^{-\beta\hbar\omega})e^{-n\beta\hbar\omega} = \frac{1}{\langle n\rangle + 1}\left(\frac{\langle n\rangle}{\langle n\rangle + 1}\right)^n. \tag{2.43}$$

For the derivations of equations 2.41 through 2.43, see reference [24].

2.1.7 Characterizing States of Light

Now that different states of light have been reviewed, it is opportune to discuss the characteristics intrinsic to each of them. The criterion most widely used to classify states of light is their photon statistics, which can be super-Poissonian, Poissonian, or sub-Poissonian. A distribution is said to be Poissonian if $\Delta n = \langle n \rangle^{1/2}$, super-Poissonian if $\Delta n > \langle n \rangle^{1/2}$, and sub-Poissonian if $\Delta n < \langle n \rangle^{1/2}$.

A state's photon statistics can be used to assess the 'quantumness' of the light. In the previous subsections, different states of light were modeled using the formalism of quantum mechanics. Some of those states can also be modeled with classical field theories, such as thermal and coherent states [29, 28]. On the other hand, neither squeezed light nor CSSs can be described with classical theories. In this sense, one may say that squeezed light and CSS can be considered 'quantum light' (they only admit a quantum description), while thermal light and coherent light may be classified as 'classical light' (they admit both descriptions). If a state of light presents a sub-Poissonian photon distribution, it is concluded that the state at hand represents quantum light. This condition is enough, but not necessary, as exemplified by the squeezed vacuum state in Table 2.1, which has super-Poissonian statistics but is clearly non-describable with classical electromagnetism.

The classification of states discussed in the previous subsections is included in Table 2.1. For derivations and further details, the reader should refer to [23, 24].

Type	State	$\langle n \rangle$	Δn	Classification
Thermal states	$\hat{\rho} = \frac{\exp(-\beta \hat{H}_{FR})}{\mathrm{Tr}[\exp(-\beta \hat{H}_{FR})]}$	$\frac{1}{e^{\beta\hbar\omega}-1}$	$\frac{e^{\beta\hbar\omega/2}}{(e^{\beta\hbar\omega}-1)}$	Super-Poissonian
Squeezed vacuum	$\lvert\psi\rangle = \lvert\zeta\rangle$	$\sinh^2 r$	$\sqrt{2}\sinh r \cosh r$	Super-Poissonian
Coherent states	$\lvert\psi\rangle = \lvert\alpha\rangle$	$\lvert\alpha\rvert^2$	$\lvert\alpha\rvert$	Poissonian
Fock states	$\lvert\psi\rangle = \lvert n\rangle$	n	0	Sub-Poissonian

Table 2.1: Photon statistics classification for thermal, squeezed vacuum, coherent, and Fock states. From left to right: light type, state, average photon number, standard deviation, and classification are shown for each light state.

A convenient short-hand parameter one may use to classify a light state is the Mandel parameter, defined as:

$$Q = \frac{\langle n^2 \rangle - \langle n \rangle^2}{\langle n \rangle} - 1. \tag{2.44}$$

Then a distribution will be Poissonian if $Q = 0$, super-Poissonian if $Q > 0$, and sub-Poissonian if $Q < 0$.

2.2 The Quantum Electrodynamics Description of High-Order Harmonic Generation

In this section, a full Quantum Electrodynamics (QED) description of HHG is developed from first principles following the formalism presented in [17, 16]. Starting with Maxwell's equations in the reciprocal space, the fields are separated into longitudinal and transverse components with respect to the wave vector. The longitudinal component corresponds to the Coulomb potential due to the charge distribution, while the transverse component contains all the information about the radiation field and the light-matter interaction [28]. Subsequently, the minimal coupling Hamiltonian is quantized and the dipole approximation is introduced. This separates the Hamiltonian into three independent terms, the electronic Hamiltonian, the radiation Hamiltonian, and the interaction Hamiltonian. Finally, the interaction Hamiltonian is separated into 'semi-classical' and 'quantum' components, allowing the use of known methods, such as solving the semi-classical TDSE numerically or using SFA, to obtain the solution.

2.2.1 Classical Light-Matter Interaction in the Coulomb Gauge

In this subsection, the formalism presented in [28] is followed closely. Once more, the starting point is Maxwell's equations 2.1, but this time in the presence of a charge distribution $\rho(\boldsymbol{r},t)$ and the associated current $\boldsymbol{J}(\boldsymbol{r},t)$. Performing a spatial Fourier transform on equations 2.1, the following expressions are obtained:

$$i\boldsymbol{k}\cdot\boldsymbol{\mathcal{B}}(\boldsymbol{k},t)=0, \tag{2.45a}$$

$$i\boldsymbol{k}\times\boldsymbol{\mathcal{E}}(\boldsymbol{k},t)=-\frac{\partial}{\partial t}\boldsymbol{\mathcal{B}}(\boldsymbol{k},t), \tag{2.45b}$$

$$i\boldsymbol{k}\cdot\boldsymbol{\mathcal{E}}(\boldsymbol{k},t)=\frac{\varrho(\boldsymbol{k},t)}{\varepsilon_0}, \tag{2.45c}$$

$$i\boldsymbol{k}\times\boldsymbol{\mathcal{B}}(\boldsymbol{k},t)=\mu_0\boldsymbol{\mathcal{J}}(\boldsymbol{k},t)+\frac{1}{c^2}\frac{\partial}{\partial t}\boldsymbol{\mathcal{E}}(\boldsymbol{k},t). \tag{2.45d}$$

Further, the longitudinal and transverse components of the fields with respect to the wave vector $\boldsymbol{k}$ are separated according to:

$$ik\mathcal{B}_{\parallel}(\boldsymbol{k},t)=0, \tag{2.46a}$$

$$i\boldsymbol{k}\times\boldsymbol{\mathcal{E}}_{\perp}(\boldsymbol{k},t)=-\frac{\partial}{\partial t}\boldsymbol{\mathcal{B}}_{\perp}(\boldsymbol{k},t), \tag{2.46b}$$

$$ik\mathcal{E}_{\parallel}(\boldsymbol{k},t)=\frac{\varrho(\boldsymbol{k},t)}{\varepsilon_0}, \tag{2.46c}$$

$$i\boldsymbol{k}\times\boldsymbol{\mathcal{B}}_{\perp}(\boldsymbol{k},t)=\mu_0\boldsymbol{\mathcal{J}}_{\perp}(\boldsymbol{k},t)+\frac{1}{c^2}\frac{\partial}{\partial t}\boldsymbol{\mathcal{E}}_{\perp}(\boldsymbol{k},t). \tag{2.46d}$$

The Coulomb gauge, where $\boldsymbol{\nabla}\cdot\boldsymbol{A}=0$, eliminates the longitudinal component of the vector field in reciprocal space, i.e., $\boldsymbol{\mathcal{A}}_{\parallel}=0$. Then, equations 2.5 expressed in the conjugate variable become:

$$\mathcal{E}_{\parallel}(\boldsymbol{k},t)=-ik\mathcal{U}(\boldsymbol{k},t), \tag{2.47a}$$

$$\boldsymbol{\mathcal{E}}_{\perp}(\boldsymbol{k},t)=-\frac{\partial}{\partial t}\boldsymbol{\mathcal{A}}_{\perp}(\boldsymbol{k},t), \tag{2.47b}$$

$$\boldsymbol{\mathcal{B}}_{\perp}(\boldsymbol{r},t)=i\boldsymbol{k}\times\boldsymbol{\mathcal{A}}_{\perp}(\boldsymbol{r},t). \tag{2.47c}$$

Comparing equations 2.46c and 2.47a one obtains:

$$\mathcal{U}(\boldsymbol{k},t) = \frac{1}{\varepsilon_0 k^2}\varrho(\boldsymbol{k},t). \tag{2.48}$$

Transforming back to the space variable:

$$U(\boldsymbol{r},t) = \frac{1}{4\pi\varepsilon_0}\int d^3r' \frac{\rho(\boldsymbol{r'},t)}{|\boldsymbol{r}-\boldsymbol{r'}|}. \tag{2.49}$$

Therefore, in the Coulomb gauge, the longitudinal vector potential is zero and the scalar potential corresponds to the Coulomb potential due to the charge distribution $\rho(\boldsymbol{r},t)$. Hence, the independent variables associated with the radiation field will be the transverse vector potential $\boldsymbol{A}_\perp(\boldsymbol{r},t) = \boldsymbol{A}(\boldsymbol{r},t)$ and its temporal derivative $\dot{\boldsymbol{A}}(\boldsymbol{r},t) = -\boldsymbol{E}_\perp(\boldsymbol{r},t)$, which can be quantized as in section 2.1.1.

2.2.2 Minimal Coupling and the Dipole Approximation

Consider a distribution of N atoms at positions $\{\boldsymbol{R}_i \,|\, i \in \{1,2,...,N\}\}$ interacting with a radiation field. In the following, the Single Active Electron (SAE) approximation is used. Within the SAE approximation, it is considered that the field only interacts with a single electron that experiences an appropriately chosen effective potential. Then, the interaction can be described by the minimal coupling Hamiltonian consisting of two terms:

$$\hat{H} = \hat{H}_C + \hat{H}_R, \tag{2.50}$$

where the first term describes the coupling of the electrons with positions $\hat{\boldsymbol{r}}_i$ and momenta $\hat{\boldsymbol{p}}_i$ to the radiation field:

$$\hat{H}_C(t) = \sum_i \left\{ \frac{1}{2m}\left[\hat{\boldsymbol{p}}_i - e\hat{\boldsymbol{A}}_\perp(\hat{\boldsymbol{r}}_i)\right]^2 + \hat{V}_{SAE}(\hat{\boldsymbol{r}}_i, \boldsymbol{R}_i)\right\}, \tag{2.51}$$

and the second term describes the free transverse radiation field:

$$\begin{aligned}\hat{H}_R &= \frac{1}{2}\int d^3r \left\{ \frac{1}{\varepsilon_0}\hat{\boldsymbol{\Pi}}_\perp(\hat{\boldsymbol{r}}) + \frac{1}{\mu_0}\left[\boldsymbol{\nabla}\times\hat{\boldsymbol{A}}_\perp(\hat{\boldsymbol{r}})\right]\right\} \\ &= \sum_l \int d^3k\ \hbar\omega_{\boldsymbol{k}} \left(\hat{a}^\dagger_{\boldsymbol{k},l}\hat{a}_{\boldsymbol{k},l} + \frac{1}{2}\right).\end{aligned} \tag{2.52}$$

The Hamiltonian $\hat{H}_C(t)$ can be further simplified using the dipole approximation, which is valid when the wavelength of the radiation is much larger than the typical size of an atom ($\boldsymbol{k}\cdot\langle\boldsymbol{R}_i - \boldsymbol{r}_i\rangle << 1$). Within the dipole approximation, it is considered that the electric and vector potential fields are approximately constant in the small volume occupied by each atom. Under this approximation, the total Hamiltonian can be separated into three terms: one term describing the electronic degrees of freedom[6], one describing the radiation and one describing the interaction between the two:

$$\hat{H} = \hat{H}_E + \hat{H}_R + \hat{H}_I, \tag{2.53}$$

[6]This term contains a potential $\hat{V}'(\hat{\boldsymbol{r}}_i, \boldsymbol{R}_i)$ which is the SAE effective potential considering polarization effects [17].

where:

$$\hat{H}_E = \sum_i \left\{ \frac{\hat{\boldsymbol{p}}_i^2}{2m} + \hat{V}'(\hat{\boldsymbol{r}}_i, \boldsymbol{R}_i) \right\}, \tag{2.54}$$

and

$$\hat{H}_I = \sum_i e\hat{\boldsymbol{r}}_i \cdot \hat{\boldsymbol{E}}_\perp(\boldsymbol{R}_i). \tag{2.55}$$

Note that the theory considered here is a non-relativistic quantum description of electrons interacting with radiation in the dipole approximation. This theory is ultraviolet divergent, partially due to the incorrect treatment of large wave vectors in the dipole approximation. The divergence cannot be successfully renormalized [30], but it can be treated including a form factor that tempers the coupling to high frequencies [31, 32]:

$$g(\boldsymbol{k}) = \frac{\Gamma}{\sqrt{\Gamma^2 + k^2}}, \tag{2.56}$$

where $\Gamma = d^{-1}$ with d the characteristic amplitude of electron oscillations in the fundamental electric field. With this consideration, the quantized electric field becomes:

$$\hat{\boldsymbol{E}}_\perp(\boldsymbol{R}_i) = \sum_l \int d^3k \tilde{g}_i(\boldsymbol{k}) \left[i\hat{a}_{\boldsymbol{k},l} \boldsymbol{\epsilon}_{\boldsymbol{k},l} e^{i\boldsymbol{k}\cdot\boldsymbol{R}_i} + H.c. \right], \tag{2.57}$$

where:

$$\tilde{g}_i(\boldsymbol{k}) = g_i(\boldsymbol{k}) \sqrt{\frac{\hbar ck}{2\varepsilon_0 (2\pi)^3}}. \tag{2.58}$$

2.2.3 The Time-Dependent Schrödinger Equation for HHG

Two different methods are available in the literature to find solutions to the Hamiltonian 2.50. Reference [16], proposes a very general theory where the quantum component of the interaction Hamiltonian is treated as a perturbation to the semi-classical component. In this treatment, any method may be used to solve the semi-classical problem. On the other hand, a less general theory using the dipole approximation, where SFA is required to solve the semi-classical component is developed in reference [17]. In this subsection, an SFQED theory using the dipole approximation where any method can be used to solve the semi-classical Hamiltonian is presented. The intention is to put forward a formulation located in the middle ground between the SFA-specific theory developed in [17] and the completely general theory developed in [16]. As a starting point, consider the Schrödinger equation:

$$i\hbar \frac{\partial}{\partial t} |\psi(t)\rangle = [\hat{H}_E + \hat{H}_R + \hat{H}_I] |\psi(t)\rangle, \tag{2.59}$$

where $|\psi(t)\rangle = |\psi_E(t)\rangle \otimes |\psi_R(t)\rangle$ describes both the electronic state $|\psi_E(t)\rangle$ and the radiation state $|\psi_R(t)\rangle$. Note that postulating the total wave function as a tensor product of the electronic and radiation states eliminates the possibility of having entanglement between the two sub-systems. The treatment explicitly presented in this subsection makes use of this simplifying assumption. This choice and style of presentation are consistent with the fact that, at a later point in the theoretical derivation, the dipole moment is obtained using SFA. Within SFA, a key assumption is that the electric field only couples to the ground state, a prescription that effectively destroys the entanglement between atom and radiation. However, a comprehensive treatment where the wave function is

considered to be a general element in the Hilbert space $\mathcal{H}_E \otimes \mathcal{H}_R$, rather than the product $|\psi_E(t)\rangle \otimes |\psi_R(t)\rangle$, is available in references [16, 17]. The reader is referred to the original literature for full details.

In the following, a single-mode laser of frequency ω_L is considered. Additionally, before the interaction, the atoms are taken to be all in their ground state $|g_i\rangle$ and the only populated mode is the fundamental $\boldsymbol{k}_L, \ell$, i.e.,

$$|\psi(0)\rangle = \bigotimes_i |g_i\rangle \bigotimes_\ell |\alpha_{\boldsymbol{k}_L,\ell}\rangle \bigotimes_{\boldsymbol{k}\neq\boldsymbol{k}_L,l} |0_{\boldsymbol{k},l}\rangle. \tag{2.60}$$

Since the solutions of $\hat{H}_R$ are known, it is convenient to transform the Schrödinger equation to the interaction picture by applying the unitary transformation $\hat{U}_1(t) = \exp(i\hat{H}_R t/\hbar)$:

$$|\psi(t)\rangle \longrightarrow |\psi_1(t)\rangle = \hat{U}_1(t)|\psi(t)\rangle = |\psi_E(t)\rangle \otimes \hat{U}_1(t)|\psi_R(t)\rangle, \tag{2.61a}$$

$$\hat{H}_E \longrightarrow \hat{H}_{1E} = \hat{U}_1(t)\hat{H}_E\hat{U}_1^\dagger(t) = \hat{H}_E, \tag{2.61b}$$

$$\hat{H}_I \longrightarrow \hat{H}_{1I} = \hat{U}_1(t)\hat{H}_I\hat{U}_1^\dagger(t) = \hat{H}_I(t) = \sum_i e\hat{\boldsymbol{r}}_i \cdot \hat{\boldsymbol{E}}_\perp(\boldsymbol{R}_i, t), \tag{2.61c}$$

where it was used that $\hat{U}_1(t)\hat{a}\hat{U}_1^\dagger(t) = \hat{a}(t)$, yielding:

$$\hat{\boldsymbol{E}}_\perp(\boldsymbol{R}_i, t) = \sum_l \int d^3k \tilde{g}_i(\boldsymbol{k}) \left[i\hat{a}_{\boldsymbol{k},l}(t)\boldsymbol{\epsilon}_{\boldsymbol{k},l} e^{i\boldsymbol{k}\cdot\boldsymbol{R}_i} + H.c. \right]. \tag{2.62}$$

Now, let $\boldsymbol{\beta} = \{\beta_{\boldsymbol{k},l}\}$ be such that $\beta_{\boldsymbol{k}\neq\boldsymbol{k}_L,l} = 0$, and $\beta_{\boldsymbol{k}_L,\ell} = \alpha_{\boldsymbol{k}_L,\ell}$ for $\ell \in \{1,2,3\}$. Then, the unitary operator $\hat{\mathcal{D}}^\dagger[\boldsymbol{\beta}]$ defined in 2.35, and which displaces the fundamental mode to the vacuum state, can be used to transform the state and operators in 2.61 as follows:

$$|\psi_1(t)\rangle \longrightarrow |\psi_2(t)\rangle = \hat{\mathcal{D}}^\dagger[\boldsymbol{\beta}]|\psi_1(t)\rangle = |\psi_E(t)\rangle \otimes \hat{\mathcal{D}}^\dagger[\boldsymbol{\beta}]\hat{U}_1(t)|\psi_R(t)\rangle, \tag{2.63a}$$

$$\hat{H}_E \longrightarrow \hat{H}_{2E} = \hat{\mathcal{D}}^\dagger[\boldsymbol{\beta}]\hat{H}_E\hat{\mathcal{D}}[\boldsymbol{\beta}] = \hat{H}_E, \tag{2.63b}$$

$$\hat{H}_I(t) \longrightarrow \hat{H}_{2I}(t) = \hat{\mathcal{D}}^\dagger[\boldsymbol{\beta}]\hat{H}_I(t)\hat{\mathcal{D}}^\dagger[\boldsymbol{\beta}] = \hat{H}_{CI}(t) + \hat{H}_{QI}(t), \tag{2.63c}$$

where the properties in 2.36 have been used, and as a result, the interaction Hamiltonian has been split into 'semi-classical' and 'quantum' components given by:

$$\begin{aligned}\hat{H}_{CI}(t) &= \sum_i e\hat{\boldsymbol{r}}_i \cdot \boldsymbol{E}_C(\boldsymbol{R}_i, t) = e\sum_{i,l} \int d^3k \tilde{g}_i(\boldsymbol{k})\, \hat{\boldsymbol{r}}_i \cdot \left[i\, \beta_{\boldsymbol{k},l}\, \boldsymbol{\epsilon}_{\boldsymbol{k},l}\, e^{i(\boldsymbol{k}\cdot\boldsymbol{R}_i - \omega_{\boldsymbol{k}}t)} + H.c. \right] \\ &= e\sum_{i,\ell} \tilde{g}_i(\boldsymbol{k}_L)\, \hat{\boldsymbol{r}}_i \cdot \left[i\, \alpha_{\boldsymbol{k}_L,\ell}\, \boldsymbol{\epsilon}_{\boldsymbol{k}_L,\ell}\, e^{i(\boldsymbol{k}_L\cdot\boldsymbol{R}_i - \omega_L t)} + H.c. \right], \end{aligned} \tag{2.64a}$$

$$\hat{H}_{QI}(t) = \sum_i e\hat{\boldsymbol{r}}_i \cdot \hat{\boldsymbol{E}}_Q(\boldsymbol{R}_i, t) = e\sum_{i,l} \int d^3k \tilde{g}_i(\boldsymbol{k})\, \hat{\boldsymbol{r}}_i \cdot \left[i\hat{a}_{\boldsymbol{k},l}(t)\boldsymbol{\epsilon}_{\boldsymbol{k},l} e^{i\boldsymbol{k}\cdot\boldsymbol{R}_i} + H.c. \right]. \tag{2.64b}$$

Thus, the new Schrödinger equation is:

$$i\hbar\frac{\partial}{\partial t}|\psi_2(t)\rangle = [\hat{H}_E + \hat{H}_{CI}(t) + \hat{H}_{QI}(t)]|\psi_2(t)\rangle. \tag{2.65}$$

Note that the solutions to the semi-classical Hamiltonian $\hat{H}_{SC}(t) = \hat{H}_E + \hat{H}_{CI}(t)$ can be obtained with the previously developed methods, e.g., by numerically solving the TDSE

or using SFA. Therefore, the Schrödinger equation in 2.65 can be further simplified by transforming to the interaction picture with respect to $\hat{H}_{SC}(t)$, using the unitary operator $\hat{U}_3(t) = \mathcal{T}\exp\left[i\int_0^t \hat{H}_{SC}(t')dt'\right]$:

$$|\psi_2(t)\rangle \longrightarrow |\psi_3(t)\rangle = \hat{U}_3(t)|\psi_2(t)\rangle = \hat{U}_3(t)|\psi_E(t)\rangle \otimes \hat{\mathcal{D}}^\dagger[\boldsymbol{\beta}]\hat{U}_1(t)|\psi_R(t)\rangle$$
$$= |\psi_{3E}(t)\rangle \otimes |\psi_{3R}(t)\rangle, \tag{2.66a}$$
$$\hat{H}_{QI} \longrightarrow \hat{H}_{3QI} = \hat{U}_3(t)\hat{H}_{QI}\hat{U}_3^\dagger(t) = e\sum_i \hat{\boldsymbol{r}}_i(t)\cdot\hat{\boldsymbol{E}}_Q(\boldsymbol{R}_i,t), \tag{2.66b}$$

with $\hat{\boldsymbol{r}}_i(t) = \hat{U}_3(t)\hat{\boldsymbol{r}}_i\hat{U}_3^\dagger(t)$. Hence, the Schrödinger equation reduces to

$$i\hbar\frac{\partial}{\partial t}|\psi_3(t)\rangle = e\sum_i \hat{\boldsymbol{r}}_i(t)\cdot\hat{\boldsymbol{E}}_Q(\boldsymbol{R}_i,t)|\psi_3(t)\rangle. \tag{2.67}$$

This work will focus on the solution of the radiation part of the wavefunction $|\psi_R(t)\rangle$. The electronic part $|\psi_E(t)\rangle$ can be eliminated from the analysis by projecting equation 2.67 onto a complete set of solutions $\{|\phi_n\rangle\}$ to the Hamiltonian $\hat{H}_E$, while simultaneously inserting an identity operator as follows:

$$i\hbar\frac{\partial}{\partial t}\sum_n \langle\phi_n|\psi_{3E}(t)\rangle \otimes |\psi_{3R}(t)\rangle$$
$$= e\sum_i \sum_{n,m}\langle\phi_n|\hat{\boldsymbol{r}}_i(t)|\phi_m\rangle\cdot\hat{\boldsymbol{E}}_Q(\boldsymbol{R}_i,t)[\langle\phi_m|\psi_{3E}(t)\rangle \otimes |\psi_{3R}(t)\rangle]. \tag{2.68}$$

Here $\langle\phi_n|\psi_{3E}(t)\rangle = \langle\tilde{\phi}_n(t)|\psi_E(t)\rangle$ and $\langle\phi_n|\hat{\boldsymbol{r}}_i(t)|\phi_m\rangle = \langle\tilde{\phi}_n(t)|\hat{\boldsymbol{r}}_i|\tilde{\phi}_m(t)\rangle$, with $\{|\tilde{\phi}_n(t)\rangle\}$ the set of solutions to $\hat{H}_{SC}$ given by $|\tilde{\phi}_n(t)\rangle = \hat{U}_3^\dagger(t)|\phi_n\rangle$. Note that to obtain the dipole moment $\langle\hat{\boldsymbol{r}}(t)\rangle_{n,m}$, one needs the full set of solutions to $\hat{H}_{SC}(t)$ evolved from the full set of solutions to $\hat{H}_E$. However, equation 2.68 encompasses all possible processes in strong laser-matter interactions. Here the focus is on HHG, and therefore one may select the processes that yield high-order harmonics by exclusively considering dipole transitions between the bound states of $\hat{H}_E$. Hence, one may write the Schrödinger equation concerning the radiation state as:

$$i\hbar\frac{\partial}{\partial t}|\psi_{3R}(t)\rangle = e\sum_{i,n,m}\langle\hat{\boldsymbol{r}}_i(t)\rangle_{nm}\cdot\hat{\boldsymbol{E}}_Q(\boldsymbol{R}_i,t)|\psi_{3R}(t)\rangle. \tag{2.69}$$

Furthermore, when generating on N atoms, with N such that $N << N^2$, the coherent part of the spectrum, i.e., the portion corresponding to the diagonal dipole elements $\langle\hat{\boldsymbol{r}}(t)\rangle_n$, will dominate [33, 16]. This is due to the random phase that results when the electron recombines to a state different than the one it tunneled from. On the other hand, when the electron recombines to the same state there is a fixed phase. Then, one may neglect the cross terms which will cancel out and not contribute to the final emission. Generation in a few atoms, where $N \sim N^2$, yields very low intensities. For current applications, the harmonics are generated in a very large number of atoms, and the incoherent contributions are never considered. In reference [16], the authors study generation in a single atom taking into account the incoherent contributions. Here, the focus will be on exploring the nature of the emitted XUV radiation that is used to study

attosecond photoionization. Therefore, only the coherent contributions will be considered. With this assumption, equation 2.69 is exactly solvable using the time evolution operator:

$$\hat{U}(t) = \mathcal{T}\exp\left(\frac{-ie}{\hbar}\int_0^t dt' \sum_{i,n}\langle\hat{\boldsymbol{r}}_i(t')\rangle_n \cdot \hat{\boldsymbol{E}}_Q(\boldsymbol{R}_i, t')\right). \tag{2.70}$$

Moreover, defining:

$$\chi_{\boldsymbol{k},l}(t) = -e\sum_{i,n}\tilde{g}_i(\boldsymbol{k})e^{-i\boldsymbol{k}\cdot\boldsymbol{R}_i}\int_0^t dt'\langle\hat{\boldsymbol{r}}_i(t')\rangle_n \cdot \boldsymbol{\epsilon}_{\boldsymbol{k},l}e^{i\omega_{\boldsymbol{k}}t'}, \tag{2.71}$$

and using equation 2.64b, the time evolution operator from 2.70 can be written as:

$$\begin{aligned}\hat{U}(t) &= \mathcal{T}\exp\left(\frac{1}{\hbar}\sum_l\int d^3k[\chi_{\boldsymbol{k},l}(t)\hat{a}^\dagger_{\boldsymbol{k},l} - \chi^*_{\boldsymbol{k},l}(t)\hat{a}_{\boldsymbol{k},l}]\right)\\ &= \bigotimes_{\boldsymbol{k},l}\hat{D}(\chi_{\boldsymbol{k},l}(t))e^{i\varphi_{\boldsymbol{k},l}(t)},\end{aligned} \tag{2.72}$$

where $\varphi_{\boldsymbol{k},l}(t)$ comes from the Zassenhaus formula, which yields the phase:

$$\begin{aligned}\varphi_{\boldsymbol{k},l}(t) &= \frac{1}{\hbar}\left[\left(\chi_{\boldsymbol{k},l}(t)\hat{a}^\dagger_{\boldsymbol{k},l} - \chi^*_{\boldsymbol{k},l}(t)\hat{a}_{\boldsymbol{k},l}\right), \left(\chi_{\boldsymbol{k'},l'}(t_1)\hat{a}^\dagger_{\boldsymbol{k'},l'} - \chi^*_{\boldsymbol{k'},l'}(t_1)\hat{a}_{\boldsymbol{k'},l'}\right)\right]\\ &= \frac{e^2}{\hbar}\sum_{\substack{i,j\\n,m}}\Bigg\{\tilde{g}_i^2(\boldsymbol{k})\int_0^t dt_1\langle\hat{\boldsymbol{r}}_i(t')\rangle_n \cdot \boldsymbol{\epsilon}_{\boldsymbol{k},l}\int_0^{t_1} dt'\langle\hat{\boldsymbol{r}}_j(t')\rangle_m \cdot \boldsymbol{\epsilon}_{\boldsymbol{k},l}\\ &\qquad \sin\left[\boldsymbol{k}\cdot(\boldsymbol{R}_j - \boldsymbol{R}_i) + \omega_{\boldsymbol{k}}(t_1 - t')\right]\Bigg\}.\end{aligned} \tag{2.73}$$

Then, the solutions to 2.69 are given by:

$$\begin{aligned}|\psi_{3R}(t)\rangle &= \bigotimes_{\boldsymbol{k},l}\hat{D}(\chi_{\boldsymbol{k},l}(t))e^{i\varphi_{\boldsymbol{k},l}(t)}|\psi_{3R}(0)\rangle\\ &= \bigotimes_{\ell}e^{i\varphi_{\boldsymbol{k}_L,\ell}(t)}|\chi_{\boldsymbol{k}_L,\ell}(t)\rangle\bigotimes_{\boldsymbol{k},l}e^{i\varphi_{\boldsymbol{k},l}(t)}|\chi_{\boldsymbol{k},l}(t)\rangle.\end{aligned} \tag{2.74}$$

To obtain the radiation state in the original frame of reference, the transformations done in previous steps must be inverted $|\psi_R(t)\rangle = \hat{U}_1^\dagger(t)\hat{\mathcal{D}}[\boldsymbol{\beta}]|\psi_{3R}(t)\rangle$:

$$|\psi_R(t)\rangle = \bigotimes_{\ell}e^{i\varphi_{\boldsymbol{k}_L,\ell}(t)}e^{i\theta_\ell(t)}|\left[\alpha_{\boldsymbol{k}_L,\ell} + \chi_{\boldsymbol{k}_L,\ell}(t)\right]e^{-i\omega_L t}\rangle\bigotimes_{\boldsymbol{k},l}e^{i\varphi_{\boldsymbol{k},l}(t)}|\chi_{\boldsymbol{k},l}(t)e^{-i\omega_{\boldsymbol{k}}t}\rangle, \tag{2.75}$$

where $\theta_\ell(t) = 2\,\mathrm{Im}\left[\alpha_{\boldsymbol{k}_L,\ell}\chi^*_{\boldsymbol{k}_L,\ell}(t)\right]$.

The HHG emission spectrum is directly proportional to the Fourier transform of the dipole velocity $\langle\phi_n|\dot{\boldsymbol{r}}_i(t)|\phi_n\rangle$ [34]:

$$\begin{aligned}S(\omega_{\boldsymbol{k}}) &\propto \left|\sum_{i,n}\tilde{g}_i(\boldsymbol{k})e^{-i\boldsymbol{k}\cdot\boldsymbol{R}_i}\int_{-\infty}^{\infty}dt'\langle\phi_n|\dot{\boldsymbol{r}}_i(t')|\phi_n\rangle e^{i\omega_{\boldsymbol{k}}t'}\cdot\boldsymbol{\epsilon}_{\boldsymbol{k},l}\right|^2\\ &= \omega_{\boldsymbol{k}}^2\left|\sum_{i,n}\tilde{g}_i(\boldsymbol{k})e^{-i\boldsymbol{k}\cdot\boldsymbol{R}_i}\langle\tilde{\boldsymbol{r}}_i(\omega_{\boldsymbol{k}})\rangle_n\cdot\boldsymbol{\epsilon}_{\boldsymbol{k},l}\right|^2,\end{aligned} \tag{2.76}$$

where $\tilde{\boldsymbol{r}}$ denotes the Fourier transform of the dipole moment[7]. Therefore,

$$S(\omega_{\boldsymbol{k}}) \propto \omega_{\boldsymbol{k}}^2 \lim_{t\to\infty} |\chi_{\boldsymbol{k},l}(t)|^2. \tag{2.77}$$

From this treatment, it becomes evident that a spatial distribution will have an effect on the displacements $\chi_{\boldsymbol{k}_L,\ell}$ through the phase factor in 2.71 (if $\boldsymbol{k} \not\perp \boldsymbol{R}_i$) and through the magnitude of the time-dependent dipole moment, introducing some distortion in the spectrum. Additionally, the final state's phases will also be affected as seen in 2.73. Nevertheless, the solution for each mode will still be a coherent state of the form 2.75. States of light with quantum characteristics such as sub-Poissonian statistics and squeezing, can be obtained in schemes where the incoherent part of the emission is not neglected [16]. Still, as discussed previously, generation in small samples consisting of just a few atoms yields very weak signals, and for most experimental applications it is not relevant to consider this case.

The sum in equation 2.76 contains many terms, making it very computationally demanding to evaluate the total dipole moment. Nevertheless, here, SFA is used to obtain the solutions to $\hat{H}_{SC}$ making the evaluation of the dipole moment much simpler.

2.3 Strong Field Approximation

In this section, the fundamentals of SFA are presented and the assumptions considered for the numerical analysis are stated [10, 35, 36]. Exceptionally clear and detailed derivations of all expressions can be found in reference [37]. Here only the main results are presented. From this point forward, all equations are expressed in atomic units [a. u.], where it is assumed that $\hbar = 1$, $e = -1$, $\varepsilon_0 = 4\pi$, and $c \approx 137$. All calculations in both simulations are carried out in atomic units as well.

2.3.1 Main Assumptions

The simplest version of the SFA model is that proposed by Lewenstein et al. in [10], where three key assumptions are made:

1. **There are no internal resonances:** the time-dependent dipole moment only couples to the ground state $|g\rangle$ of each atom. This assumption neglects contributions from all other bound states.

2. **The continuum states are plane waves:** propagating electrons are not influenced by the atomic potential. Therefore, the continuum states will be those of an electron being accelerated in an electric field $|\boldsymbol{p}(t)\rangle$. This assumption is valid when the driving laser intensity is such that $I_p < 2U_p$, which for infrared lasers usually holds when the intensity is in the range of $10^{13} - 10^{14}$ W/cm^2 [10]. In this situation, the electron is accelerated by the intense laser field reaching high speeds when in the vicinity of the ion. Hence, the effect of the atomic potential on the electron dynamics can be neglected.

[7]Note that the full spectrum will include the Fourier transform of the driving field $\tilde{E}(\omega)$ as well [34].

3. **There is no ground state depletion:** the depletion of the ground state can be neglected at all times. For this assumption to be reasonable, the laser intensity must be smaller than the saturation intensity of the atom, for which ionization happens directly. In other words, the ponderomotive energy must be under the saturation level $U_p < U_{sat}$. In this parameter region the ionization during the interaction is weak [38].

For simplicity's sake, and since the total dipole response is the addition of the individual atom responses, only one atom will be considered in the following discussion. Assumption 1 means that in equations 2.68 through 2.76, one may only consider the dipole moment elements $\langle g|\hat{\boldsymbol{r}}(t)|g\rangle$. Together with assumption 2, it also implies that one may write the solutions to $\hat{H}_{SC}$ as:

$$|\Psi(t)\rangle = \hat{U}_3^\dagger(t)|g\rangle = e^{iI_p t}\left(a(t)|g\rangle + \int d^3p\, b(\boldsymbol{p},t)|\boldsymbol{p}(t)\rangle\right). \tag{2.78}$$

Finally, assumption 3 implies that $a(t) \approx 1$. The amplitudes $b(\boldsymbol{p},t)$ can be found substituting 2.78 in the Schrödinger equation, which yields a solvable differential equation. The solution is found to be:

$$b(\boldsymbol{p},t) = i\int_0^t dt' \left\{\boldsymbol{E}(t')\langle \boldsymbol{p}(t')|\hat{\boldsymbol{r}}|g\rangle \exp\left[-i\int_{t'}^t d\tilde{t}\left(\frac{\boldsymbol{p}^2(\tilde{t})}{2}+I_p\right)\right]\right\}. \tag{2.79}$$

For convenience, one may introduce the shorthand notation $\boldsymbol{d}(\boldsymbol{p}(t)) = \langle \boldsymbol{p}(t)|\hat{\boldsymbol{r}}|g\rangle$ for the atomic dipole matrix element corresponding to the bound-free transition. The SFA assumptions greatly simplify the expression for the time-dependent dipole moment:

$$\begin{aligned}\boldsymbol{r}(t) &= \langle\Psi(t)|\hat{\boldsymbol{r}}|\Psi(t)\rangle = \langle g|\hat{\boldsymbol{r}}|g\rangle + \\ &+ \int d^3p'\, b^*(\boldsymbol{p}',t)\boldsymbol{d}(\boldsymbol{p}'(t)) + \int d^3p\, b(\boldsymbol{p},t)\boldsymbol{d}^*(\boldsymbol{p}(t)) \\ &+ \int d^3p\, d^3p'\, b^*(\boldsymbol{p}',t)b(\boldsymbol{p},t)\langle \boldsymbol{p}'(t)|\hat{\boldsymbol{r}}|\boldsymbol{p}(t)\rangle,\end{aligned} \tag{2.80}$$

where the first term is zero and the last term corresponds to continuum transitions which can be neglected. Substituting the mechanical momentum $\boldsymbol{p}(t)$ with the conserved canonical momentum $\boldsymbol{p}_c = \boldsymbol{p}(t) - \boldsymbol{A}(t)$, the SFA expression for the dipole moment becomes:

$$\begin{aligned}\boldsymbol{r}(t) = i\int d^3p_c \int_0^t dt' \boldsymbol{E}(t')\,\boldsymbol{d}(\boldsymbol{p}_c+\boldsymbol{A}(t'))\exp\left[-i\int_{t'}^t d\tilde{t}\left(\frac{[\boldsymbol{p}_c+\boldsymbol{A}(\tilde{t})]^2}{2}+I_p\right)\right]\boldsymbol{d}^*(\boldsymbol{p}_c+\boldsymbol{A}(t)) \\ - i\int d^3p_c \int_0^t dt' \boldsymbol{E}(t')\,\boldsymbol{d}^*(\boldsymbol{p}_c+\boldsymbol{A}(t'))\exp\left[i\int_{t'}^t d\tilde{t}\left(\frac{[\boldsymbol{p}_c+\boldsymbol{A}(\tilde{t})]^2}{2}+I_p\right)\right]\boldsymbol{d}(\boldsymbol{p}_c+\boldsymbol{A}(t)),\end{aligned} \tag{2.81}$$

where the phase in the exponential corresponds to the semi-classical action:

$$S(\boldsymbol{p}_c,t,t') = \int_{t'}^t d\tilde{t}\left(\frac{[\boldsymbol{p}_c+\boldsymbol{A}(\tilde{t})]^2}{2}+I_p\right). \tag{2.82}$$

Equation 2.81 can be interpreted in the following way. In the first term from left to right, one finds the probability amplitude of ionization at a time t', followed by the propagation of the electron in the continuum from a time t' to time t, followed by the probability amplitude for recombination at a time t, reproducing the three distinctive processes in the 3-step model.

2.3.2 The Time-Dependent Dipole Moment

The integral over the momentum in equation 2.81 can be approximated using the method of steepest descent, also known as the saddle point approximation. In this approximation, the action is Taylor expanded around its stationary points $\boldsymbol{p}_s$ and approximated to second degree $S(\boldsymbol{p}_c, t, t') \approx S(\boldsymbol{p}_s, t, t') + \nabla^2_{\boldsymbol{p}} S(\boldsymbol{p}_s, t, t')(\boldsymbol{p}_c - \boldsymbol{p}_s)^2/2$. The stationary points will be those for which the canonical momentum takes the value:

$$\boldsymbol{p}_s(t, t') = -\frac{1}{t - t'} \int_{t'}^{t} dt' \boldsymbol{A}(t'). \tag{2.83}$$

Since the action evaluated in $\boldsymbol{p}_s$ is now not a function of $\boldsymbol{p}_c$:

$$S(\boldsymbol{p}_s, t, t') = \int_{t'}^{t} d\tilde{t} \left(\frac{[\boldsymbol{p}_s + \boldsymbol{A}(\tilde{t})]^2}{2} + I_p \right), \tag{2.84}$$

after substituting the second degree approximation in equation 2.81, the remaining integral over $\boldsymbol{p}_c$ becomes a Gaussian integral that can be evaluated yielding the factor:

$$\zeta(t, t') = \left(\frac{\pi}{\varepsilon + i(t - t')/2} \right)^{3/2}, \tag{2.85}$$

where ε is an infinitesimal regulation constant.

On the other hand, to obtain an explicit expression for the function $\boldsymbol{d}(\boldsymbol{p})$, the atomic ground state is chosen to be that of a hydrogen-like atom:

$$\langle \boldsymbol{r} | g \rangle = \frac{\alpha^{3/4}}{\sqrt{\pi}} e^{-\sqrt{\alpha} r}, \tag{2.86}$$

where $\alpha = 2I_p$. Then,

$$\boldsymbol{d}(\boldsymbol{p}) = -i \frac{2^{7/2} \alpha^{5/4}}{\pi} \frac{\boldsymbol{p}}{(\boldsymbol{p}^2 + \alpha)^3}. \tag{2.87}$$

Gathering these results, the final expression for the dipole moment becomes:

$$\begin{aligned} \boldsymbol{r}(t) = i \frac{2^7 \alpha^{5/2}}{\pi^2} \int_0^t dt' \Bigg\{ & \zeta(t, t') \boldsymbol{E}(t') \frac{\boldsymbol{p}_s + \boldsymbol{A}(t')}{([\boldsymbol{p}_s + \boldsymbol{A}(t')]^2 + \alpha)^3} e^{-iS(\boldsymbol{p}_s, t, t')} \frac{\boldsymbol{p}_s + \boldsymbol{A}(t)}{([\boldsymbol{p}_s + \boldsymbol{A}(t)]^2 + \alpha)^3} \\ & - \zeta^*(t, t') \boldsymbol{E}(t') \frac{\boldsymbol{p}_s + \boldsymbol{A}(t')}{([\boldsymbol{p}_s + \boldsymbol{A}(t')]^2 + \alpha)^3} e^{iS(\boldsymbol{p}_s, t, t')} \frac{\boldsymbol{p}_s + \boldsymbol{A}(t)}{([\boldsymbol{p}_s + \boldsymbol{A}(t)]^2 + \alpha)^3} \Bigg\}. \end{aligned} \tag{2.88}$$

As mentioned before, in the single atom and few atom simulations created for this work hydrogen atoms are used. Hydrogen atoms posses a single electron, and therefore there are no electron correlations that need to be taken into account. Nevertheless, if one considers heavier atoms, electron correlations might be relevant and could be included in the electronic states that are used to compute the dipole moment. Similarly, when considering molecules one could include nuclear motion in the analysis.

Chapter 3

Numerical Implementation

3.1 Parameters

In this section, the laser parameters and target sample details considered in each simulation are clearly stated.

In the numerical implementation, the harmonics are generated in hydrogen atoms for which $I_p = 13.6$ eV. The driving laser is considered to be a linearly-polarized pulse with a sine square envelope and a Gaussian intensity profile at focus:

$$\boldsymbol{E}(r,t) = E_0 e^{-\frac{r^2}{w^2}} \sin^2\left(\frac{\pi}{\Delta t_p} t\right) \cos(\omega_L t)\, \hat{\boldsymbol{e}}_x, \tag{3.1}$$

where E_0 is the field amplitude, r is the radial distance from the beam center, w is the beam waist, Δt_p is the pulse duration, and ω_L is the angular frequency of the light. For the single atom simulation, the atom is positioned at the center of the beam where $r = 0$. For the few atoms simulation, the atoms are positioned in a plane perpendicular to the propagation axis of the beam. In this case, the phase factors $e^{-i\boldsymbol{k}\cdot\boldsymbol{R}_i}$ in equation 2.71 will be unity.[1] In Table 3.1, the laser parameters used in both the single and few atoms simulations are shown. In Figure 3.1 the corresponding electric field and vector potential at $r = 0$ are plotted.

Parameter	**SI**	**a.u.**
Wavelength	800 nm	15 118
Intensity	1×10^{14} W/cm^2	2.85×10^{-3}
Pulse duration	30 fs	1 240
Beam waist	50 µm	9.45×10^5

Table 3.1: Driving laser parameters used in simulations.

[1] This assumes that the plane where the atoms are positioned is exactly at focus or that a collimated beam is used.

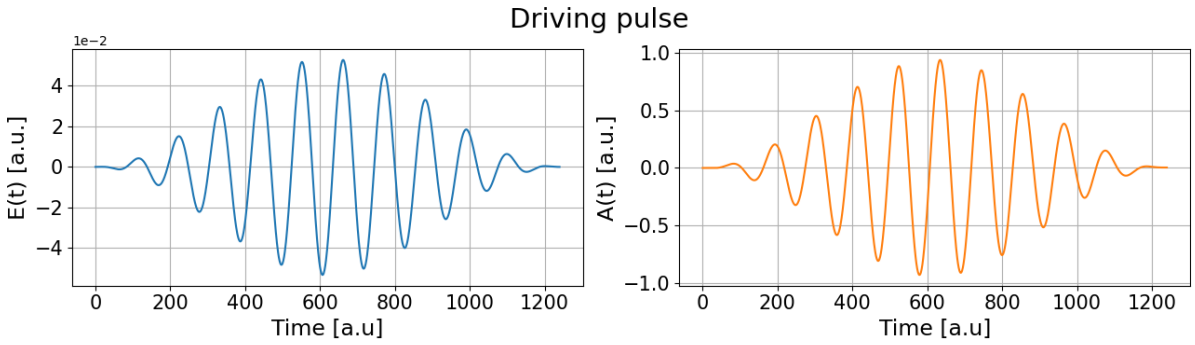

Figure 3.1: Plots of the pulse electric field and vector potential for a 800 nm laser pulse with 30 fs duration and sine square envelope. The pulse contains 11.24 cycles.

For the simulations, it is considered that before the pulse, all electrons are in their ground state, and all modes except the laser mode are in vacuum. During the interaction the harmonic modes get populated. That is, the magnitude of $\chi_{\boldsymbol{k},l}$ grows until, at the end of the pulse, the displacements have reached a final state. After the pulse, the harmonic states evolve as coherent states, and the electrons are back to their ground state.

3.2 Equations and Methods

In this section, the approximated discrete expressions, as well as the methods used to compute the momentum, action, and dipole moment found with the saddle point analysis are presented.

Both the single atom and the few atoms simulations were written using Python. The window of observation was set between $t_0 = 0$ and $t_f = \Delta t_p$ with step $\delta t = 1$, corresponding to $N = 1\,240$ time samples. For each atom at position $\boldsymbol{R}_i$, and each possible ionization time t_n, the following computations are performed for all times $t_m > t_n$:

- **Momentum:** the canonical momentum from equation 2.83 is computed using the quad function from the scipy.integrate package. Each calculated value $p_{i,nm} = p_{s,i}(t_m, t_n)$ is stored in a square matrix P_i (one matrix per atom). This matrix is used to obtain a mechanical momentum matrix $P_{kin,i}$ from which a kinetic energy matrix $E_{kin,i}$ is computed.

- **Action:** equation 2.84 is also implemented using the quad function. Once again, a value $S_{i,nm} = S_i(p_{s,i}(t_m, t_n), t_m, t_n)$ is obtained and then stored in a matrix S_i.

- **Dipole moment:** the dipole moment is approximated with the following discrete version[2] of equation 2.88:

$$x_i(t_m) \approx \delta t \sum_{n=0}^{m} x_{i,nm} = \delta t \sum_{n=0}^{m} \{i\zeta(t_m, t_n) E(\boldsymbol{R}_i, t_n) \times d(p_{i,nm} + A(\boldsymbol{R}_i, t_n)) e^{-iS_{i,nm}} d^*(p_{i,nm} + A(\boldsymbol{R}_i, t_m)) + c.c\} . \tag{3.2}$$

  To implement 3.2, the numbers $x_{i,nm}$ are computed and stored in a matrix X_i'. The maximum time of flight τ_{max} is used to make a mask matrix M which is then

[2]This is the rectangular rule approximation.

used to select the short trajectories[3] using element-wise multiplication $X_i = X_i' * M$ [36, 39]. Then, the columns of X_i are summed over, and a vector with entries $x_i(t_m)$ is obtained.

- **Spectrum:** the spectrum is obtained by performing a Fourier transform on the time-dependent dipole moment plus the fundamental field, with the following convention:

$$\tilde{x}_i(\omega_\nu) = \sum_j^{N-1} x_i(t_j) e^{i\omega_\nu t_j}, \tag{3.3}$$

  and plugging it in equation 2.76.

- **Displacements:** the displacements are computed using the approximated version of 2.71:

$$\chi_{\boldsymbol{k}}(t_m) \approx \sum_i e^{-i\boldsymbol{k}\cdot\boldsymbol{R}_i} \tilde{g}_i(\omega_\nu/c)\delta t \sum_{n=o}^{m} x(t_n) e^{i\omega_{\boldsymbol{k}} t_n}. \tag{3.4}$$

3.3 Simulation Description

In this section, a short description including the goals and specifications of each simulation is provided. The simulations' code can be found in Appendix B.1.

- **Single atom:** the computations described in the previous section are performed considering a single atom placed in the center of the Gaussian beam. In other words, the calculations are performed with a single intensity value corresponding to the laser's peak intensity. The running time of the main code is 18.29 minutes. This simulation was used to aid in the understanding of the theory presented in the preceding sections and to compare it with the results in [17] and the few atoms simulation.

- **Few atoms:** here, four atoms are positioned as shown in Figure 3.2, where the intensity profile is also plotted. The distance between atoms is such that the interatomic interactions can be neglected. Additionally to the spectrum generated by the atoms shown in Figure 3.2, the cylindrical symmetry was exploited to obtain a few atoms spectrum and displacements. This was done by multiplying the contributions of atoms 1-4 by an effective number of atoms proportional to the square of their distance to the center of the beam, namely, 1, 7 611, 30 444, and 68 500 atoms, respectively.[4] The running time of the main code is 104.52 minutes. This simulation was used to understand the effects of a spatial distribution in the emitted radiation.

[3] In laboratories, experimentalists usually control the generation conditions so that only the short trajectories are phase-matched, effectively eliminating the contribution from long trajectories.

[4] This distribution was chosen ad-hoc to work within the limitations of the 64-bit Windows computer used to run the simulations. With this hardware, it was only possible to calculate distributions between 0 and 50 photons, given that the numbers $|\chi|^{2n}$ and $n!$ in equation 2.15 must be stored in a variable with higher precision for $n > 50$.

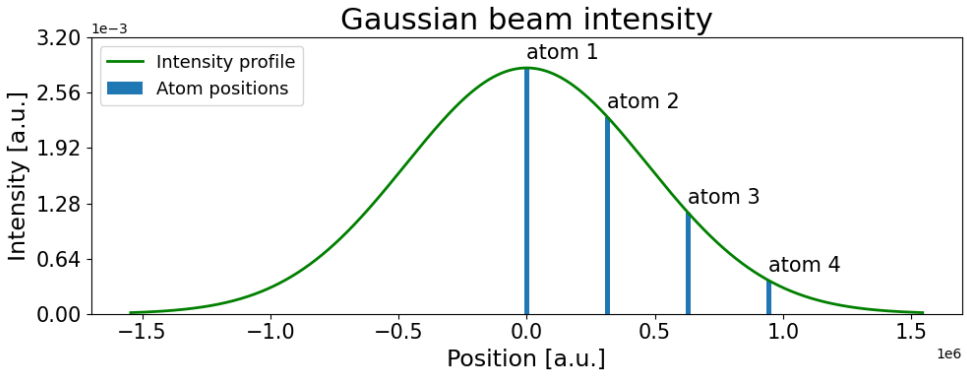

Figure 3.2: Plot of the laser intensity profile showing the positions of the four atoms.

3.4 Results and Discussion

3.4.1 Single atom

In this section, the results of the single atom simulation are presented and analyzed. The maximum kinetic energy and time of flight are obtained. The time-dependent dipole moment is presented and contrasted to the dipole moment from a similar simulation found in the literature. The resulting harmonic spectrum is shown and discussed. The displacements' time evolution in the optical phase space is analyzed. The final state's photon statistics and density matrices are graphically represented.

Kinetic Energy

The canonical momentum from equation 2.83 was used to obtain the mechanical momentum at a time t_m of an electron born at time t_n, i.e., $(P_{kin,i})_{nm} = (P_i)_{nm} + A(t_m)$, which in turn was used to obtain the kinetic energy $(E_{kin,i})_{nm} = (P_{kin,i})^2_{nm}/2$. The obtained kinetic energy matrix is plotted in panel a) of Figure 3.3. From this matrix a maximum kinetic energy value E_{max}, and its corresponding time of flight τ_{max} can be extracted. These quantities can be used to verify that the calculations are correct, as it is known that $E_{max} \approx 3.17 U_p$ and $\tau_{max} \approx 0.65\,T$, for a laser of period T [37]. Note, however, that the maximum energy relationship is specific to the case of a continuous waveform, where for every cycle there are possible ionization and recombination times with kinetic energy E_{max}. Nevertheless, here a finite duration pulse with varying intensity is used, and only one ionization time can be associated with a trajectory for which the maximum energy is reached.

In panel a) it can be seen that the electrons that escape the ion when the driving field is at maximum amplitude reach the highest energies at short times after the ionization. The maximum energy value in this matrix is found to be $E_{max} \approx 3.1687\,U_p$, which closely approximates the expected value from the semi-classical models. Moreover, this matrix element represents the energy at time $t = 629\,a.u.$ of an electron born at time $t_{exit} = 557\,a.u.$, corresponding to a time of flight $\tau_{max} \approx 0.65\,T$. Panel b) in Figure 3.3 shows the kinetic energy as a function of time for an electron born at time $t_{exit} = 557\,a.u.$, which can be interpreted in a semi-classical way as follows. The electron appears in the continuum and is accelerated away from the ion. After the field changes polarity (first local maximum), the electron is decelerated until it reaches velocity zero and then begins

to move in the other direction toward the ion. The electron goes by the ion's position and is decelerated again after another change of polarity (second local maximum). In the following, the electron continues to oscillate with a decreasing probability of recombination over time due to quantum diffusion. This plot is similar to that shown in FIG.1 of reference [10], where the authors plot the kinetic energy as a function of the return time, further validating the results presented here.

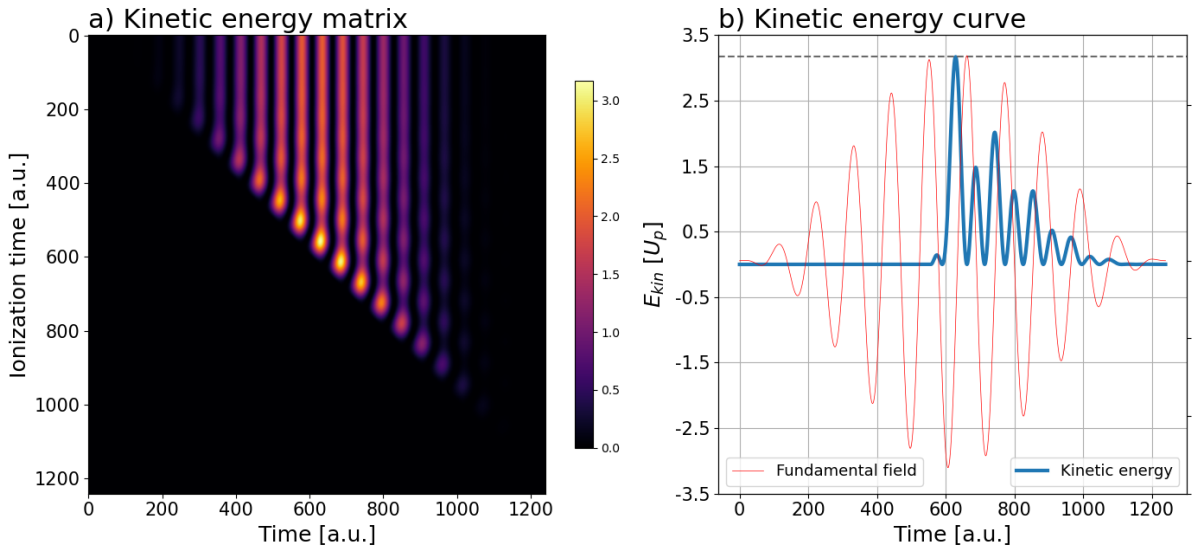

Figure 3.3: a)Plot of the time-dependent kinetic energy for different ionization times. b) Plot of the kinetic energy as a function of time for an electron born at time $t_{exit} = 557\,a.u.$ (thick blue line), and of the fundamental field represented in arbitrary units as reference (thin red line).

Dipole Moment and Spectrum

The time-dependent dipole moment calculated using equation 3.2 is plotted in Figure 3.4 alongside the fundamental field. As can be seen, the dipole moment response follows the fundamental field oscillations closely, revealing that the dominant spectral component is that of the fundamental frequency. However, the dipole moment's shape is not identical to that of the fundamental field, as it contains contributions from the other spectral components that make up the emission spectrum and affect the shape of the curve. The obtained dipole moment can be compared to the one plotted in Figure D.2 from reference [37], which is the result of a similar SFA simulation on hydrogen-like argon using a linearly-polarized driving field of the form $E(t) = E_0 \cos(t)$, with $I_0 = 1 \times 10^{14}\,W/cm^2$ and $\lambda = 1\,030\,nm$. The dipole moment obtained here holds a resemblance to the one shown in [37], with the main difference being the amplitude modulation of the dipole, which follows the raising and falling amplitude of the pulse, and a slight shape difference in the second half of the pulse with respect to the first half. This shape difference could be due to temporal interference between the leading and trailing parts of the pulse.

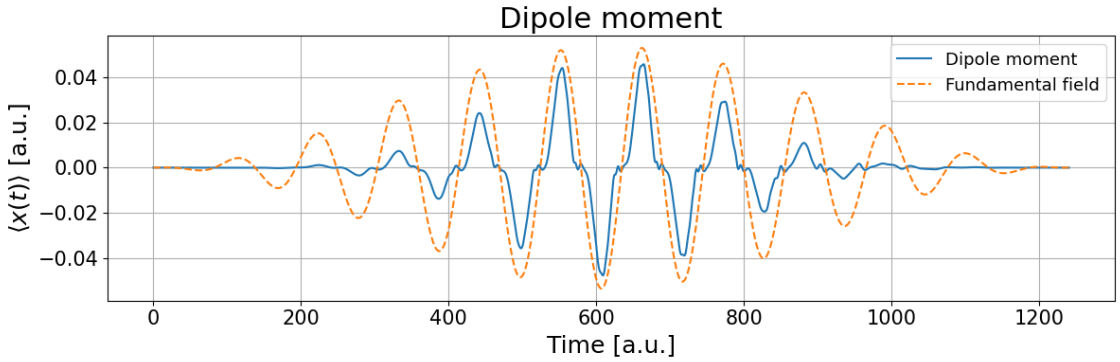

Figure 3.4: Plot of the dipole moment (blue solid line) and the fundamental field (orange dashed line) as a function of time.

The spectrum obtained from Fourier transforming the dipole moment shown in Figure 3.4 and then using equation 2.76 is plotted in Figure 3.5. Here, all the spectral components of the dipole moment and their relative strengths are represented, showing that the main contributions come from the first few harmonic orders, which present the highest intensity peaks. The harmonic intensities rapidly decrease for the low orders until the plateau is reached, where they stay somewhat constant. Later, the intensities rapidly decrease again for orders in the cutoff region. This spectrum can be compared with that shown in FIG.4 from reference [17], where they also consider hydrogen and use a finite pulse with the same peak intensity and central wavelength. The spectra are similar but not identical. The differences may arise from the fact that in [17] it is assumed that the driving laser populates more than one mode around the central frequency. Additionally, they take the pulse's vector potential to have the shape in equation 2.88 instead of the electric field. Nevertheless, the spectrum in Figure 3.5 reproduces the three distinctive regions in an HHG spectrum: the perturbative regime for harmonics 5 and lower, the plateau for harmonics between 5 and 19, and the cutoff region after harmonic 19.

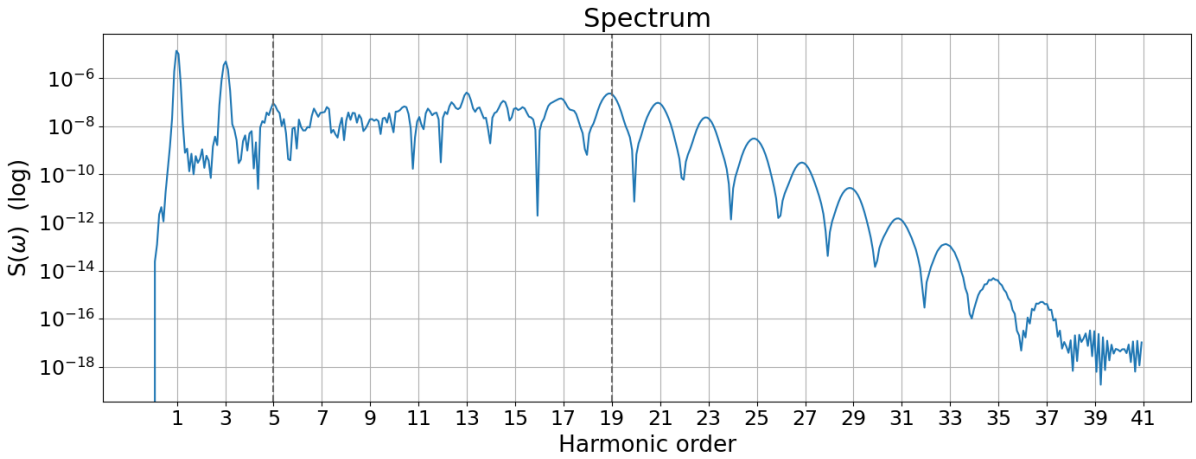

Figure 3.5: a) Plot of the HHG spectrum showing the perturbative regime, the plateau, and the cutoff.

Mode Displacements

Equation 3.4 was used to compute the time evolution of each harmonic displacement during the interaction. The time evolution for harmonic 13 is plotted in Figure 3.6 (figures for harmonics 1-27 can be found in Appendix C.1.1). As it can be seen in panel a), the

magnitude of the displacement begins to grow as the interaction starts, oscillating around a central value that increases approaching the final magnitude at the end of the pulse. From panel b), it can be concluded that the time evolution during the interaction involves counterclockwise rotation around the origin, as could also be deduced from equation 2.71. Finally, panel c) shows the state's trajectory in the optical phase space as the mode begins to get populated due to the interaction, resulting in a final displacement marked with a red dot. Note that this is related to the evolution of the radiation's quantum state in the rotating frame of reference resulting from applying the transformation $\hat{U}_1(t) = \exp(i\hat{H}_R t/\hbar)$. It is the final displacement that corresponds to the emitted radiation stationary state $|\chi_{\boldsymbol{k},l}\rangle$, which in the lab frame of reference has a coherent state evolution in the phase space.

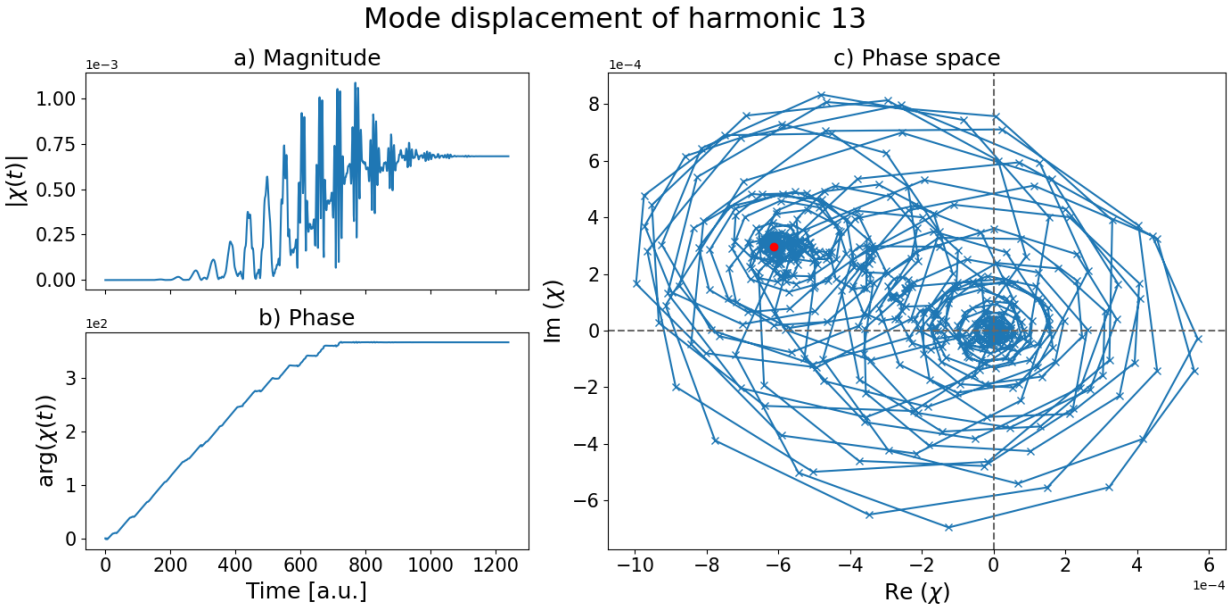

Figure 3.6: a) Plot of the displacement magnitude as a function of time for harmonic 13. b) Plot of the displacement phase as a function of time for harmonic 13. c) Plot of the displacement time evolution in the optical phase space for harmonic 13. The final displacement is marked with a red dot.

Having access to the quantum state of the radiation allows the analysis of the state's photon statistics. In the case of coherent states, the distributions will be Poissonian with Mandel parameter $Q = 0$, as discussed in subsection 2.1.1. For single atom HHG, the signal is too small to see any interesting statistics since the most probable photon number for all displacements is 0. Therefore, here the single atom displacements were multiplied by a number $\tilde{N}$ to amplify the effect. As seen in equation 2.15, to obtain the distribution, the computer must calculate $|\chi|^{2n}$ and $n!$ for each photon number n. This is limiting for the choice of $\tilde{N}$, given that the 64-bit Windows computer used to run the simulation can only compute the distribution for a limited magnitude of χ and n without throwing an overflow warning. With this in mind, it was chosen that $\tilde{N} = 9.7 \times 10^3$ so that the plateau harmonics show distributions between 0 and 50 photons in a range the computer can handle. The distributions for the plateau harmonics are shown in Figure 3.7, where it can be seen that the average photon number varies slightly from one harmonic to another. The relative intensity of the harmonics in the plateau depends on the atom used to generate them, and slight differences are expected. It is in the logarithmic scale that the intensities appear to be somewhat constant, and even then it can be seen in figure 3.5

that harmonic 13 is the most intense in the plateau.

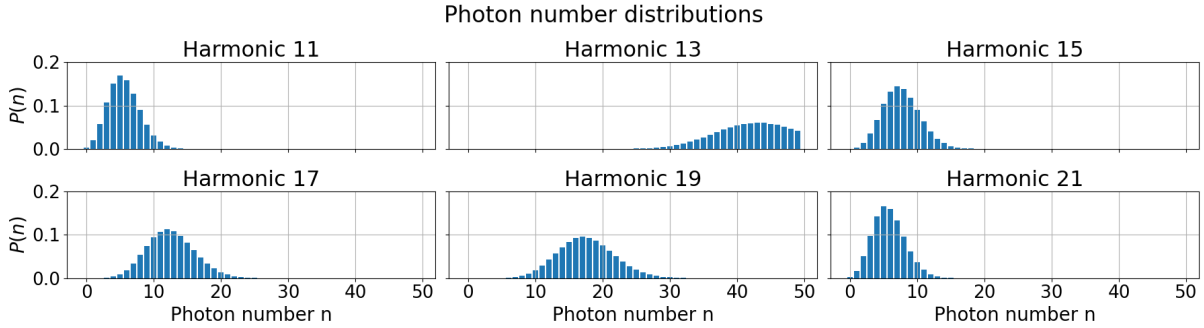

Figure 3.7: a)-f) Plots of the final state photon distributions (amplified signal) for harmonics 11-21.

The density matrices for each harmonic mode can be computed using the radiation's final (pure) state in equation 2.75. In Figure 3.8, the density matrices for harmonics 13, 15, and 17 are plotted (plots for other harmonics can be found in Appendix C.1.2). The density matrices show the expected shapes, where the diagonals correspond to the Poissonian distributions in Figure 3.7. The phases of the matrix elements are determined by the expression

$$\rho_{nm} = \frac{e^{-|\chi|^2}|\chi|^{n+m}}{\sqrt{n!m!}} e^{i\arg(\chi)(n-m)}. \tag{3.5}$$

Then the phase of the matrix elements depends on $\arg(\chi)$, which itself depends on the phase that the electron acquires during the propagation in the continuum, and $(n-m)$. The factor $(n-m)$ in the exponential slowly cycles from right to left through the color bars in Figure 3.8 as we move through the matrix anti-diagonal. Thus, the magnitude of $\arg(\chi)$ will determine the speed with which the matrix elements' phase cycles through the color bar, while the sign will determine the direction. For example, harmonic 13 shows very fast variation from right to left, consistent with the final displacement phase shown in Figure 3.6, which is larger than $3\pi/4$. Similarly, it can be seen in the figures from Appendix C.1.1 that harmonic 15's final displacement phase is close to $-\pi$ while harmonic 17's final displacement phase is close to $3\pi/4$, yielding fast variations as well.

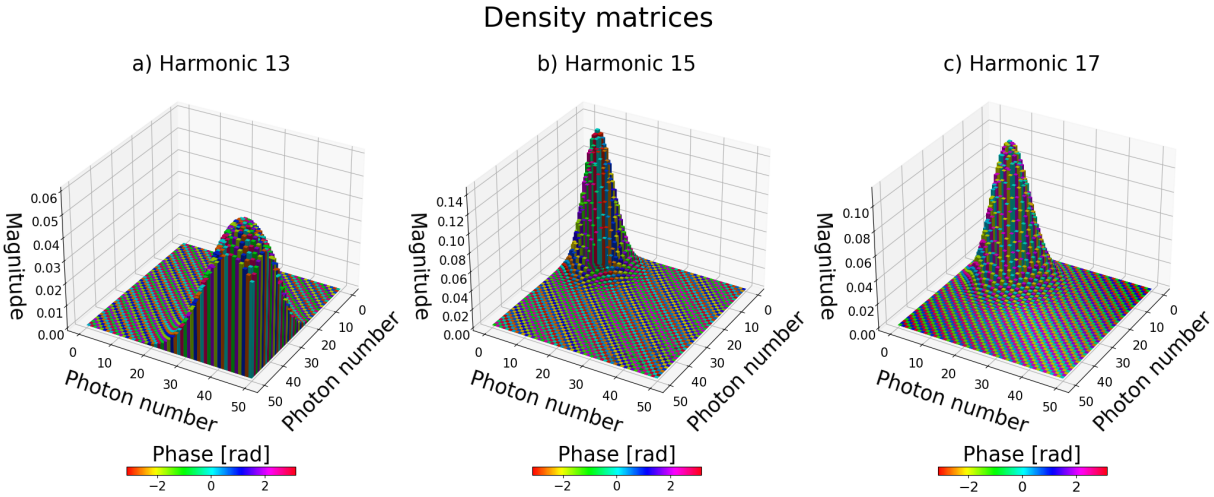

Figure 3.8: a)-c) Plots of the final state density matrices for harmonics 13, 15, and 17.

3.4.2 Few Atoms

In this section, the results of the few atoms simulation are presented. The harmonic spectrum generated by the four atoms is analyzed and compared with the single atom spectrum. The displacements' time evolution in the optical phase space is discussed. The response is multiplied by an effective number of atoms as described in section 3.3, and the resulting spectrum and displacements are presented. The final state's photon statistics and density matrices are graphically represented.

Dipole Moments and Spectra

The resulting dipole moments for each atom are shown in Figure 3.9. Once again, the dipole moments obtained here are similar to the one in [37], with the same differences as in the single atom case. The dipole moment curve obtained for atom 1 matches that obtained in the single atom simulation since they are equivalent systems. The curves for atoms 2-4 illustrate how the strengths of the responses are proportional to the field intensity. Furthermore, in the curve for atom 4, it can be seen that both at the beginning and end of the pulse, there is no response since the intensity is not high enough.

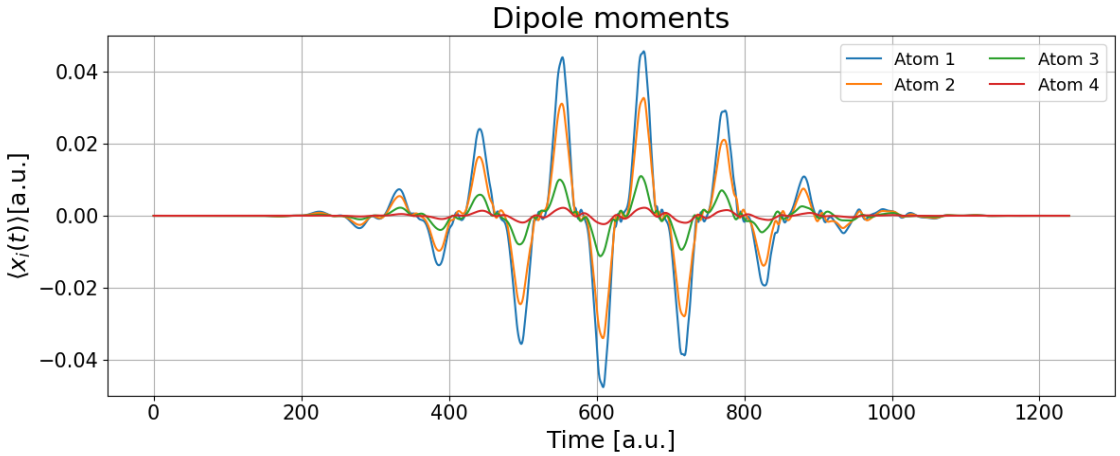

Figure 3.9: Plot of the dipole moment for atom 1 (blue line), atom 2 (orange line), atom 3 (green line), and atom 4 (red line).

The obtained spectra are plotted in Figure 3.10. In panel a), the spectra for each atom are shown. Here it can be seen that as the intensity decreases, the cutoff moves to the left until there is no plateau (atom 4). In panel b), the harmonic phase for each atom is also plotted. These phases play an important role when adding the spectra, and they also affect the duration of the pulse train. In the plateau region, the phases are expected to be quadratic in the harmonic order [40]. However, the ones obtained here don't present this relationship. Later in this section, the phases for the harmonic displacements are discussed. In this instance, the phases look quadratic in the cutoff region and somewhat constant in the plateau. The source of this discrepancy was not identified or understood and it is left for future work. In panel c), the total spectrum and the single atom spectrum are plotted for comparison. It can be seen that the intensities in the 4-atom spectrum are larger, and the peaks are better defined around the harmonics. Other than that, the differences are minimal as expected from the equations presented in subsection 2.2.3.

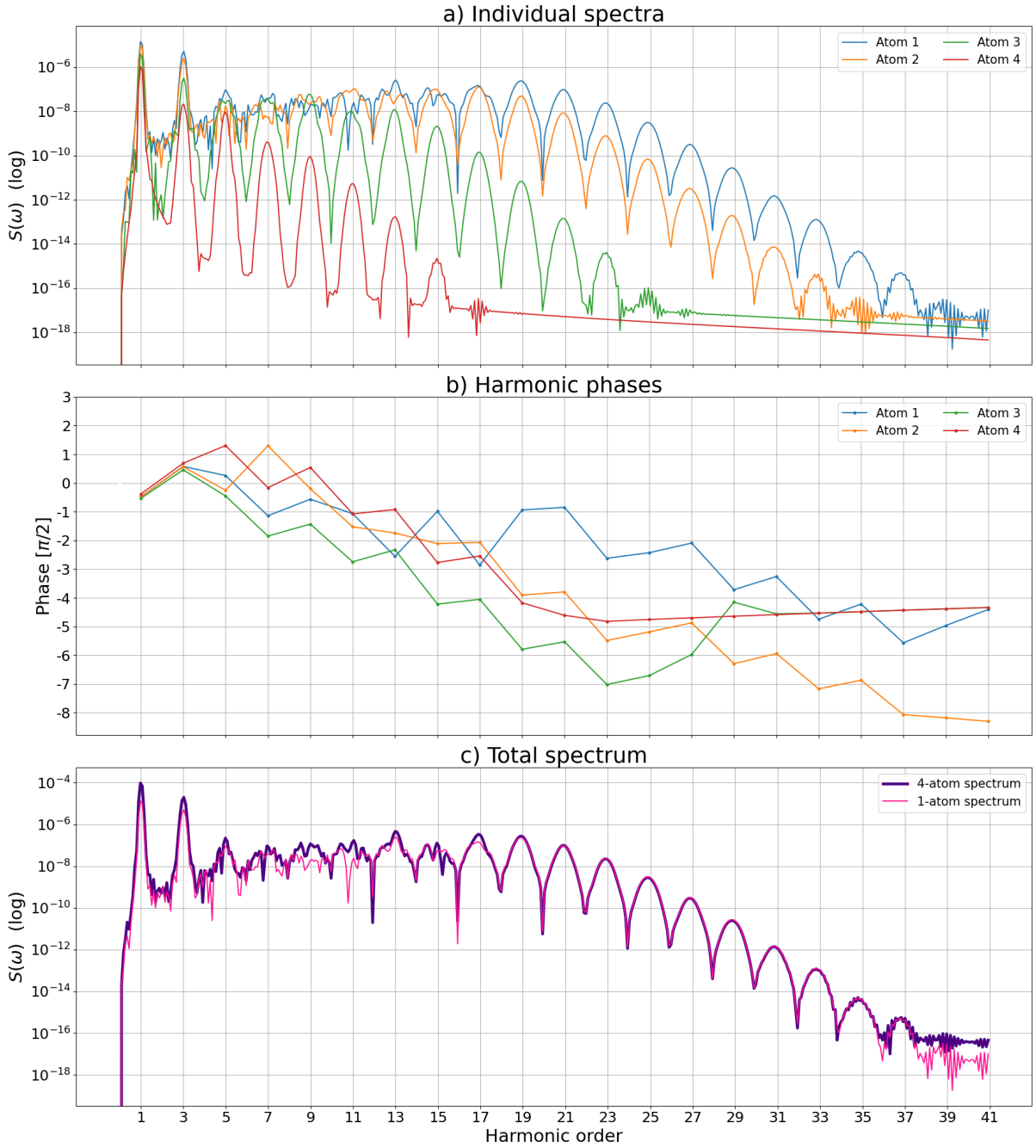

Figure 3.10: a) Plot of the individual spectra obtained for atom 1 (blue line), atom 2 (orange line), atom 3 (green line), and atom 4 (red line). b) Plot of the unwrapped harmonic phases for atom 1 (blue line), atom 2 (orange line), atom 3 (green line), and atom 4 (red line). c) Plot of the total spectrum (thick purple line) compared with the single atom spectrum (thin pink line).

Mode Displacements

The time evolution plots for harmonics 1-27 can be found in Appendix C.2.1. Here in Figure 3.11, the final displacements' a) magnitudes and b) harmonic phases are plotted for the four atoms, and the single atom simulations. In this case, the phases in panel b) present the expected quadratic dependence in the cutoff region and are fairly constant in the plateau, except for harmonic 15 in the single atom case. The magnitudes in panel a) are not very different, as the contributions of the atoms in the lower intensity zones are weak compared to the response of the atom at the center of the beam.

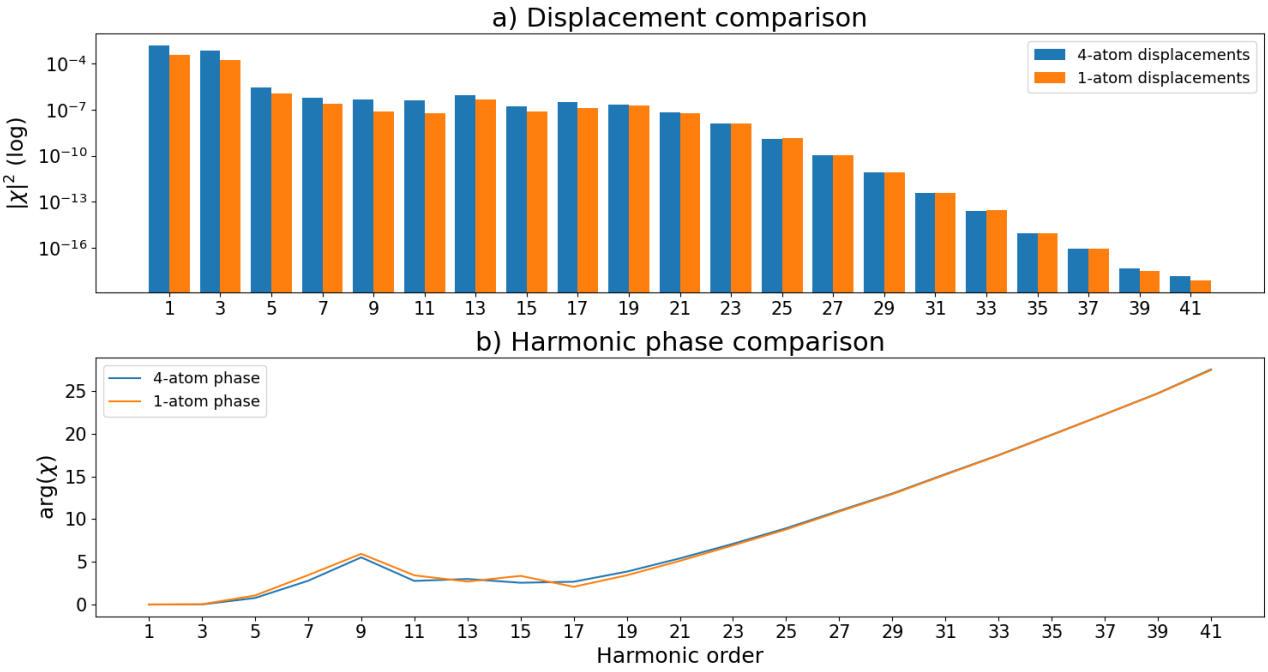

Figure 3.11: a) Plot of the displacements' magnitudes for the single atom (orange) and few atoms (blue) simulation. b) Plot of the unwrapped harmonic phases for the single atom (orange) and few atoms (blue) simulation.

When looking at the final state's photon statistics, the same problem as with the single atom simulation arises. The emission from the 4 atoms alone is not strong enough to show a distribution. Similarly to the single atom case, a number for each atom contribution was chosen to show statistics within the 50 photon range. In this case, exploiting the cylindrical symmetry of the beam, the individual atoms' emission was multiplied by an effective atom number $D_i \propto d_i^2$, where d_i is their distance to the center. As a result, the response of the outer atoms was amplified, yielding a new emission spectrum (without the fundamental field) and displacements shown in Figure 3.12. As can be seen, harmonics 11 and 13 are much stronger than harmonics 15-19, and the cutoff has moved to harmonic 17.

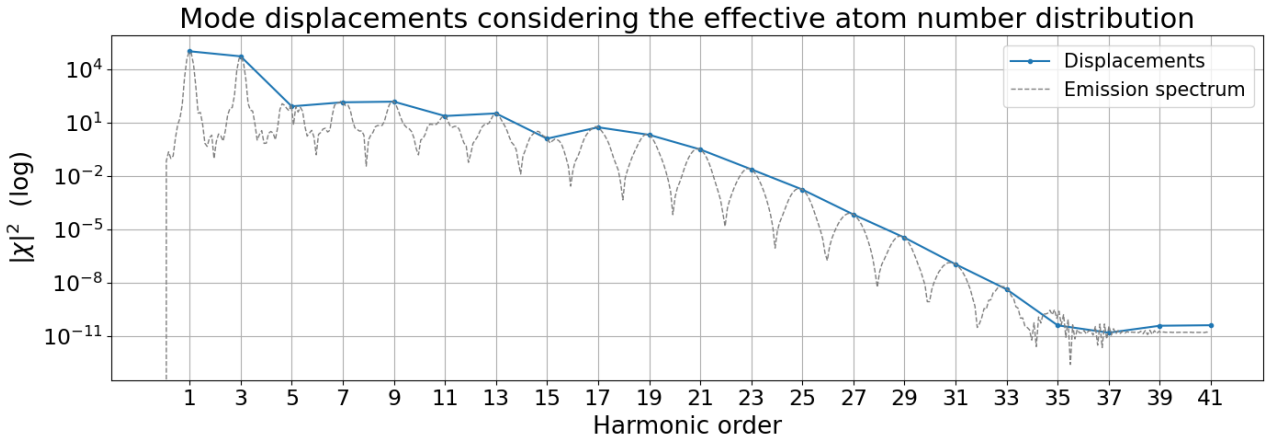

Figure 3.12: Plot of the mode displacements' amplitude (blue solid line) and emission spectrum (gray dotted line) after being multiplied by an effective number of atoms. The emission spectrum does not include the fundamental driving field.

Considering the displacements in Figure 3.12, the photon number distributions shown in Figure 3.13 were obtained. The distributions show the expected behavior for Poissonian distributions, which spread larger for bigger average photon numbers and become localized for smaller average photon numbers.

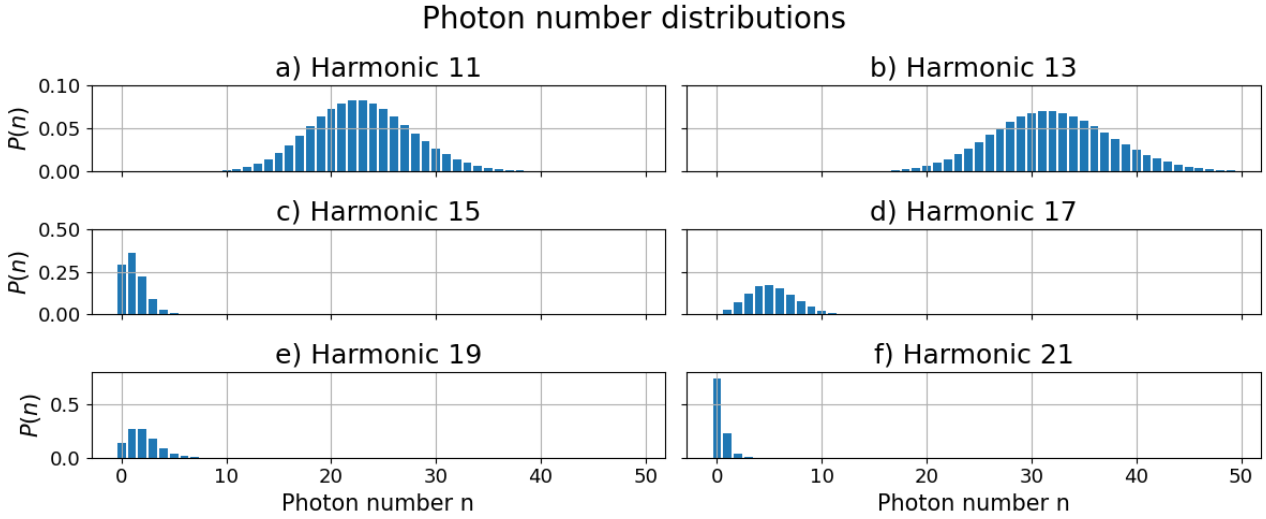

Figure 3.13: Plot of the photon number distributions for harmonics 11-21.

Similarly, the density matrices shown in Figure 3.14 were calculated using the displacements in Figure 3.12 (plots for harmonics 7-27 can be found in Appendix C.1.2). Once again, they present the expected shapes and phases.

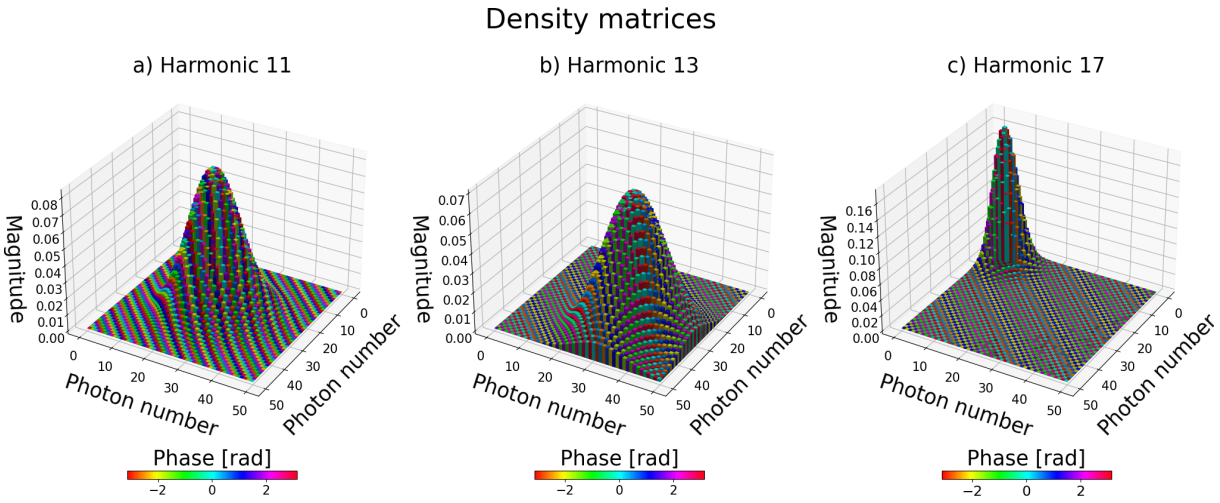

Figure 3.14: a)-c) Plots of the final state density matrices (considering the effective number of atoms) for harmonics 11, 13, and 17.

Chapter 4

Conclusions and Outlook

4.1 Summary and Conclusions

In this thesis, the history of harmonic generation was discussed, and the use of QED to describe HHG was motivated. The basic formalism necessary to describe light with quantum mechanics was reviewed. Different states of light were studied and compared. Later, the light-matter interaction Hamiltonian was introduced and simplified to be used in the specific case of HHG. The formalism to solve the time-dependent Schrödinger equation was laid out in detail, proposing an approach that incorporates elements from different methods found in the literature. The procedure to separate the problem into two parts, one equivalent to the known semi-classical scheme and one corresponding to the quantum corrections, was delineated. The selected method to solve the semi-classical problem, SFA, was described along with its most relevant equations. The specific conditions and methods used in the simulations were presented, and the particularities of each simulation were discussed. Finally, the results of both simulations were described, analyzed, and contrasted with each other and with similar simulations found in the literature.

The work conducted here provided a deep understanding of HHG and its underlying physics. The single atom simulation served as a simple example that could be used to explore and understand all the theory that was presented in this thesis. Once the results from this simulation were understood, expanding the code to multiple atoms was more accessible. The results from the few atoms simulation served to illustrate the effects of considering the spatial distribution, which affects the shape and intensity of the emission spectrum. After reviewing the literature and carrying out the simulations, it was clear that considering a spatial distribution would not impact the purity of the final state when generating in atoms, or yield states of light other than coherent states. Still, from a theoretical point of view, an interesting feature of HHG was highlighted by using SFQED to describe it. As was briefly discussed at the end subsection 2.2.3, when considering the incoherent contributions to the generation, the radiation's final state presents quantum features such as sub-Poissonian statistics for some spectral components [16]. Since these contributions are only relevant for generation in a small number of atoms, an apparent 'loss of quantumness' occurs when transitioning from the few atoms regime to the many atoms regime. In the outlook section, it is discussed how the removal of certain assumptions can enable the study of the quantum features in the few atoms regime. Additionally, experimentally realizable schemes where the final radiation state obtained here can be conditioned to possess quantum features are also discussed as possible avenues to explore.

4.2 Outlook

In this work, it is found that in targets consisting of many atoms driven by classic light, the emitted harmonics are always described by coherent states. In this section, different possible paths to generate more interesting states of light are discussed.

4.2.1 Applications in Quantum Technology

Quantum light is considered a key element in the development of quantum technologies due to distinct features that present an advantage over other systems. On one hand, the electromagnetic environment for these states can be considered as the vacuum, making the optical system somewhat decoherence-free. This provides a clear advantage over matter particles when scaling to macroscopic sizes. On the other hand, quantum states of light can possess reduced noise or be entangled, unlike classical light. Nevertheless, the applicability of these states is restricted by their low photon number since the engineering of high photon number quantum states is challenging.

In references [2, 17, 18], methods to produce entanglement between different field modes or to engineer Schrödinger Cat states using HHG's final radiation state are developed. This highlights the potential of using HHG to generate high photon number quantum states with important applications in quantum technologies.

4.2.2 HHG Driven by Quantum Light

In references [41, 42], HHG driven by different states of light, such as squeezed light or Fock states, was studied. It was found that the statistics of the driving field affect the characteristics of the HHG spectrum, and therefore the features of the resulting APT. In the previous subsection, the engineering of intense Schrödinger Cat states from HHG radiation was discussed. An alternative that hasn't been explored in the literature yet is the possibility of driving the HHG process with this intense cat state again in order to study the effects on the spectrum and APT.

4.2.3 Generation in Complex Targets

With the treatment used in this thesis, it was concluded that generation in more than one atomic target results in coherent light with no quantum features. In reference [43], where they analyze generation in H_2^+ molecular ions considering that the dipole moment couples to the first exited level as well as the ground state of the molecule, they find that the final state presents entanglement between the electronic and radiation degrees of freedom. The electron-light hybrid entangled state has multiple applications within quantum technology. This result depends heavily on, among other things, the population of different bound states and electron localization. Therefore, considering complex targets for which the coupling to more than one bound state is important, can lead to more interesting final states.

4.2.4 Modifications on the Present Work

In the formulation given here, many simplifying assumptions are made. In particular, two of these assumptions have important effects on the quantum state of the emitted

radiation: (1) that the laser field only couples to the ground state of $\hat{H}_E$ when solving the semi-classical problem, and (2) that the total wave function can be written as the tensor product $|\psi(t)\rangle = |\psi_E(t)\rangle \otimes |\psi_R(t)\rangle$. These assumptions are reasonable when generating in a large number of atoms. Nevertheless, together they eliminate the quantum characteristics of the light from the analysis by not considering entanglement to the electronic state and excluding the incoherent contributions to the emission. If, from a fundamental point of view, one is interested in studying generation in small samples, it is necessary to remove these assumptions. Note that considering contributions from other bounded states means that the analytical solution given by the displacements χ is no longer available and time-dependent perturbation theory must be used.

4.3 Acknowledgments

I would like to thank my supervisors David Busto and Anne L'Huillier for their guidance, support, and invaluable insights throughout the entire process of researching and writing this thesis. David Busto has been an excellent teacher, always available to answer questions and help me find solutions. I am most grateful for his wonderful feedback, which was always sensible and incredibly helpful. Anne L'Huillier has been a constant source of inspiration, providing not only helpful advice but also encouragement during moments of doubt.

I would also like to extend my heartfelt gratitude to Stefanos Carlström, for his patience and kindness. I am particularly grateful for his generosity and willingness to share his expertise. Our conversations have significantly enriched and deepened the analysis carried out in this project.

Finally, I would like to thank the members of the Attolab group at the Atomic Physics Division in Lund for making me feel welcome, and for their collaborative spirit and valuable input.

Bibliography

[1] T. H. Maiman. Stimulated optical radiation in ruby. *Nat.*, 187:493–494, 8 1960.

[2] U. Bhattacharya, T. Lamprou, A. S. Maxwell, A. Ordóñez, E. Pisanty, J. Rivera-Dean, P. Stammer, M. F. Ciappina, M. Lewenstein, and P. Tzallas. Strong–laser–field physics, non–classical light states and quantum information science. *Rep. Prog. Phys.*, 86:094401, 9 2023.

[3] P. A. Franken, A. E. Hill, C. W. Peters, and G. Weinreich. Generation of optical harmonics. *Phys. Rev. Lett.*, 7:118–119, 8 1961.

[4] A. McPherson, G. Gibson, H. Jara, U. Johann, T. S. Luk, I. A. McIntyre, K. Boyer, and C. K. Rhodes. Studies of multiphoton production of vacuum-ultraviolet radiation in the rare gases. *J. Opt. Soc. Am. B*, 4:595, 4 1987.

[5] M. Ferray, A. L'Huillier, X. F. Li, L. A. Lompre, G. Mainfray, and C. Manus. Multiple-harmonic conversion of 1064 nm radiation in rare gases. *J. Phys. B At. Mol. Opt. Phys.*, 21:L31–L35, 2 1988.

[6] F. Krausz and M. Ivanov. Attosecond physics. *Rev. Mod. Phys.*, 81:163–234, 2 2009.

[7] K. C. Kulander, K. J. Schafer, and J. L. Krause. *Dynamics of Short-Pulse Excitation, Ionization and Harmonic Conversion*, pages 95–110. Plenum Press, New York, 1993.

[8] P. B. Corkum. Plasma perspective on strong field multiphoton ionization. *Phys. Rev. Lett.*, 71:1994–1997, 9 1993.

[9] J. L. Krause, K. J. Schafer, and K. C. Kulander. High-order harmonic generation from atoms and ions in the high intensity regime. *Phys. Rev. Lett.*, 68:3535–3538, 6 1992.

[10] M. Lewenstein, P. Balcou, M. Y. Ivanov, A. L'Huillier, and P. B. Corkum. Theory of high-harmonic generation by low-frequency laser fields. *Phys. Rev. A*, 49:2117–2132, 3 1994.

[11] J. L. Krause, K. J. Schafer, and K. C. Kulander. Optical harmonic generation in atomic and molecular hydrogen. *Chem. Phys. Lett.*, 178:573–578, 4 1991.

[12] K. C. Kulander. Multiphoton ionization of hydrogen: A time-dependent theory. *Phys. Rev. A*, 35:445–447, 1 1987.

[13] F. Ehlotzky. Harmonic generation in keldysh-type models. *Il Nuovo Cimento D*, 14:517–525, 5 1992.

[14] A. L'Huillier, M. Lewenstein, P. Salières, Ph. Balcou, M. Y. Ivanov, J. Larsson, and C. G. Wahlström. High-order harmonic-generation cutoff. *Phys. Rev. A*, 48:R3433–R3436, 11 1993.

[15] P. Antoine, A. L'Huillier, M. Lewenstein, P. Salières, and B. Carré. Theory of high-order harmonic generation by an elliptically polarized laser field. *Phys. Rev. A*, 53:1725–1745, 3 1996.

[16] A. Gorlach, O. Neufeld, N. Rivera, O. Cohen, and I. Kaminer. The quantum-optical nature of high harmonic generation. *Nat. Commun.*, 11:4598, 9 2020.

[17] P. Stammer, J. Rivera-Dean, A. Maxwell, T. Lamprou, A. Ordóñez, M. F. Ciappina, P. Tzallas, and M. Lewenstein. Quantum electrodynamics of intense laser-matter interactions: A tool for quantum state engineering. *PRX Quantum*, 4, 2023.

[18] M. Lewenstein, M. F. Ciappina, E. Pisanty, J. Rivera-Dean, P. Stammer, T. Lamprou, and P. Tzallas. Generation of optical schrödinger cat states in intense laser–matter interactions. *Nat. Phys.*, 17:1104–1108, 10 2021.

[19] P. Stammer, J. Rivera-Dean, T. Lamprou, E. Pisanty, M. F. Ciappina, P. Tzallas, and M. Lewenstein. High photon number entangled states and coherent state superposition from the extreme-ultraviolet to the far infrared. *Phys. Rev. Lett.*, 7 2021.

[20] P. Stammer. Theory of entanglement and measurement in high harmonic generation. *Phys. Rev. A*, 3 2022.

[21] H. Laurell, D. Finkelstein-Shapiro, C. Dittel, C. Guo, R. Demjaha, M. Ammitzböll, R. Weissenbilder, L. Neoričić, S. Luo, M. Gisselbrecht, C. L. Arnold, A. Buchleitner, T. Pullerits, A. L'Huillier, and D. Busto. Continuous-variable quantum state tomography of photoelectrons. *Phys. Rev. Res.*, 4:033220, 9 2022.

[22] H. Laurell, S. Luo, R. Weissenbilder, M. Ammitzböll, S. Ahmed, H. Söderberg, C. L. M. Petersson, V. Poulain, C. Guo, C. Dittel, D. Finkelstein-Shapiro, R. J. Squibb, R. Feifel, M. Gisselbrecht, C. L. Arnold, A. Buchleitner, E. Lindroth, A. F. Kockum, A. L'Huillier, and D. Busto. Measuring the quantum state of photoelectrons. 9 2023.

[23] R. Loudon. *The Quantum Theory of Light*. Oxford Univ. Press, 3 edition, 2000.

[24] P. Meystre. *Electromagnetic Field Quantization*, pages 29–74. Springer International Publishing, Cham, 2021.

[25] J. Zamastil and J. Benda. *Dynamics: The Nonrelativistic Theory*, pages 189–289. Springer International Publishing, Cham, 2017.

[26] R. J. Glauber. Coherent and incoherent states of the radiation field. *Phys. Rev.*, 131, 1963.

[27] D. Griffiths. *Chapter 8: Conservation Laws*, pages 356–381. Cambridge University Press, 6 2017.

[28] C. Cohen-Tannoudji, J. Dupont-Roc, and G. Grynberg. *Appendix*, pages 621–639. Wiley, 4 1998.

[29] S. A. Rashkovskiy. Nonlinear schrödinger equation and classical-field description of thermal radiation. *Indian J. Phys.*, 92:289–302, 3 2018.

[30] P. C. Aichelburg and H. Grosse. Exactly soluble system of relativistic two-body interaction. *Phys. Rev. D*, 16:1900–1911, 9 1977.

[31] K. Rzazewski and W. Zakowicz. Initial value problem and causality of radiating oscillator. *J. Phys. A Math. Gen.*, 9:1159–1170, 7 1976.

[32] K. Rzazewski and W. Zakowicz. Initial value problem for two oscillators interacting with electromagnetic field. *J. Math. Phys.*, 21:378–388, 2 1980.

[33] J. H. Eberly and M. V. Fedorov. Spectrum of light scattered coherently or incoherently by a collection of atoms. *Phys. Rev. A*, 45:4706–4712, 4 1992.

[34] J. C. Baggesen and L. B. Madsen. On the dipole, velocity and acceleration forms in high-order harmonic generation from a single atom or molecule. *J. of Phys. B: At. Mol. Opt.*, 44:115601, 6 2011.

[35] K. Amini, J. Biegert, F. Calegari, A. Chacón, M. F. Ciappina, A. Dauphin, D. K. Efimov, C. Figueira de Morisson Faria, K. Giergiel, P. Gniewek, A. S. Landsman, M. Lesiuk, M. Mandrysz, A. S. Maxwell, R. Moszyński, L. Ortmann, J. A. Pérez-Hernández, A. Picón, E. Pisanty, J. Prauzner-Bechcicki, K. Sacha, N. Suárez, A. Zaïr, J. Zakrzewski, and M. Lewenstein. Symphony on strong field approximation. *Rep. Prog. Phys.*, 82, 2019.

[36] J. M. Dahlström. Strong field approximation for high order harmonic generation with $\omega/2\omega$ laser fields. 2007.

[37] S. Carlström. Sub-cycle control of strong-field processes on the attosecond timescale. 2017.

[38] E. Mevel, P. Breger, R. Trainham, G. Petite, P. Agostini, A. Migus, J. P. Chambaret, and A. Antonetti. Atoms in strong optical fields: Evolution from multiphoton to tunnel ionization. *Phys. Rev. Lett.*, 70:406–409, 1 1993.

[39] P. Antoine, A. L'Huillier, and M. Lewenstein. Attosecond pulse trains using high–order harmonics. *Phys. Rev. Lett.*, 77:1234–1237, 8 1996.

[40] Y. Mairesse, A. de Bohan, L. J. Frasinski, H. Merdji, L. C. Dinu, P. Monchicourt, P. Breger, M. Kovacev, R. Taieb, B. Carre, H. G. Muller, P. Agostini, and P. Salieres. Attosecond synchronization of high-harmonic soft x-rays. *Science*, 302:1540–1543, 11 2003.

[41] M. E. Tsur, M. Birk, A. Gorlach, M. Krüger, I. Kaminer, and O. Cohen. High harmonic generation driven by quantum light: Strong-field approximation and attosecond pulses. page FW4B.1. Optica Publishing Group, 2022.

[42] A. Gorlach, M. E. Tzur, M. Birk, M. Krüger, N. Rivera, O. Cohen, and I. Kaminer. High-harmonic generation driven by quantum light. *Nat. Phys.*, 19:1689–1696, 11 2023.

[43] J. Rivera-Dean, P. Stammer, A. S. Maxwell, Th. Lamprou, E. Pisanty, P. Tzallas, M. Lewenstein, and M. F. Ciappina. Quantum optical analysis of high-order harmonic generation in h_2^+ molecular ions. 7 2023.

Appendix A

Coherent States

A.1 Coherent States are Eigenstates of $\hat{a}_{\boldsymbol{k},l}$

Here the proof that coherent states are eigenstates of the annihilation operator $\hat{a}_{\boldsymbol{k},l}$ with eigenvalue $\alpha_{\boldsymbol{k},l}$ is presented:

$$\begin{aligned}
\hat{a}_{\boldsymbol{k},l}|\alpha_{\boldsymbol{k},l}\rangle &= e^{-\frac{|\alpha_{\boldsymbol{k},l}|^2}{2}} \sum_{n=0}^{\infty} \frac{\alpha_{\boldsymbol{k},l}^n}{\sqrt{n!}} \hat{a}_{\boldsymbol{k},l}|n\rangle_{\boldsymbol{k},l} \\
&= e^{-\frac{|\alpha_{\boldsymbol{k},l}|^2}{2}} \sum_{n=1}^{\infty} \frac{\alpha_{\boldsymbol{k},l}^n}{\sqrt{n!}} \sqrt{n}|n-1\rangle_{\boldsymbol{k},l} \\
&= \alpha_{\boldsymbol{k},l} e^{-\frac{|\alpha_{\boldsymbol{k},l}|^2}{2}} \sum_{n=1}^{\infty} \frac{\alpha_{\boldsymbol{k},l}^{n-1}}{\sqrt{(n-1)!}} |n-1\rangle_{\boldsymbol{k},l} \\
&= \alpha_{\boldsymbol{k},l}|\alpha_{\boldsymbol{k},l}\rangle. \qquad \text{(A.1)}
\end{aligned}$$

A.2 Coherent States Have Poissonian Photon Number Distributions

Photon number fluctuations are defined as $\Delta n = \sqrt{\langle n^2\rangle - \langle n\rangle^2}$. Then, for a coherent state $|\alpha\rangle$:

$$\langle n\rangle = \langle\alpha|\hat{a}^\dagger\hat{a}|\alpha\rangle = |\alpha|^2, \qquad \text{(A.2a)}$$

$$\langle n^2\rangle = \langle\alpha|\hat{a}^\dagger\hat{a}\hat{a}^\dagger\hat{a}|\alpha\rangle = |\alpha|^2(\langle\alpha|\hat{a}^\dagger\hat{a}|\alpha\rangle + 1) = |\alpha|^4 + |\alpha|^2, \qquad \text{(A.2b)}$$

$$\Delta n = \sqrt{|\alpha|^4 + |\alpha|^2 - |\alpha|^4} = |\alpha|. \qquad \text{(A.2c)}$$

Appendix B

Numerical Implementation

B.1 Code

The single atom code is contained in the few atoms code, given that it is equivalent to considering the atom 1 in Figure 3.2. Therefore, only the few atoms code is presented here.

```
import time
import numpy as np
import matplotlib.pyplot as plt
import matplotlib.colors as cm
import scipy.special as scp #factorial function
from scipy.integrate import odeint,quad
from datetime import datetime
from matplotlib import animation
from matplotlib.animation import PillowWriter
#Parameters SI units
pint=1e14 #laser intensity W/cm2
wlen=8e-7 #wavelength m
pdur=30e-15 #pulse duration s
lrad=50e-6 #beam radius at focus m
ene=5e-3 #pulse energy J
iene=13.6 #ionization energy of hydrogen eV
#Conversion factors
length=1/5.291772e-11 #a.u./m
intensity=1/3.50945e16 #a.u./W/cm2
frequency=1/4.134137e16 #a.u./Hz
energy1=1/27.2113962 #a.u./eV
energy2=2.2937e17 #a.u./J
time1=1/2.418884e-17 #a.u./s
#Parameters in a.u.
pint=pint*intensity #laser intensity
wlen=wlen*length #wavelength
pdur=pdur*time1 #pulse duration
lrad=lrad*length #beam waist
ene=ene*energy2 #pulse energy
iene=iene*energy1 #ionization energy of hydrogen
c=137.04 #speed of light
eps0=4*np.pi #vacuum permittivity
#Variables in a.u.
amp=np.sqrt(pint) #electric field amplitude at x=0
freq=(2*np.pi*c)/wlen #driving laser frequency
wvec=2*np.pi/wlen #wave vector
```

```
    per=wlen/c #driving laser period
    ncyc=pdur*c/wlen #number of cycles
    efreq=np.pi/pdur #envelope frequency
    ponde=amp**2/(4*freq**2) #ponderomotive energy for atom 1
    cutoff=3.17*ponde+iene #cutoff energy for atom 1
    min_order=iene/freq+1 #first plateau order
    max_order=cutoff/freq #cutoff order
    print(" amp=",amp,"\n","freq=",freq,"\n","per=",per,"\n",
        "ncyc=",ncyc,"\n","efreq=",efreq, "\n",
        "lrad=",lrad,"\n","ponde=", ponde,"\n",
        "cutoff=", cutoff,"\n",
        "min_order=", min_order,"\n","max_order=", max_order)
    #Spatial distribution
    npos=4 #number of positions considered
    start=0 #first position
    stop=lrad #last position
    positions=np.linspace(start,stop,npos) #position array
    if npos>1: #separation between atoms
        dely=positions[1]-positions[0]
    else:
        dely=1
    print(positions)#Spatial distribution
    npos=4 #number of positions considered
    start=0 #first position
    stop=lrad #last position
    positions=np.linspace(start,stop,npos) #position array
    if npos>1: #separation between atoms
        dely=positions[1]-positions[0]
    else:
        dely=1
    print(positions)
    #Time array
    t0=0 #pulse starts at t0=0
    tf=pdur #pulse ends at tf=pdur
    delt=1 #time step
    t=np.arange(t0,tf,delt) #time values
    N=len(t) #number of points
        #Details for file names
    f=round(freq,3)
    dur=round(pdur/(time1*1e-15))
    inten=round(pint,3)
    date = datetime.now().strftime("%Y-%m-%d_%H-%M")
    #Define functions of the intensity
    I = lambda x: pint*np.exp((-2*x**2)/lrad**2) #intensity profile
    E0= lambda r: np.sqrt(I(r)) #field amplitude
    A_ = lambda am,y: am*(np.sin(2*efreq*y-freq*y)/(8*efreq-4*freq)
                          +np.sin(2*efreq*y+freq*y)/(8*efreq+4*freq)
                          -np.sin(freq*y)/(2*freq)) #vector potential
    E_ = lambda am,z: am*(np.sin(efreq*z))**2*np.cos(freq*z) #el. field
    Up = lambda s: I(s)/(4*freq**2) #ponderomotive energy
    #Fourier transform function
    def fourier(t,y):
        dt=t[1]-t[0]
        Dt=t[-1]-t[0]
        dw=2*np.pi/Dt
        T=len(t)
        omega=[]
        trans=[]
```

```
        for i in range(T):
            suma=0
            omega.append(dw*i)
            for j in range(T):
                suma=suma+(y[j]*np.exp(1j*t[j]*omega[i]))
            trans.append(suma)
        return omega,trans
    #Electric field and vector potential arrays
    EL=np.zeros([npos,N])
    VP=np.zeros([npos,N])
    maxel=np.zeros([npos])
    melin=np.zeros([npos], dtype=np.int_)
    for i in range(npos):
        EL[i,:]=E_(E0(positions[i]),t)
        VP[i,:]=A_(E0(positions[i]),t)
        maxel[i]=max(np.abs(EL[i,:]))
        melin[i]=np.where(np.abs(EL[i,:]) == maxel[i])[0][0]
    #Electron oscillation amplitude (Solving the initial value problem)
    d=[]
    tmax=[]
    for i in range(npos):
        def g(y,t): #define the system of differential equations
            v=y[1] #velocity
            a=E0(positions[i])*np.cos(freq*t)
            *(np.sin(np.pi*t/pdur))**2 #acceleration
            return [v,a]
        y0=[0,0]
        sol=odeint(g,y0,t) #solver
        x=sol[:,0].tolist() #positions
        d_osc=max(x) #oscillation amplitude
        tmax_osc=t[x.index(d_osc)]
        d.append(d_osc)
        tmax.append(tmax_osc)
    print (" tmax=",tmax,"\n","d=",d)
    #Form factor
    def gamma(k,i):
        gamma=np.sqrt(c*k/(2**6*np.pi**4))
        *(1/d[i])/np.sqrt((1/d[i])**2+k**2)
        return gamma
    #Compute momentum, action and dipole moment
    #Empty arrays
    p=np.zeros([N,N,npos],dtype=np.complex_)
    perr=np.zeros([N,N,npos],dtype=np.complex_)
    a=np.zeros([N,N,npos],dtype=np.complex_)
    aerr=np.zeros([N,N,npos],dtype=np.complex_)
    x=np.zeros([N,N,npos],dtype=np.complex_)
    pk=np.zeros([N,N,npos],dtype=np.complex_)
    Ek=np.zeros([N,N,npos],dtype=np.complex_)
    #Values are calculated for each each ionization time tn at time step
    tm
    initial=time.time()
    for i in range(npos):
        A = lambda y: E0(positions[i])*
                    (np.sin(2*efreq*y-freq*y)/(8*efreq-4*freq)
                    +np.sin(2*efreq*y+freq*y)/(8*efreq+4*freq)
                    -np.sin(freq*y)/(2*freq))
        E = lambda z: E0(positions[i])*(np.sin(efreq*z))**2
                    *np.cos(freq*z)
```

```
        for m in range(N):
            n=0
            while t[n]<t[m]:
                integral1,error1 = quad(A,t[n],t[m])
                p[n,m,i] = - (1.0/(t[m]-t[n]))*integral1
                perr[n,m,i] = error1
                pk[n,m,i] = p[n,m,i]+A(t[m])
                Ek[n,m,i] = (pk[n,m,i])**2/2/Up(positions[i])
                real_action = lambda r: np.real((p[n,m,i]+A(r))**2/2+
    iene)
                imag_action = lambda r: np.imag((p[n,m,i]+A(r))**2/2+
    iene)
                integral_real,error_real = quad(real_action,t[n],t[m])
                integral_imag,error_imag = quad(imag_action,t[n],t[m])
                a[n,m,i] = integral_real+1j*integral_imag
                aerr[n,m,i] = error_real+error_imag
                epsilon = 1e-10 #regulation constant
                C = (np.pi/(epsilon+1j*(t[m]-t[n])/2))**(3/2)
                dip = lambda w: (p[n,m,i]+A(w))/(1+(p[n,m,i]+A(w))**2)
    **3
                x[n,m,i] = delt*(1j*C*dip(t[m])
                                 *np.exp(-1j*a[n,m,i])*E(t[n])*dip(t[n])
                                  +np.conj(1j*C*dip(t[m])
                                  *np.exp(-1j*a[n,m,i])*E(t[n])*dip(t[n])
    ))
                n=n+1
     final=time.time()
     rt=final-initial
     print("Run time = ",rt/60," min")
     #Kinetik energy and maximum time of flight
     maximums=[]
     exits=[]
     returns=[]
     taus=[]
     times=[]
     for i in range(npos):
         maxi=np.amax(np.real(Ek[:,:,i]))
         ex=np.where(Ek[:,:,i] == maxi)[0][0]
         ret=np.where(Ek[:,:,i] == maxi)[1][0]
         tim=(ret-ex)*delt
         tau=tim/per
         maximums.append(maxi)
         exits.append(ex)
         returns.append(ret)
         taus.append(tau)
         times.append(tim)
     print("Max kinetic energy= " , maximums)
     print("Max time of flight= " , times , " a.u.")
     print("Max time of flight= ", taus, "T")
     #Mask for selecting short trajectories
     pondes=int2/(4*freq**2) #ponderomotive energies array
     scale=2**7*(2*iene)**(5/2)/np.pi**2 #constant multiplying the dipole
     moment
     flight_max=per*taus[0] #define a maximum time of flight
     M=int(flight_max*N//pdur) #number of timesteps in the maximum time
    of flight
     Mask=np.zeros([N,N])
     m=0
```

```
    for m in range(N): #make the mask
        if m<M:
            for n in range(M):
                Mask[n,m]=1
        else:
            n=m
            while n>m-M:
                Mask[n,m]=1
                n=n-1
    Dipole=np.zeros([N,N,npos])
    for i in range(npos): #select trajectories
        Dipole[:,:,i]=np.real(x[:,:,i]*Mask)
        X1=np.transpose(np.sum(Dipole,axis=0)*scale)
    #Fourier transform the dipole moments
    X=np.zeros([npos,N])
    X=X1+EL
    last=41 #last harmonic to show
    sp=[]
    sp1=[]
    om,throw= fourier(t,X1[0,:]) #get the frequency array
    om=np.array(om)
    index=np.argmin(np.abs(om-last*freq))
    w=np.array(om)[:index]
    order=w/freq
    ords=[]
    for i in range(1,last+1): #make and order array
        if i%2!=0:
            ords.append(i)
    S=len(ords)
    for i in range(npos): #fourier transform the dipoles
        throw,fo = fourier(t,X[i,:])
        fo = np.array(fo)[:index]
        fou = fo*gamma(w/c,i)
        throw,fo1 = fourier(t,X1[i,:])
        fo1=np.array(fo1)[:index]
        fou1=fo1*gamma(w/c,i)
        sp.append(fou)
        sp1.append(fou1)
    specs=np.array(sp)
    specs1=np.array(sp1)
    #Choose the one with electric field: specs
    Tspec=np.sum(specs,axis=0) #add all the contribution
    spectrum=(np.abs(Tspec)*w)**2 #total spectrum
    aspecs=(np.abs(specs)*w)**2 # individual spectrums
    #Harmonic Displacements
    initial=time.time()
    #effective number of atoms
    natoms=[int(np.pi*positions[i]**2/(130*dely)) for i in range(npos)]
    natoms[0]=1
    q=50
    num=range(q)
    gx=np.zeros([npos,N],dtype=np.complex_)
    prob=np.zeros([S,N,q])
    chi=np.zeros([S,N],dtype=np.complex_)
    schi=np.zeros([S,N])
    altchi=np.zeros([S,N],dtype=np.complex_)
    saltchi=np.zeros([S,N])
    chi_sa=np.zeros([npos,S,N],dtype=np.complex_)
```

```
    schi_sa=np.zeros([npos,S,N])
    m=0
    s=0
    for s in range(S): #for each order
        for m in range(N): #for each time
            sum1=np.zeros([npos],dtype=np.complex_)
            for i in range(npos): #for each atom
                wv=ords[s]*freq/c #wave vector corresponding to each
order
                gx[i,:]=gamma(wv,i)*X1[i,:]
                j=0
                while t[j]<t[m]: #copute displacements
                    sum1[i]=sum1[i]
                            +(delt*np.exp(1j*ords[s]*freq*t[j])*gx[i,j])
                    j=j+1
                chi_sa[i,s,m]=sum1[i]
                schi_sa[i,s,m]=np.real(chi_sa[i,s,m]
                                *np.conj(chi_sa[i,s,m]))
            sum2=np.sum(natoms*sum1) #with effective number of atoms
            sum3=np.sum(sum1) #without effective number of atoms
            chi[s,m]=sum2
            schi[s,m]=np.real(chi[s,m]*np.conj(chi[s,m]))
            #Photon statistics
            altchi[s,m]=sum3
            saltchi[s,m]=np.real(altchi[s,m]*np.conj(altchi[s,m]))
            for n in num:
                pr=schi[s,m]**n*np.exp(-schi[s,m])/np.math.factorial(n)
                prob[s,m,n]=pr
    nprob=np.copy(prob)
    final=time.time()
    rt=final-initial
    print("Run time = ",rt/60," min")
    #Spectrum after multiplying by natoms
    sp2=[]
    for i in range(npos):
        om2,fou2 = fourier(t,X1[i,:])
        fou2=np.array(fou2)[:index]*natoms[i]*gamma(w/c,i)
        sp2.append(fou2)
    specs2 = np.array(sp2)
    Tspec2=np.sum(specs2,axis=0) #add all the contribution
    spectrum2=np.abs(Tspec2)**2
```

Appendix C

Results

C.1 Single atom

C.1.1 Mode Displacements

In this appendix, figures showing the time evolution of displacements 1 to 27 are included.

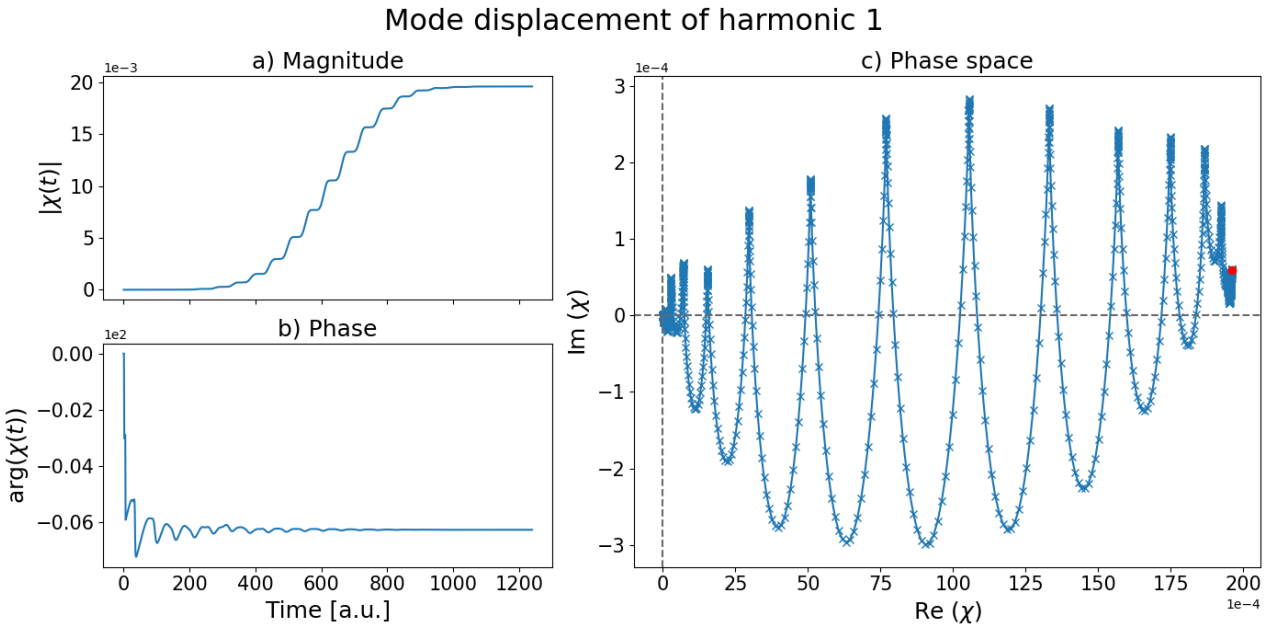

Figure C.1: a) Plot of displacement 1's magnitude as a function of time. b) Plot of displacement 1's phase as a function of time. c) Plot of displacement 1's time evolution in the optical phase space. The final displacement is marked with a red dot.

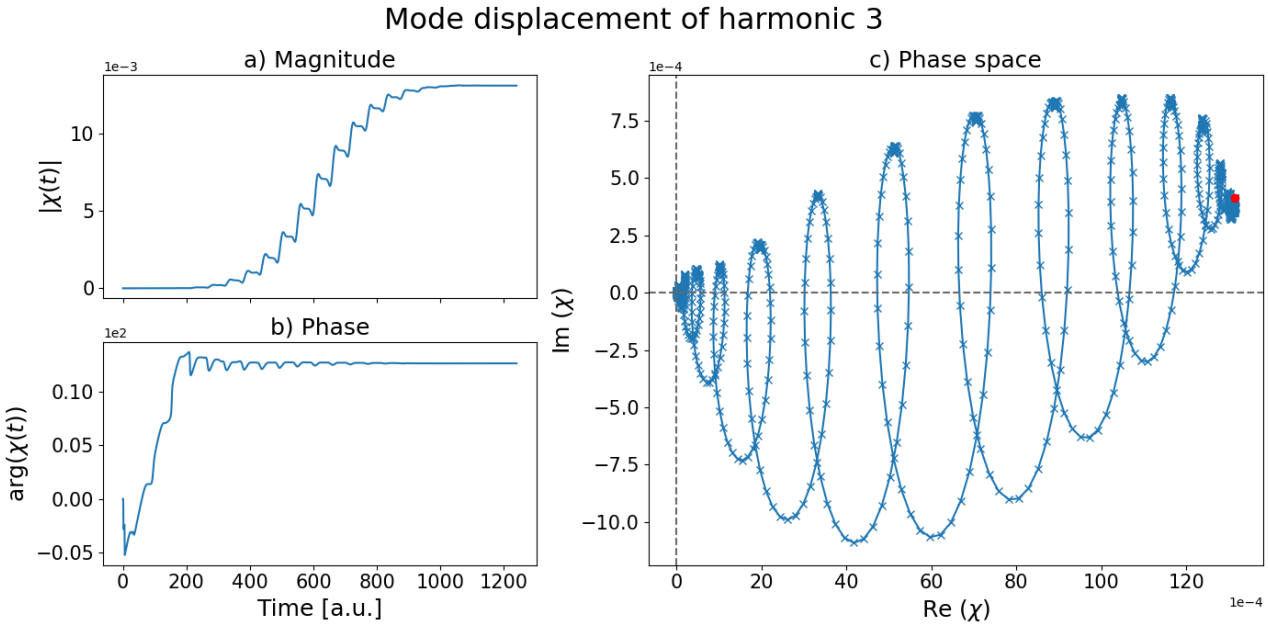

Figure C.2: a) Plot of displacement 3's magnitude as a function of time. b) Plot of displacement 3's phase as a function of time. c) Plot of displacement 3's time evolution in the optical phase space. The final displacement is marked with a red dot.

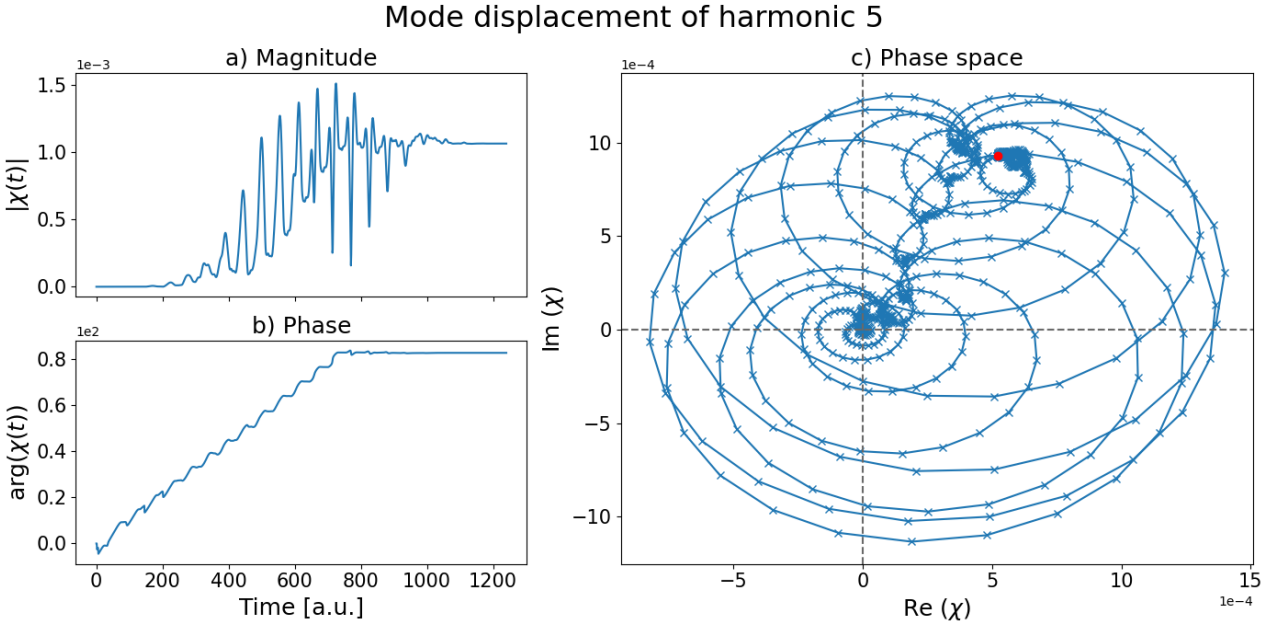

Figure C.3: a) Plot of displacement 5's magnitude as a function of time. b) Plot of displacement 5's phase as a function of time. c) Plot of displacement 5's time evolution in the optical phase space. The final displacement is marked with a red dot.

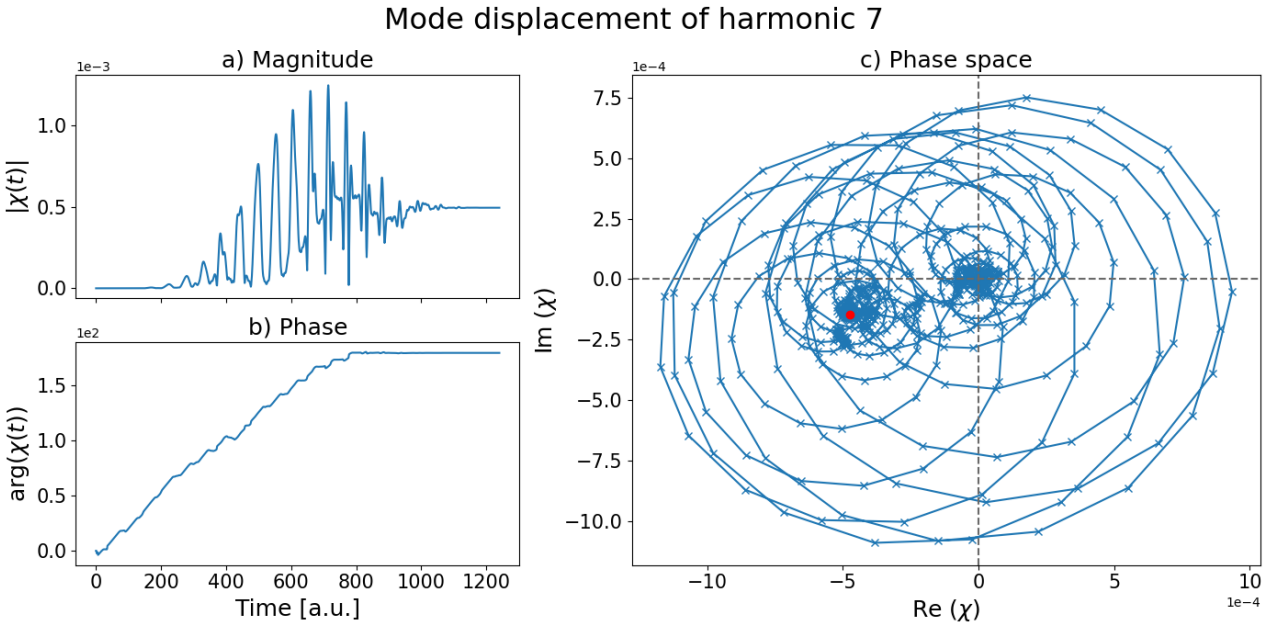

Figure C.4: a) Plot of displacement 7's magnitude as a function of time. b) Plot of displacement 7's phase as a function of time. c) Plot of displacement 7's time evolution in the optical phase space. The final displacement is marked with a red dot.

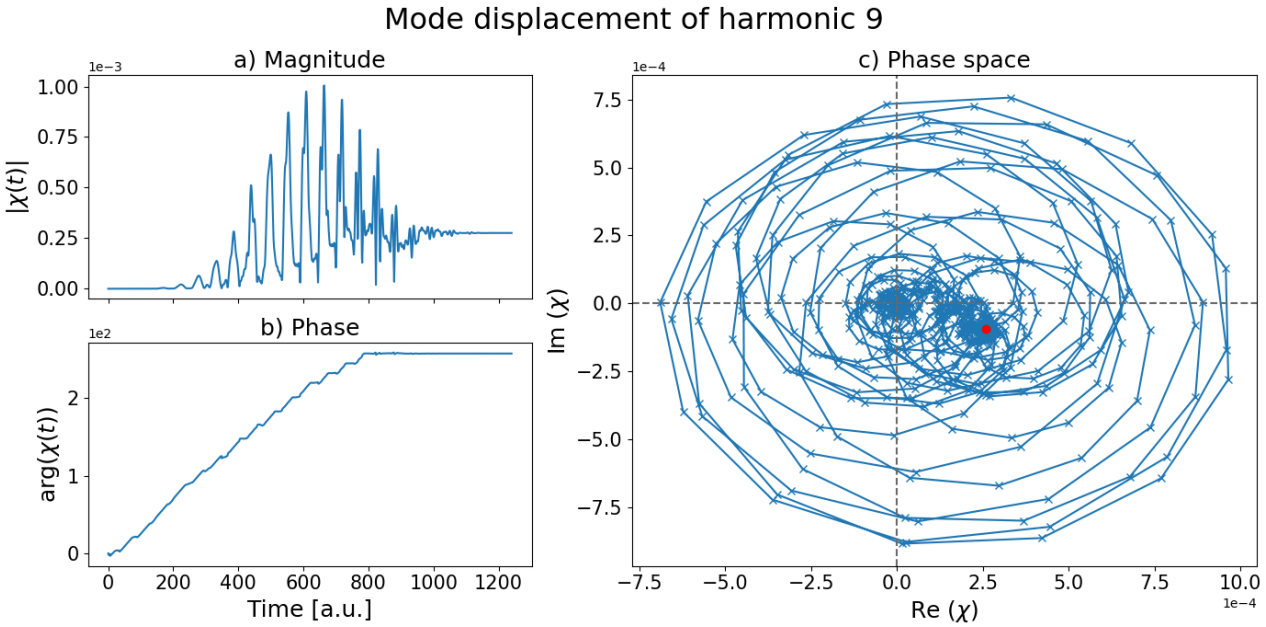

Figure C.5: a) Plot of displacement 9's magnitude as a function of time. b) Plot of displacement 9's phase as a function of time. c) Plot of displacement 9's time evolution in the optical phase space. The final displacement is marked with a red dot.

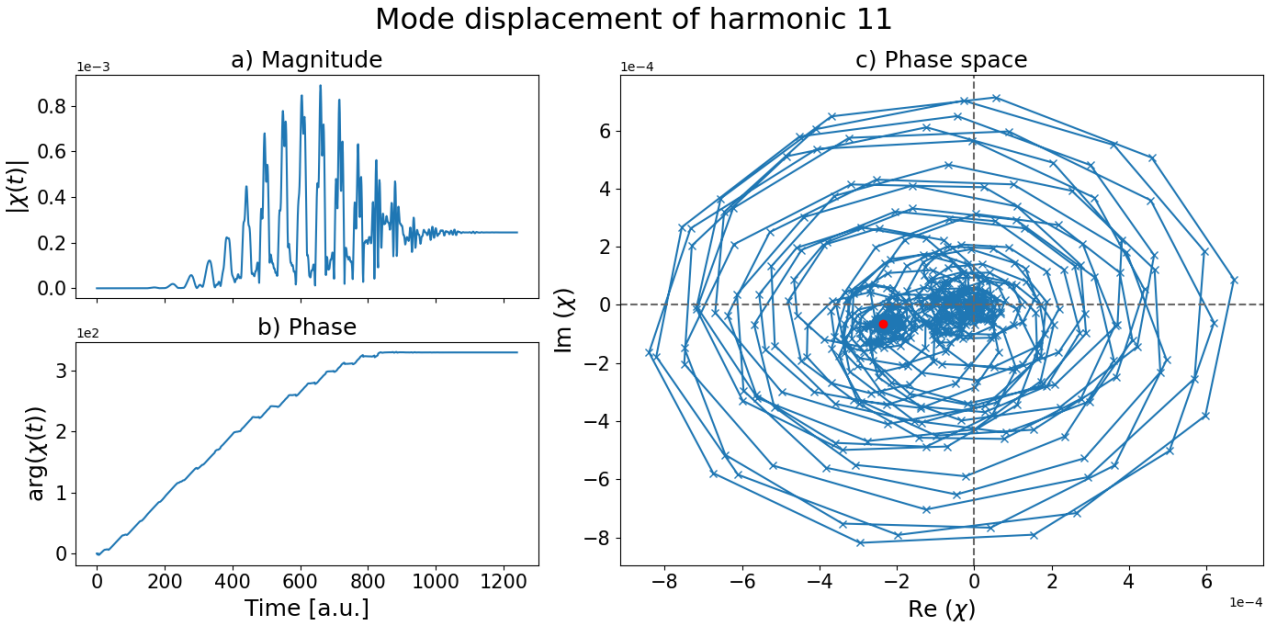

Figure C.6: a) Plot of displacement 11's magnitude as a function of time. b) Plot of displacement 11's phase as a function of time. c) Plot of displacement 11's time evolution in the optical phase space. The final displacement is marked with a red dot.

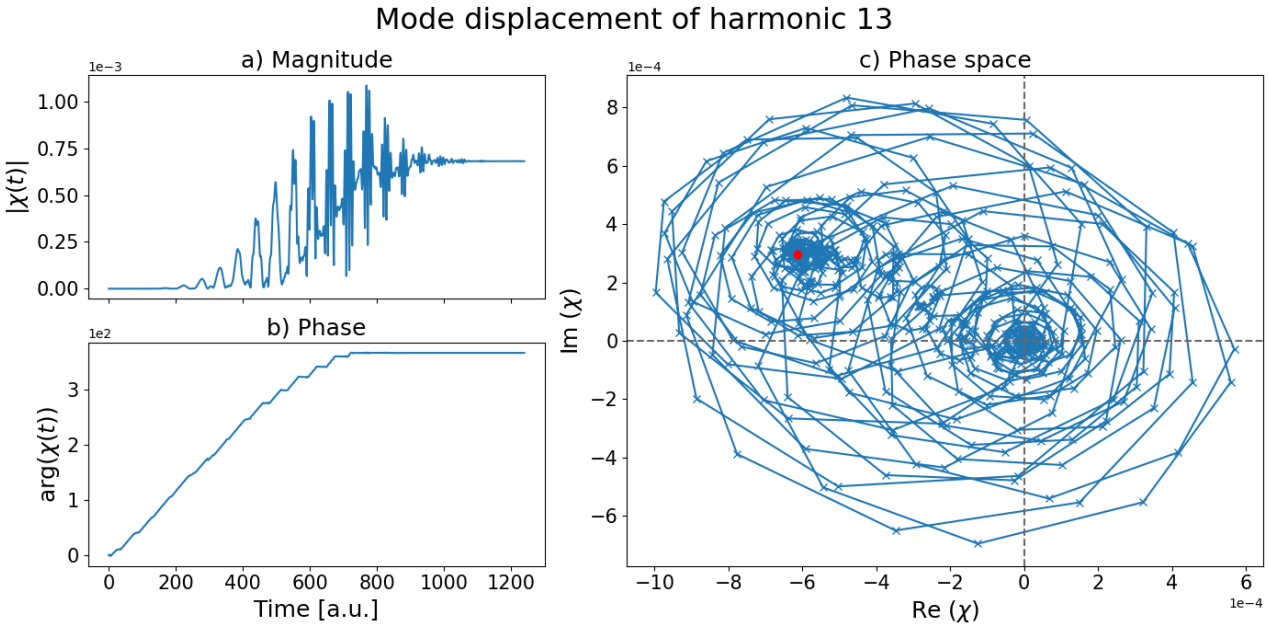

Figure C.7: a) Plot of displacement 13's magnitude as a function of time. b) Plot of displacement 13's phase as a function of time. c) Plot of displacement 13's time evolution in the optical phase space. The final displacement is marked with a red dot.

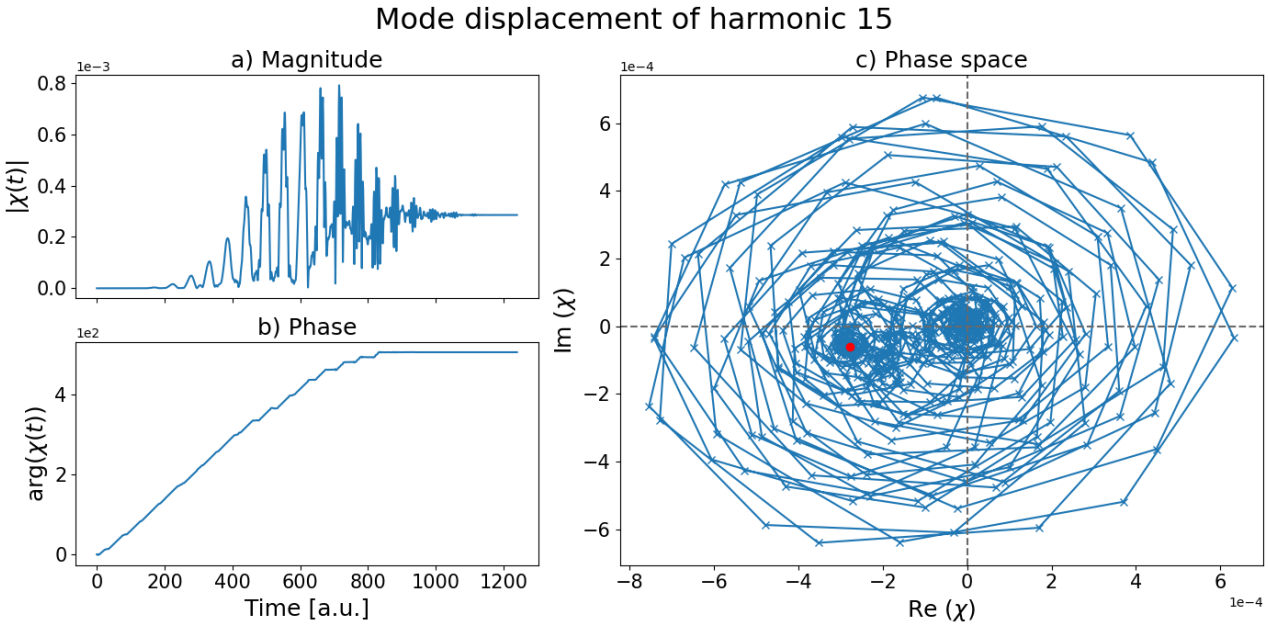

Figure C.8: a) Plot of displacement 15's magnitude as a function of time. b) Plot of displacement 15's phase as a function of time. c) Plot of displacement 15's time evolution in the optical phase space. The final displacement is marked with a red dot.

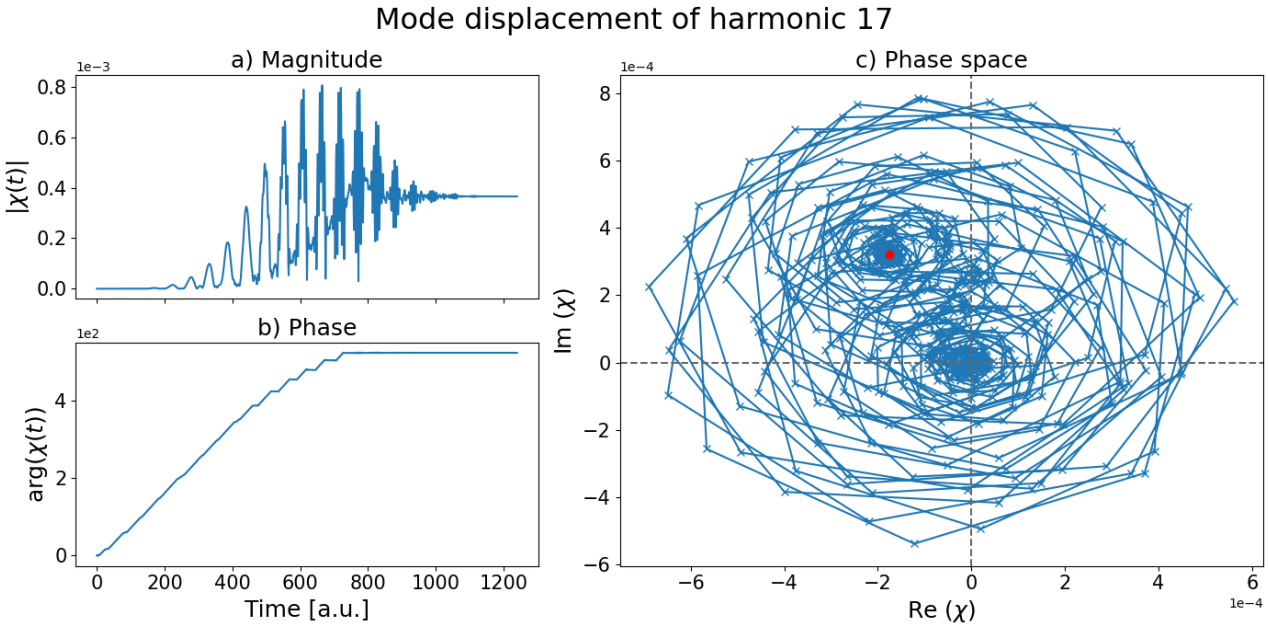

Figure C.9: a) Plot of displacement 17's magnitude as a function of time. b) Plot of displacement 17's phase as a function of time. c) Plot of displacement 17's time evolution in the optical phase space. The final displacement is marked with a red dot.

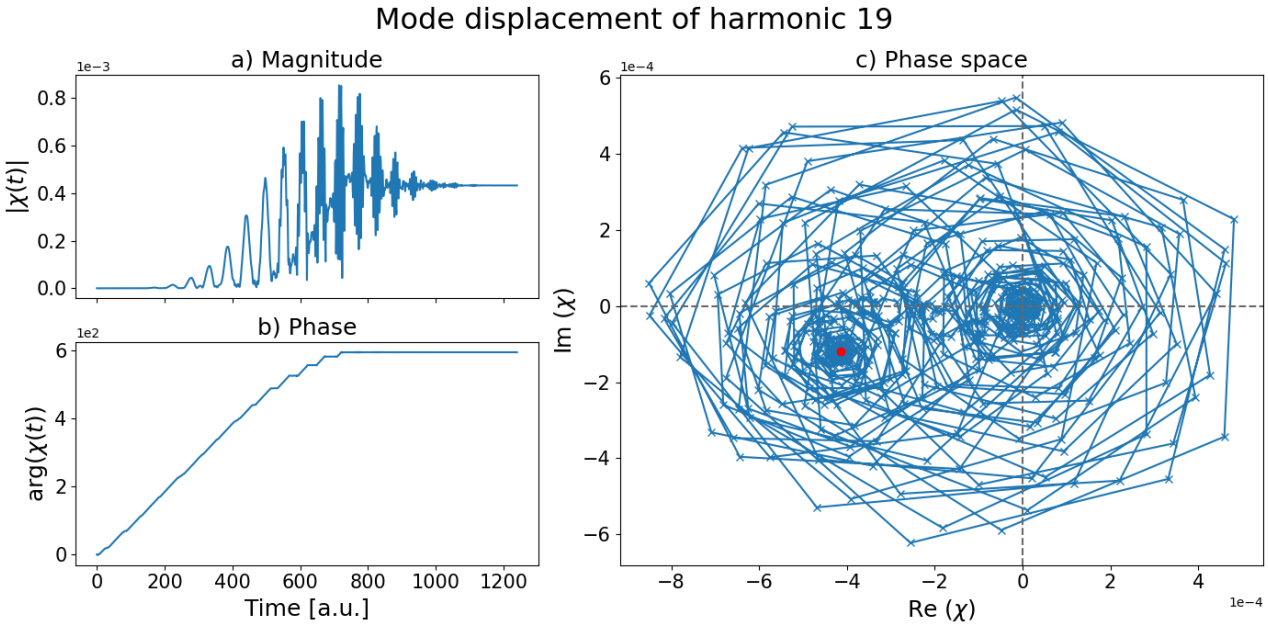

Figure C.10: a) Plot of displacement 19's magnitude as a function of time. b) Plot of displacement 19's phase as a function of time. c) Plot of displacement 19's time evolution in the optical phase space. The final displacement is marked with a red dot.

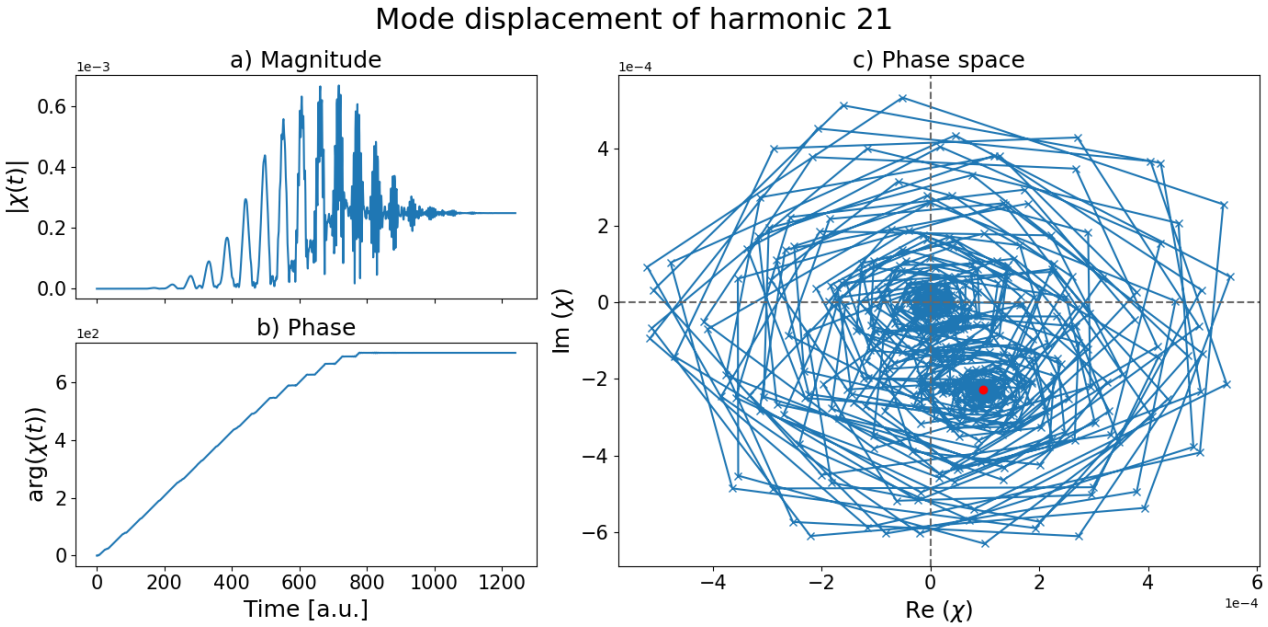

Figure C.11: a) Plot of displacement 21's magnitude as a function of time. b) Plot of displacement 21's phase as a function of time. c) Plot of displacement 21's time evolution in the optical phase space. The final displacement is marked with a red dot.

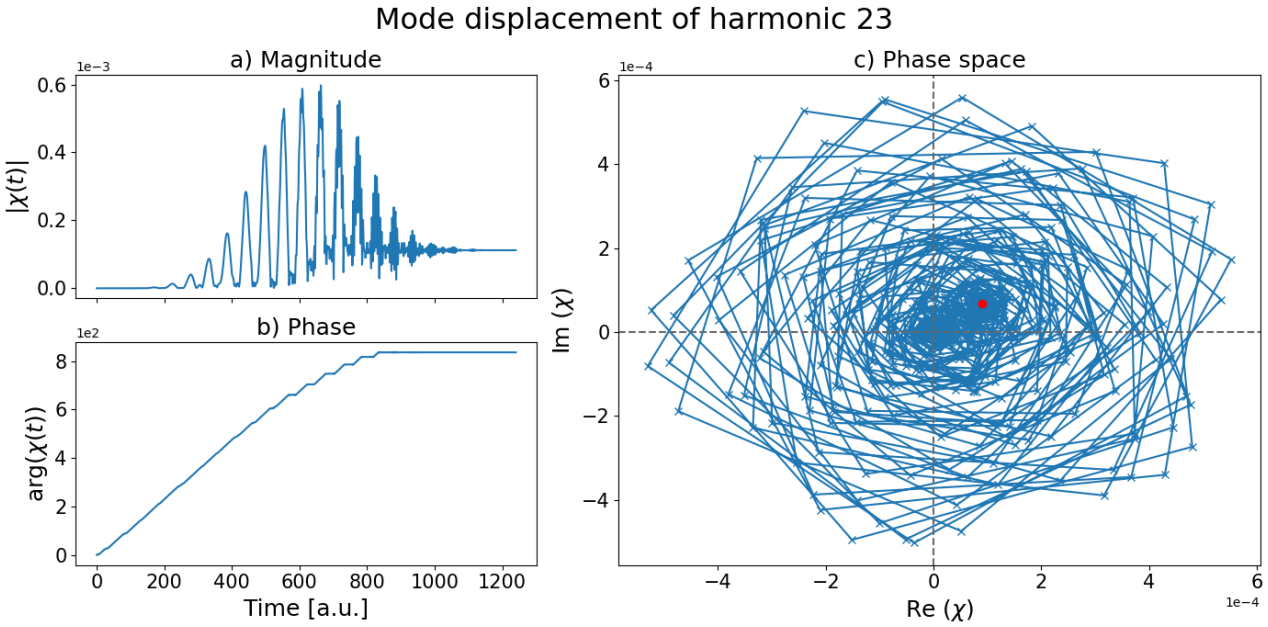

Figure C.12: a) Plot of displacement 23's magnitude as a function of time. b) Plot of displacement 23's phase as a function of time. c) Plot of displacement 23's time evolution in the optical phase space. The final displacement is marked with a red dot.

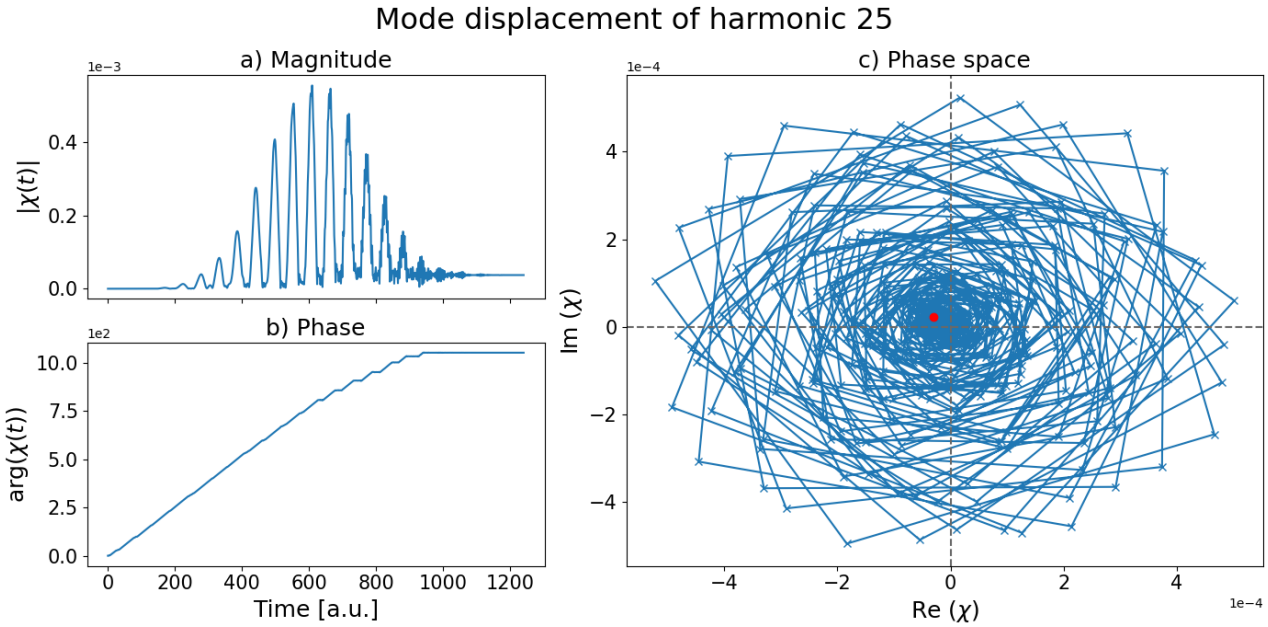

Figure C.13: a) Plot of displacement 25's magnitude as a function of time. b) Plot of displacement 25's phase as a function of time. c) Plot of displacement 25's time evolution in the optical phase space. The final displacement is marked with a red dot.

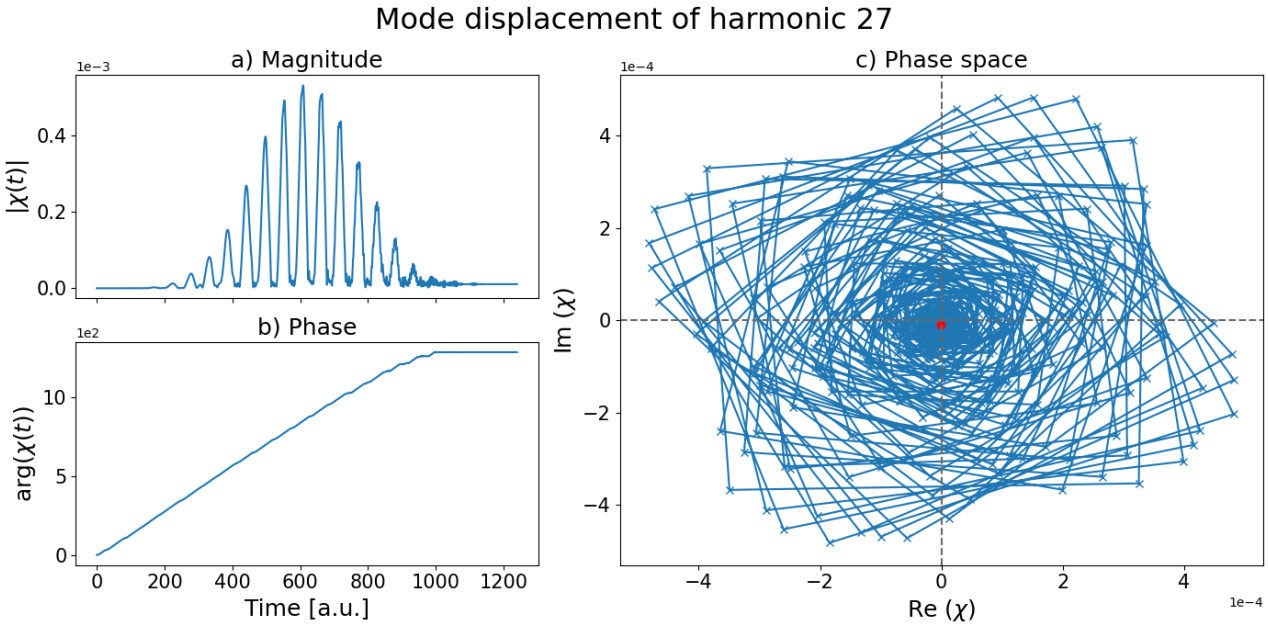

Figure C.14: a) Plot of displacement 27's magnitude as a function of time. b) Plot of displacement 27's phase as a function of time. c) Plot of displacement 27's time evolution in the optical phase space. The final displacement is marked with a red dot.

C.1.2 Density Matrices

The density matrices for harmonics 7 to 27 are shown. The phase matrices only show values corresponding to magnitudes greater than 1×10^{-55} to avoid computational errors.

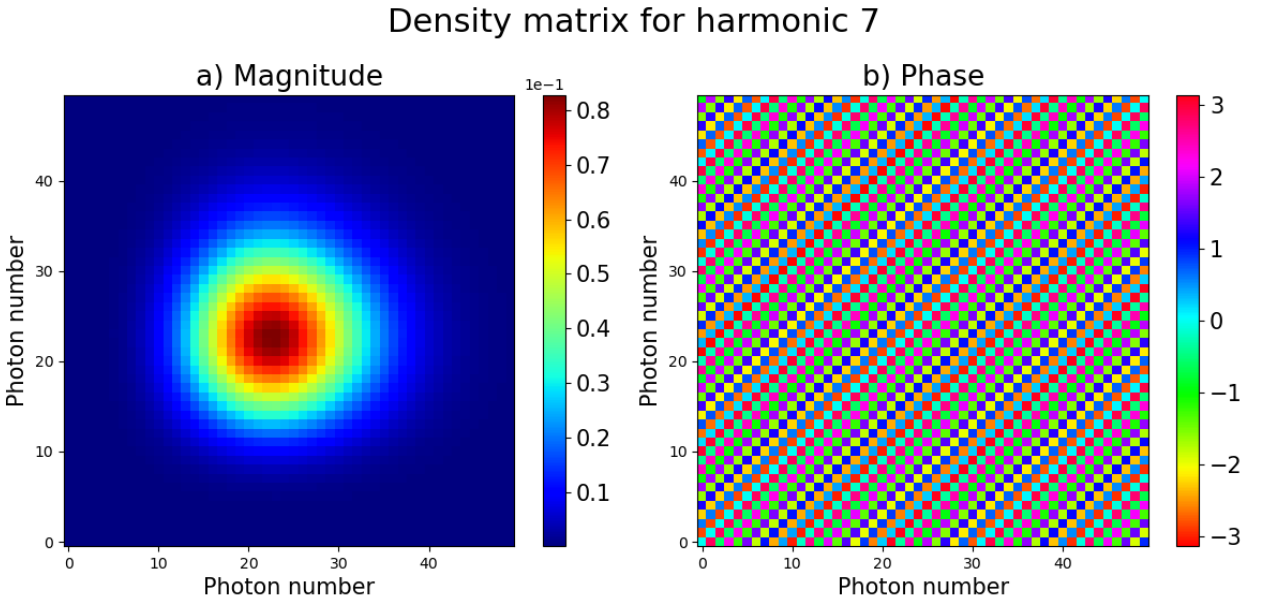

Figure C.15: a) Plot of the density matrix magnitudes. b) Plot of the density matrix phases.

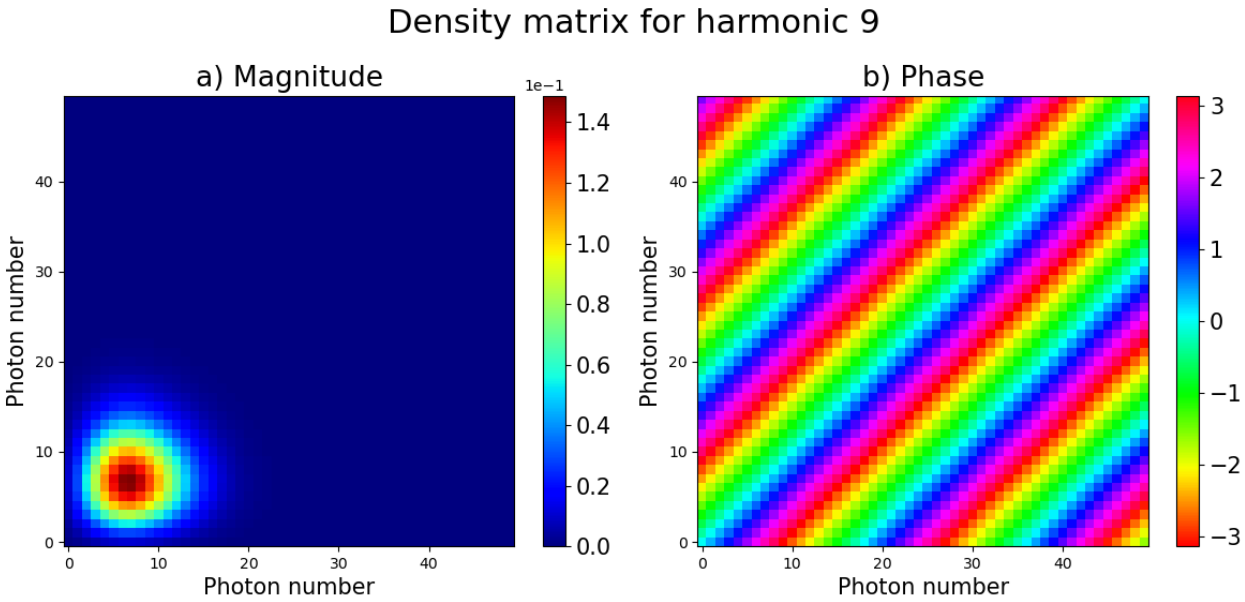

Figure C.16: a) Plot of the density matrix magnitudes. b) Plot of the density matrix phases.

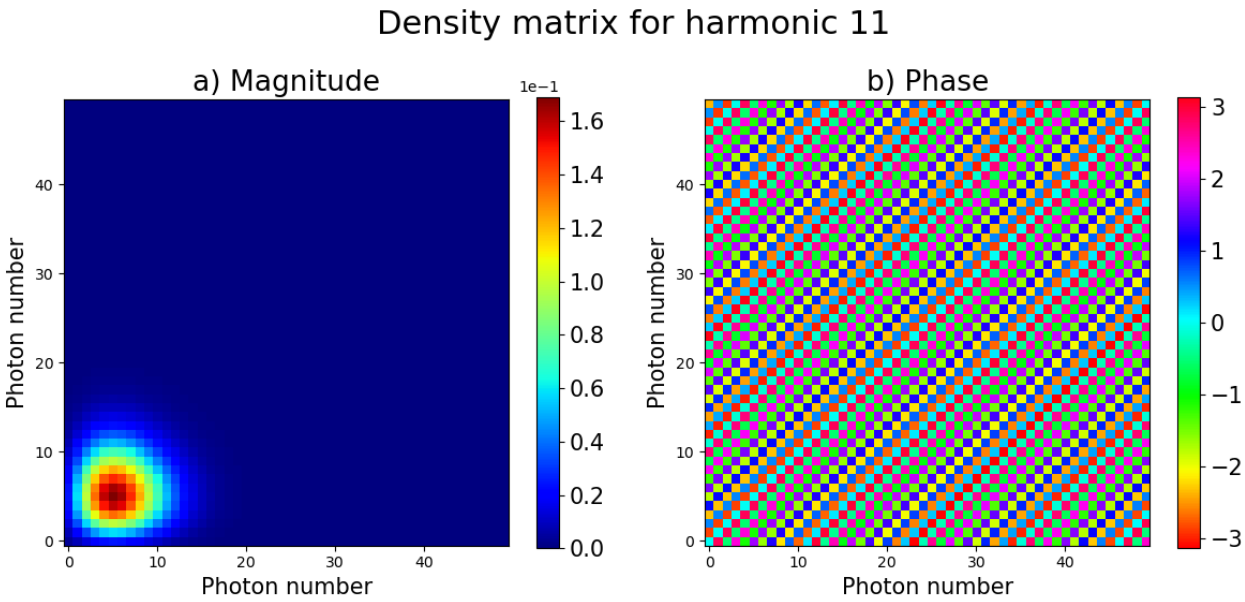

Figure C.17: a) Plot of the density matrix magnitudes. b) Plot of the density matrix phases.

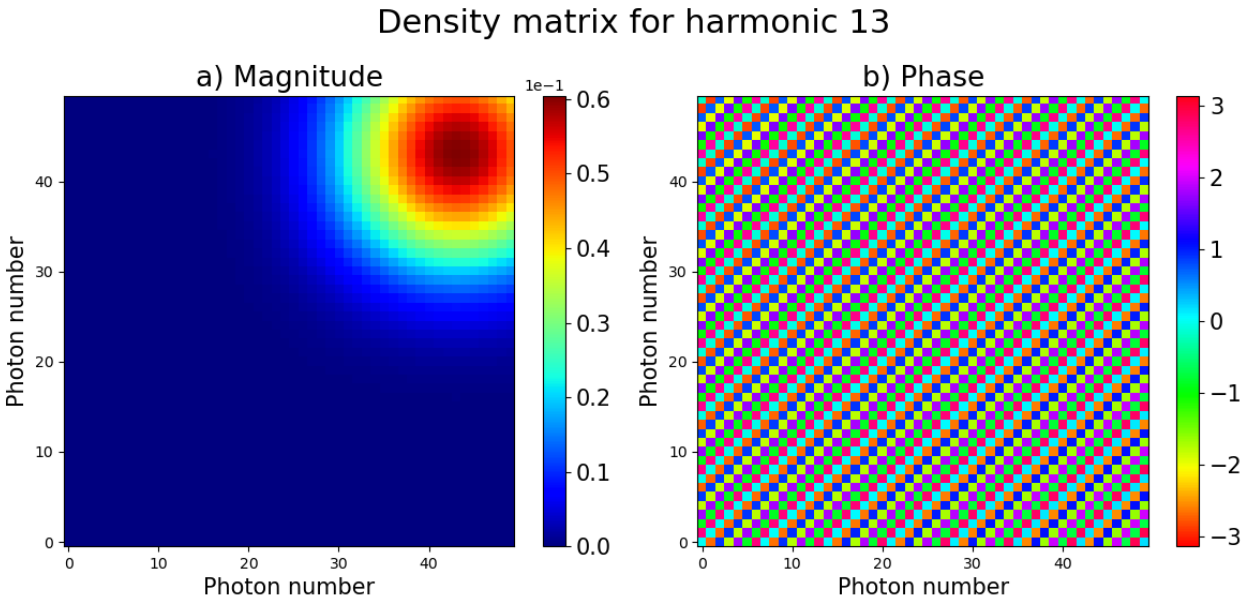

Figure C.18: a) Plot of the density matrix magnitudes. b) Plot of the density matrix phases.

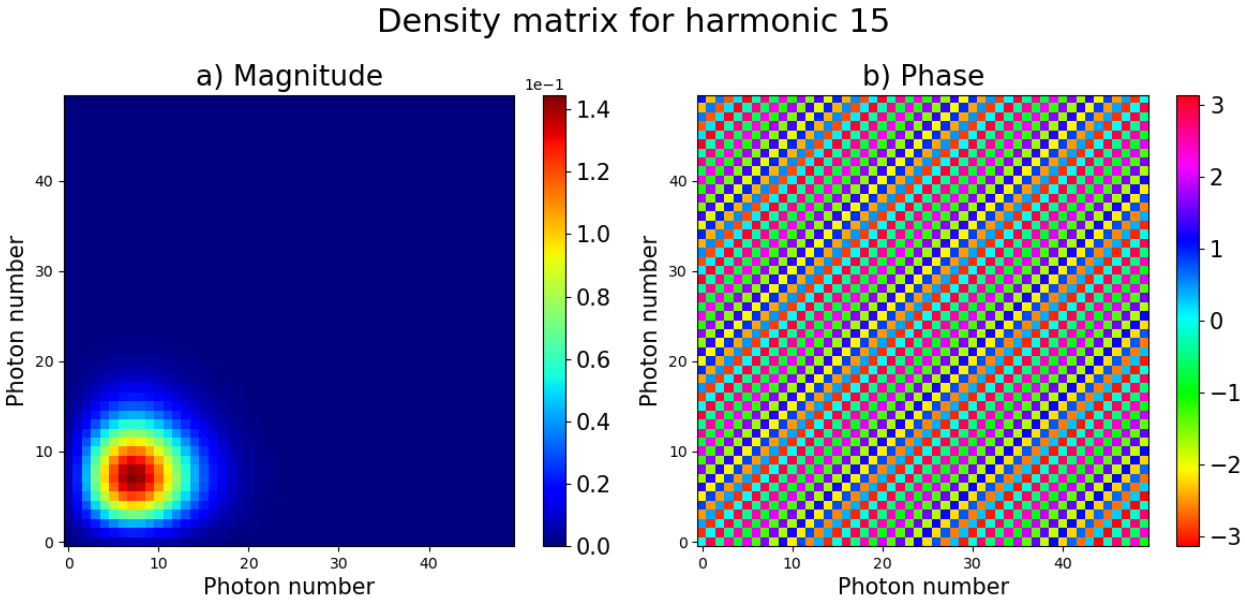

Figure C.19: a) Plot of the density matrix magnitudes. b) Plot of the density matrix phases.

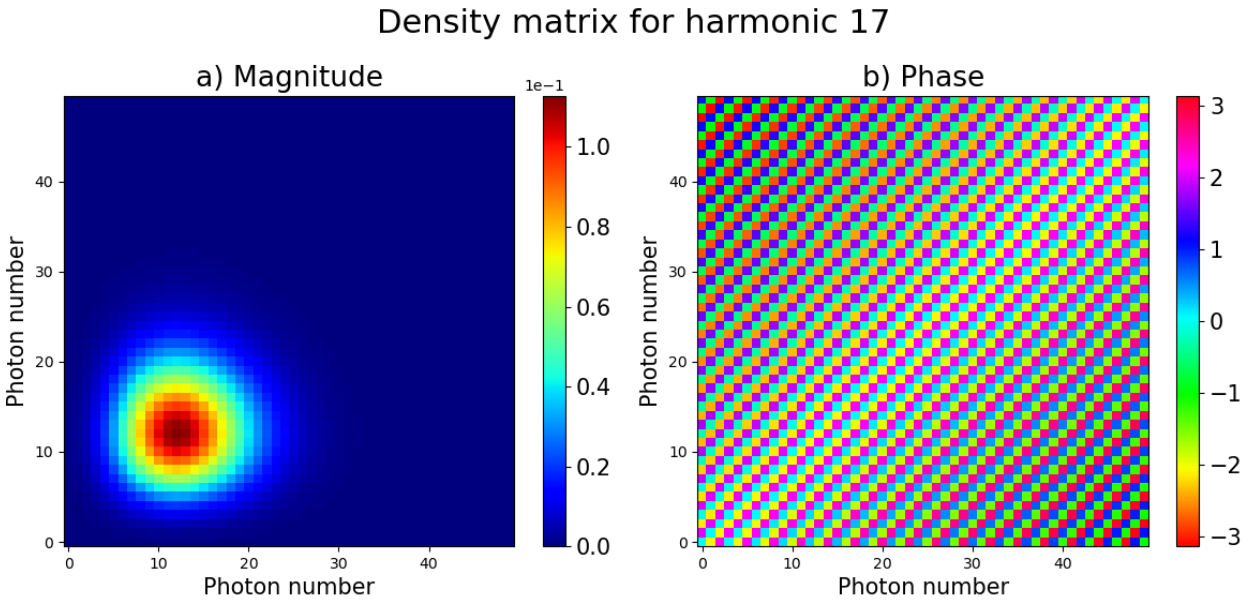

Figure C.20: a) Plot of the density matrix magnitudes. b) Plot of the density matrix phases.

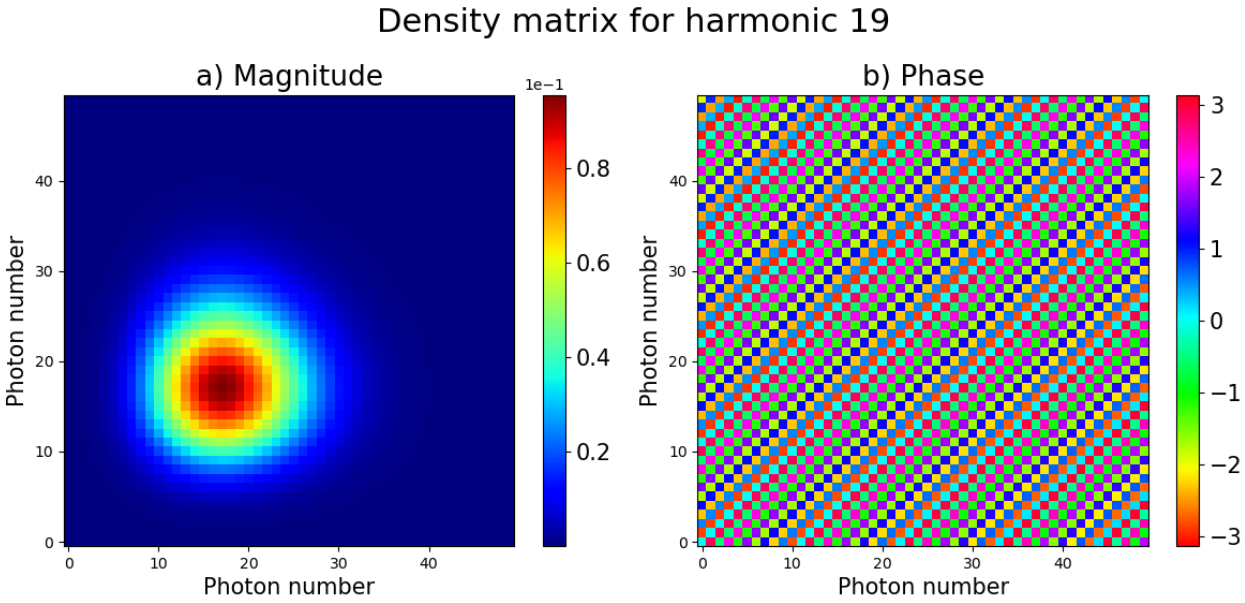

Figure C.21: a) Plot of the density matrix magnitudes. b) Plot of the density matrix phases.

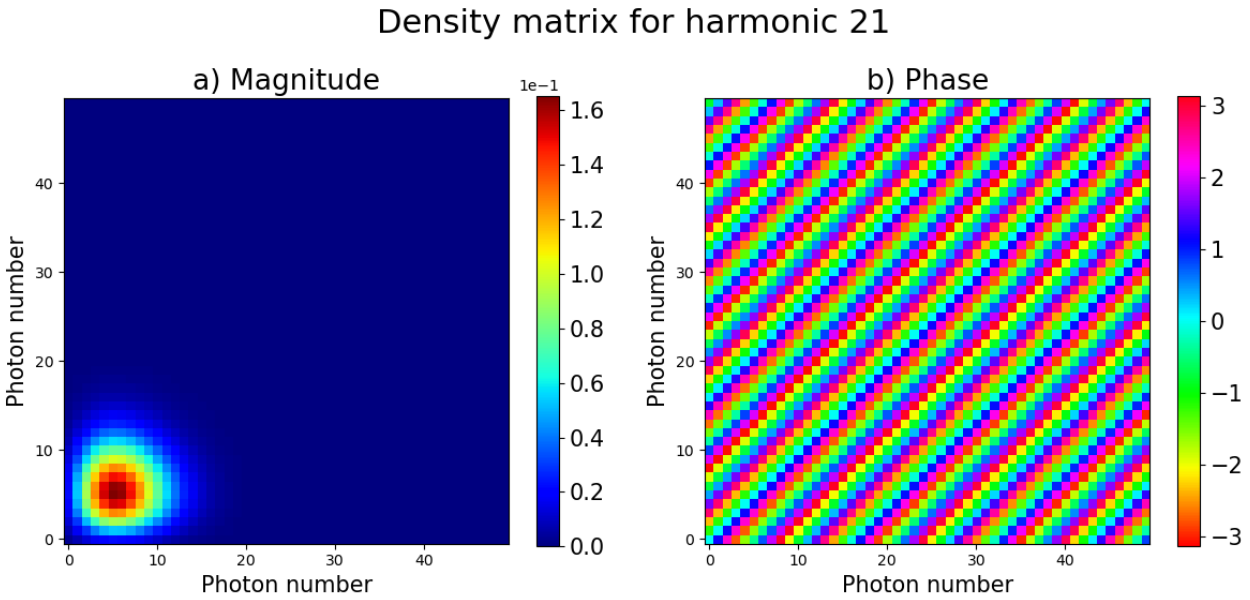

Figure C.22: a) Plot of the density matrix magnitudes. b) Plot of the density matrix phases.

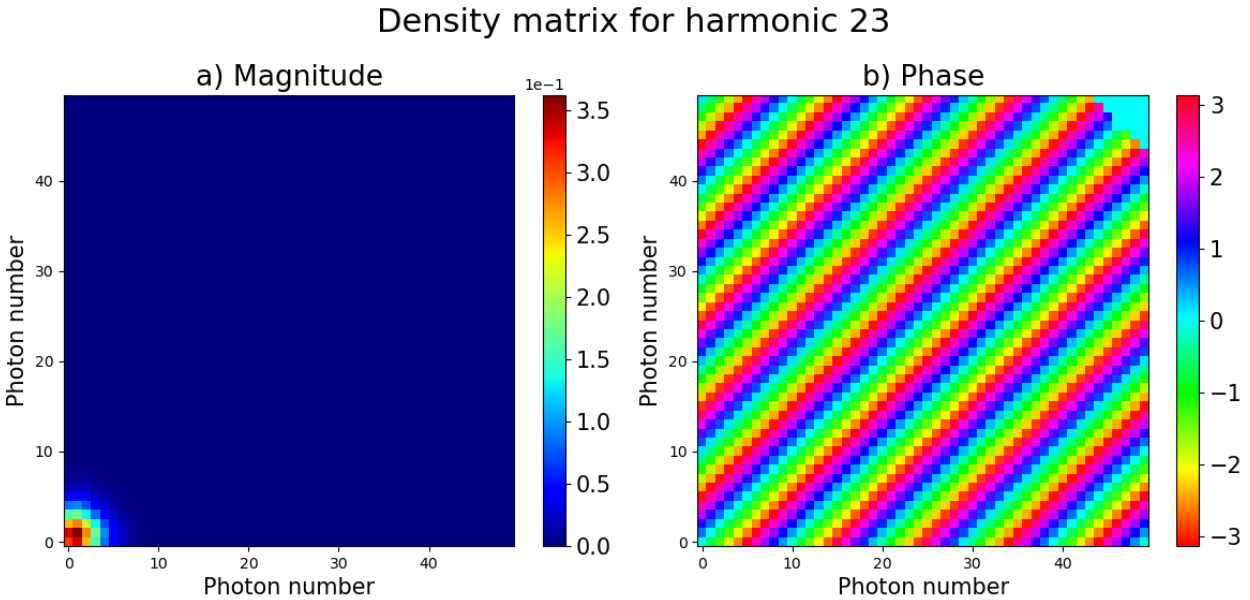

Figure C.23: a) Plot of the density matrix magnitudes. b) Plot of the density matrix phases.

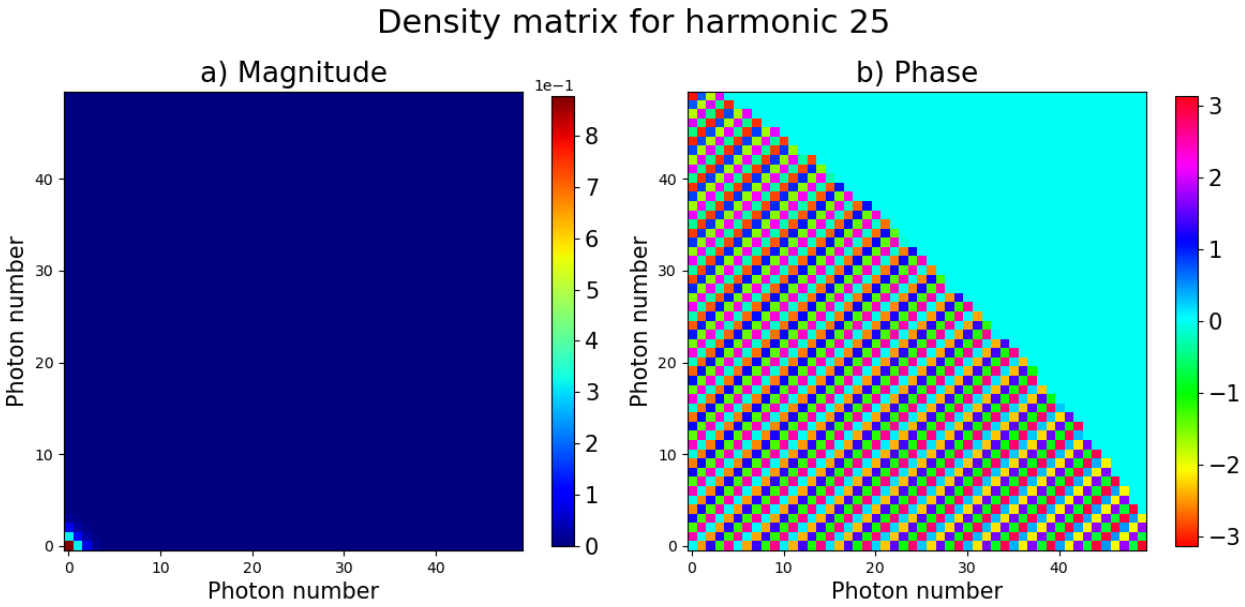

Figure C.24: a) Plot of the density matrix magnitudes. b) Plot of the density matrix phases.

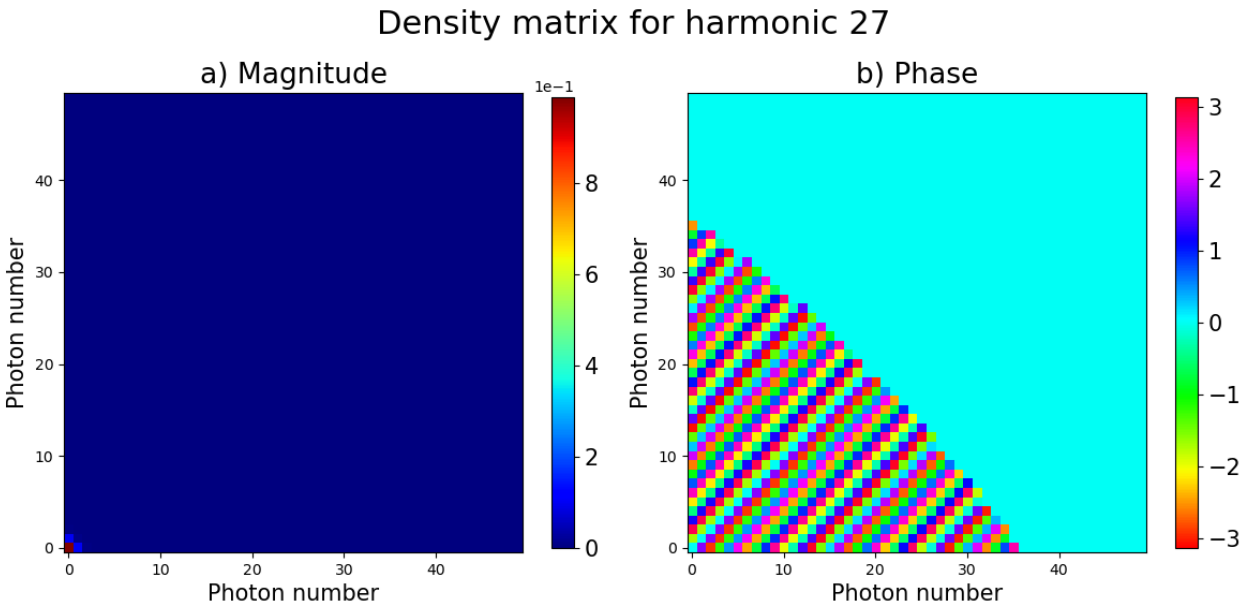

Figure C.25: a) Plot of the density matrix magnitudes. b) Plot of the density matrix phases.

C.2 Few atoms

C.2.1 Mode Displacements

In this appendix, figures showing the time evolution of displacements 1 to 27 are included.

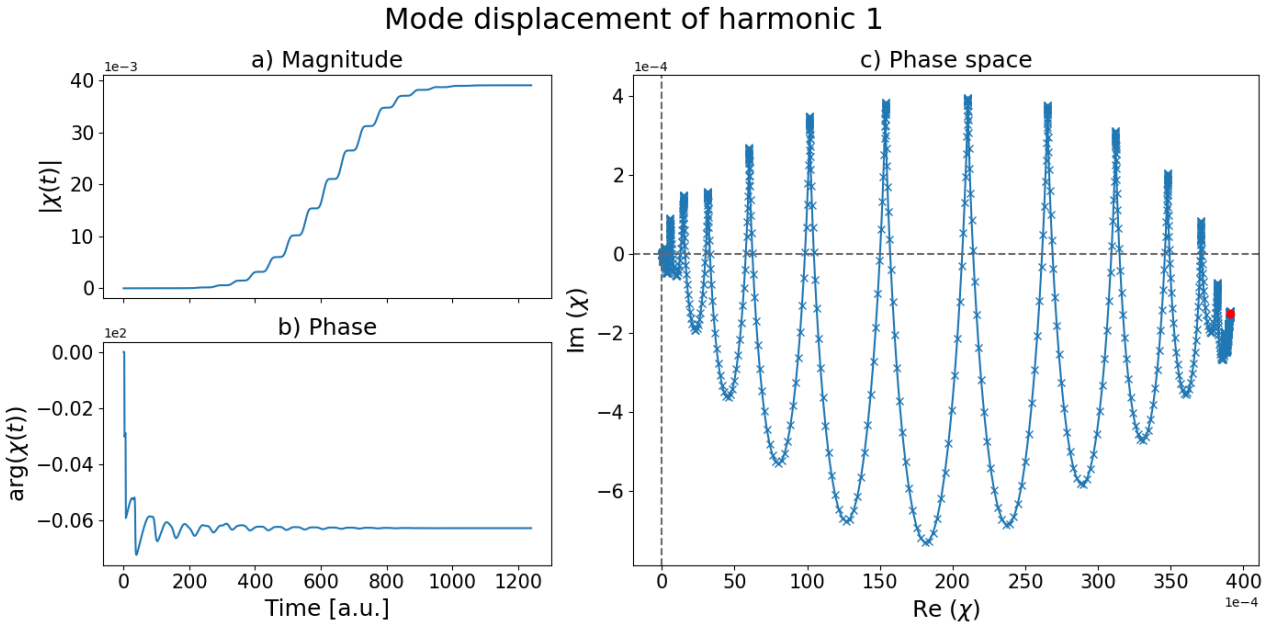

Figure C.26: a) Plot of displacement 1's magnitude as a function of time. b) Plot of displacement 1's phase as a function of time. c) Plot of displacement 1's time evolution in the optical phase space. The final displacement is marked with a red dot.

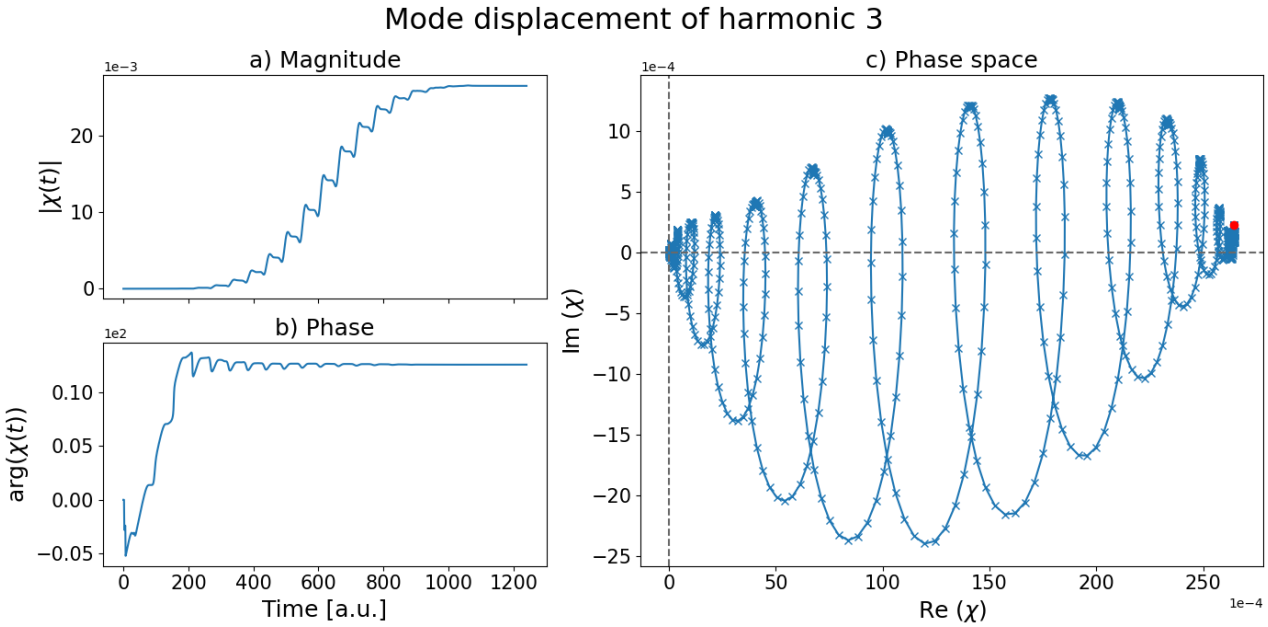

Figure C.27: a) Plot of displacement 3's magnitude as a function of time. b) Plot of displacement 3's phase as a function of time. c) Plot of displacement 3's time evolution in the optical phase space. The final displacement is marked with a red dot.

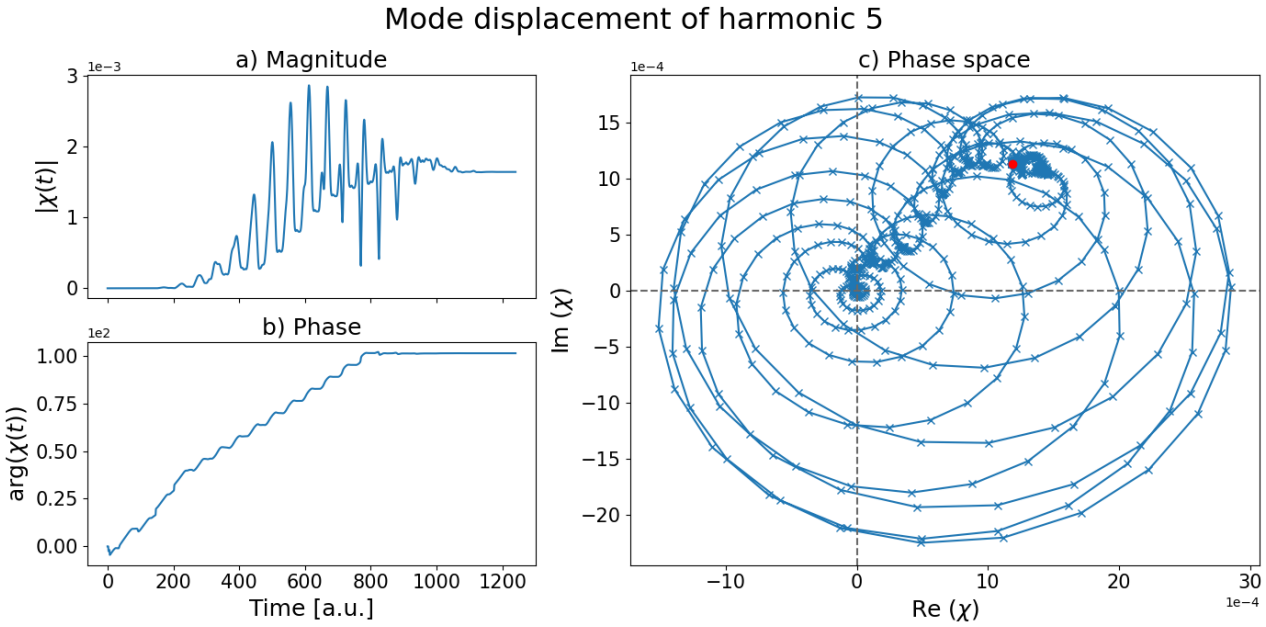

Figure C.28: a) Plot of displacement 5's magnitude as a function of time. b) Plot of displacement 5's phase as a function of time. c) Plot of displacement 5's time evolution in the optical phase space. The final displacement is marked with a red dot.

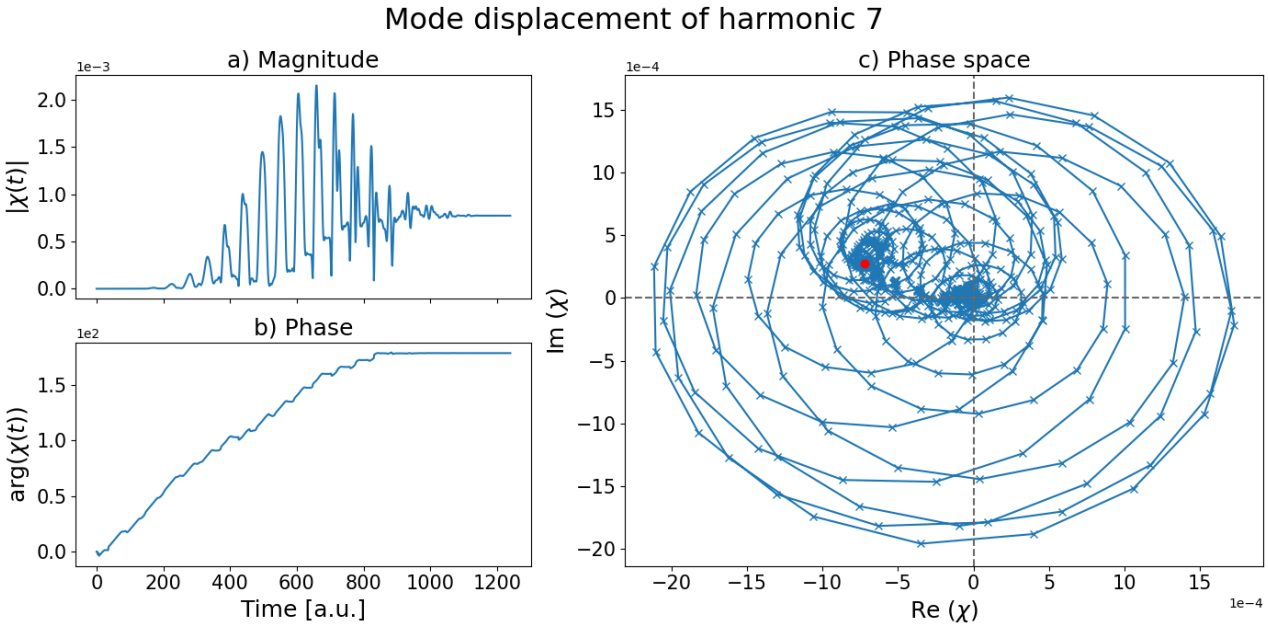

Figure C.29: a) Plot of displacement 7's magnitude as a function of time. b) Plot of displacement 7's phase as a function of time. c) Plot of displacement 7's time evolution in the optical phase space. The final displacement is marked with a red dot.

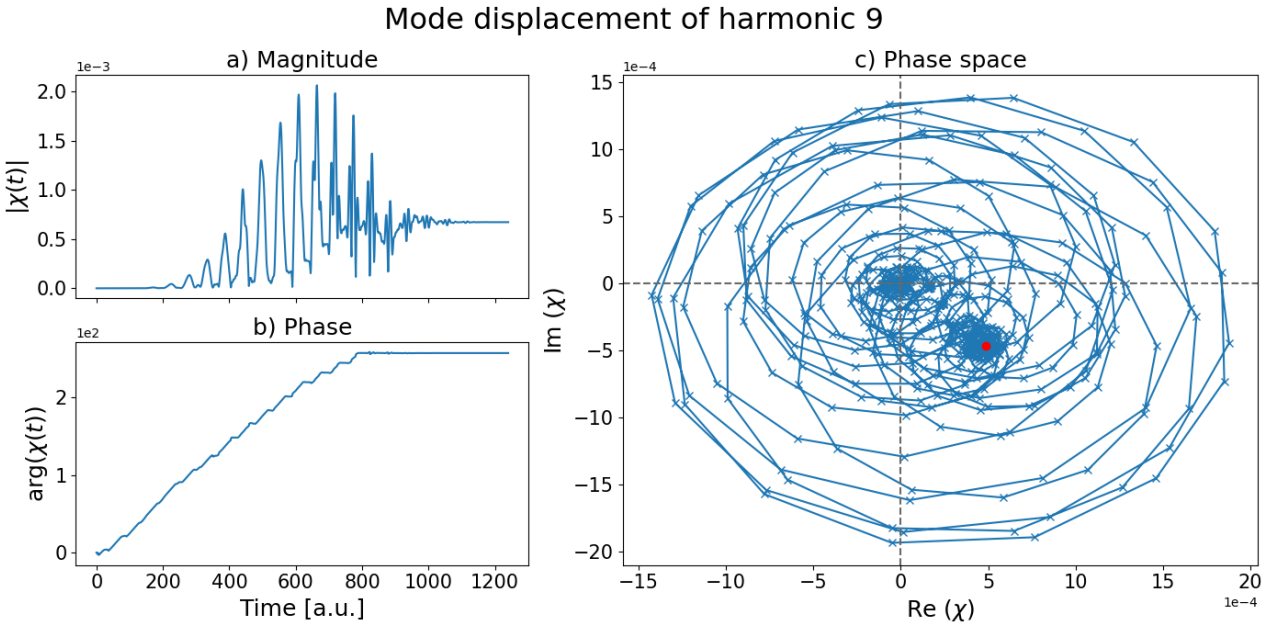

Figure C.30: a) Plot of displacement 9's magnitude as a function of time. b) Plot of displacement 9's phase as a function of time. c) Plot of displacement 9's time evolution in the optical phase space. The final displacement is marked with a red dot.

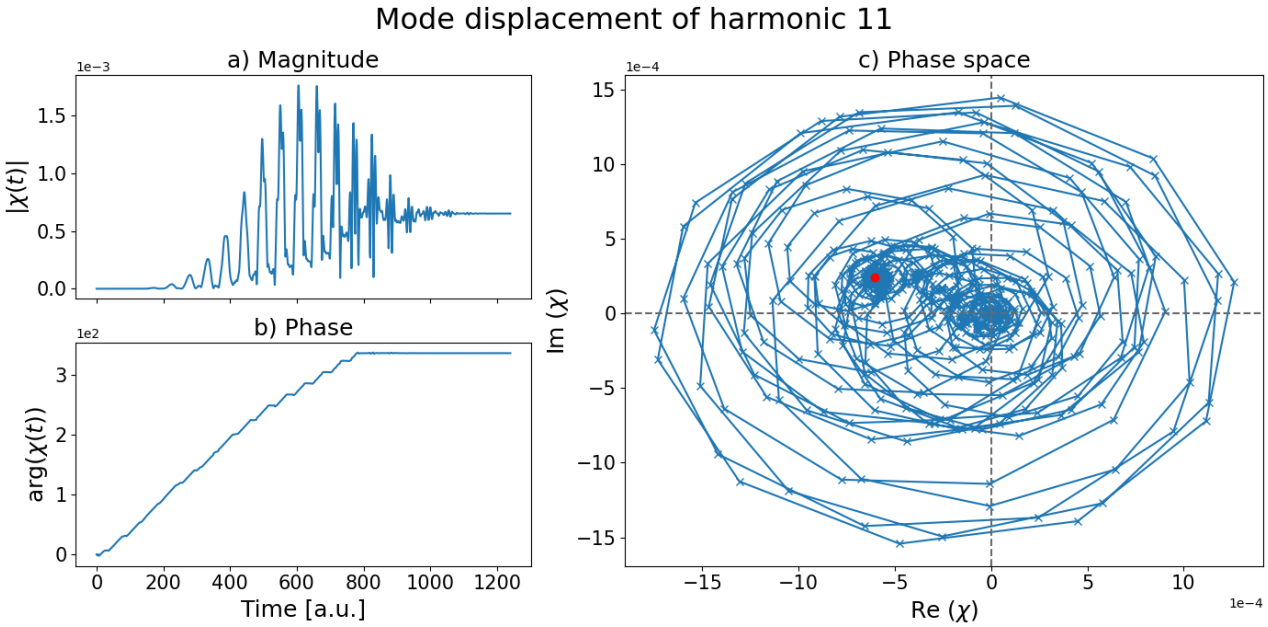

Figure C.31: a) Plot of displacement 11's magnitude as a function of time. b) Plot of displacement 11's phase as a function of time. c) Plot of displacement 11's time evolution in the optical phase space. The final displacement is marked with a red dot.

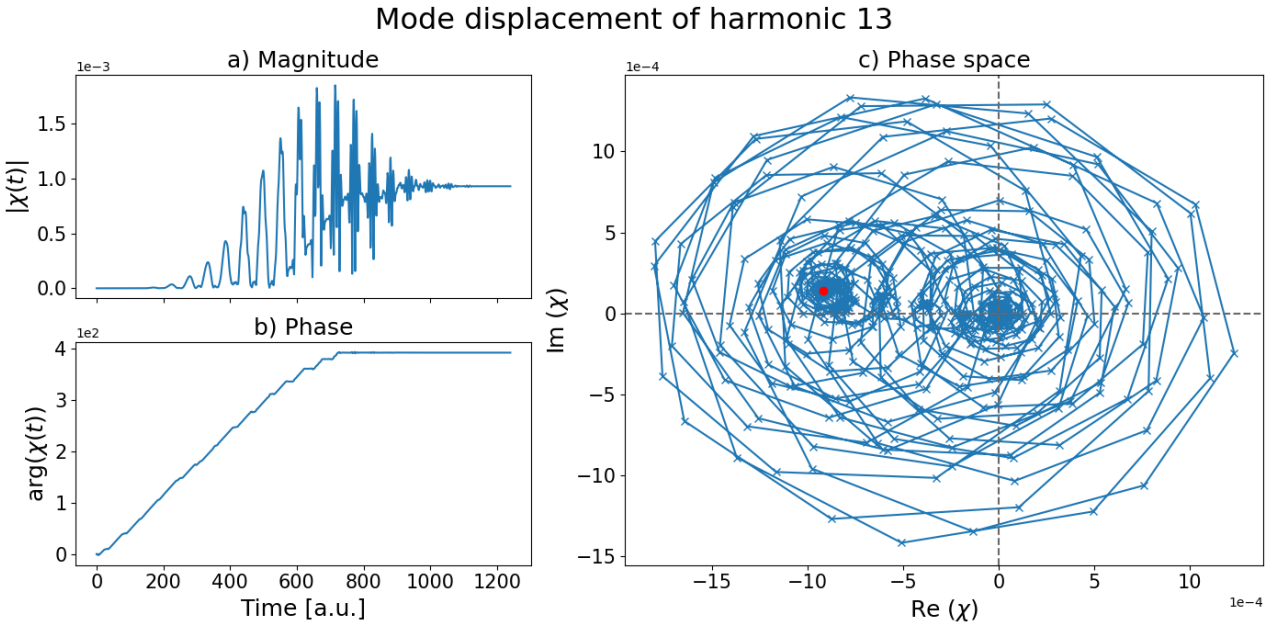

Figure C.32: a) Plot of displacement 13's magnitude as a function of time. b) Plot of displacement 13's phase as a function of time. c) Plot of displacement 13's time evolution in the optical phase space. The final displacement is marked with a red dot.

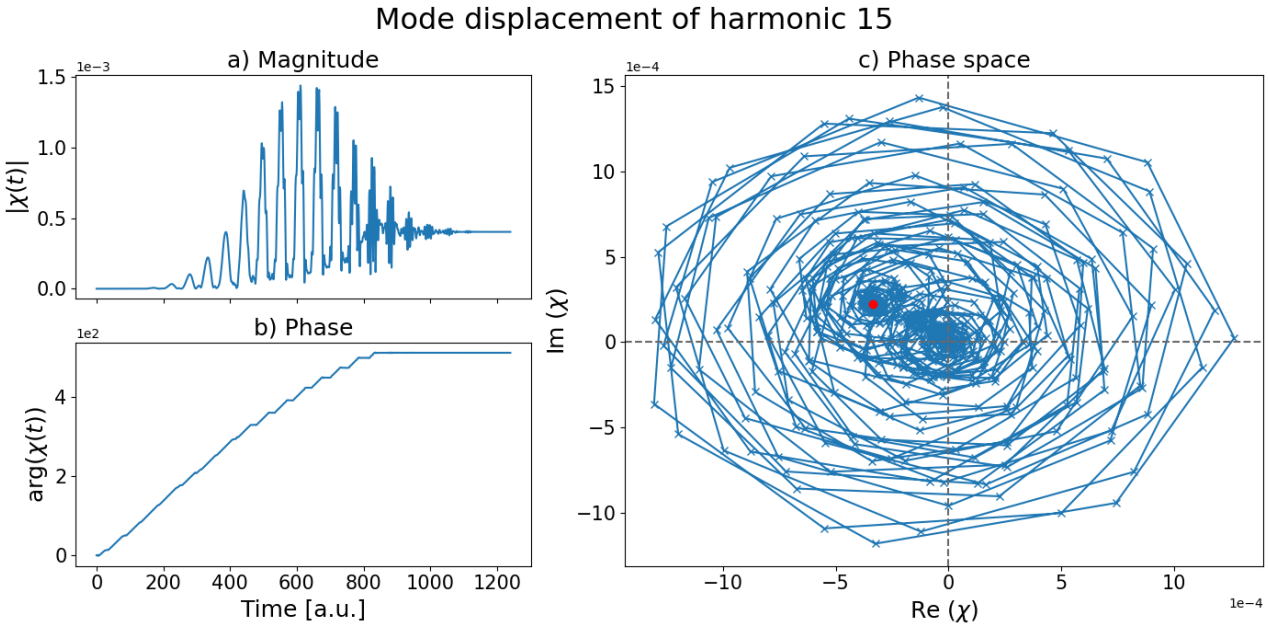

Figure C.33: a) Plot of displacement 15's magnitude as a function of time. b) Plot of displacement 15's phase as a function of time. c) Plot of displacement 15's time evolution in the optical phase space. The final displacement is marked with a red dot.

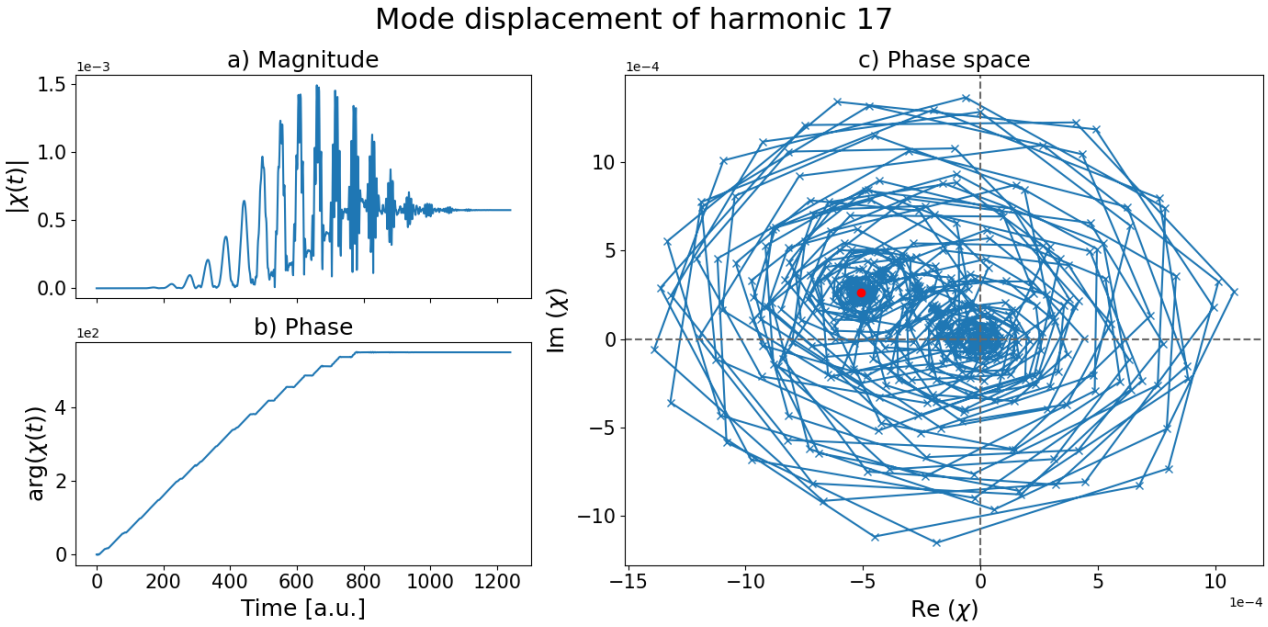

Figure C.34: a) Plot of displacement 17's magnitude as a function of time. b) Plot of displacement 17's phase as a function of time. c) Plot of displacement 17's time evolution in the optical phase space. The final displacement is marked with a red dot.

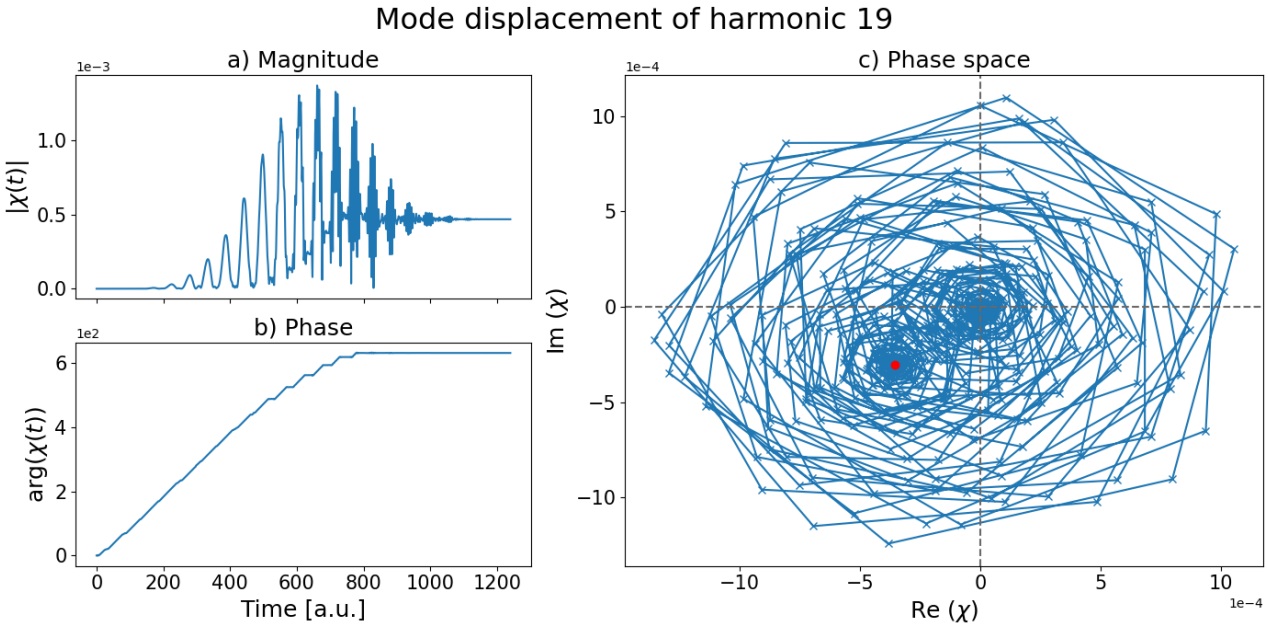

Figure C.35: a) Plot of displacement 19's magnitude as a function of time. b) Plot of displacement 19's phase as a function of time. c) Plot of displacement 19's time evolution in the optical phase space. The final displacement is marked with a red dot.

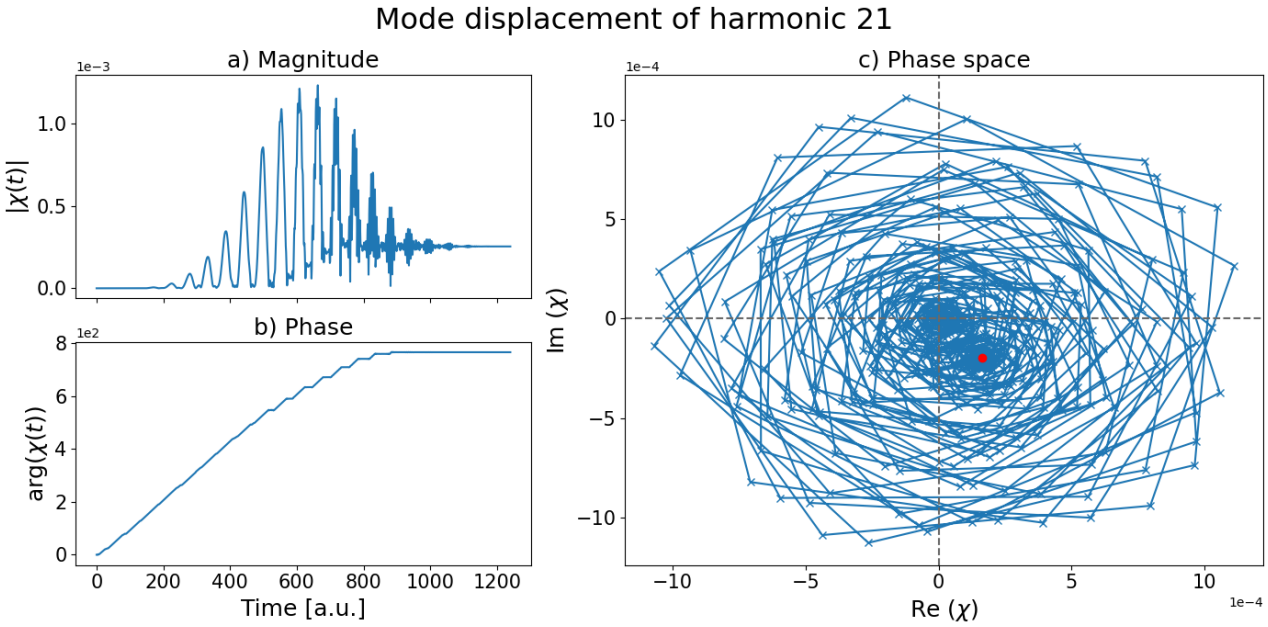

Figure C.36: a) Plot of displacement 21's magnitude as a function of time. b) Plot of displacement 21's phase as a function of time. c) Plot of displacement 21's time evolution in the optical phase space. The final displacement is marked with a red dot.

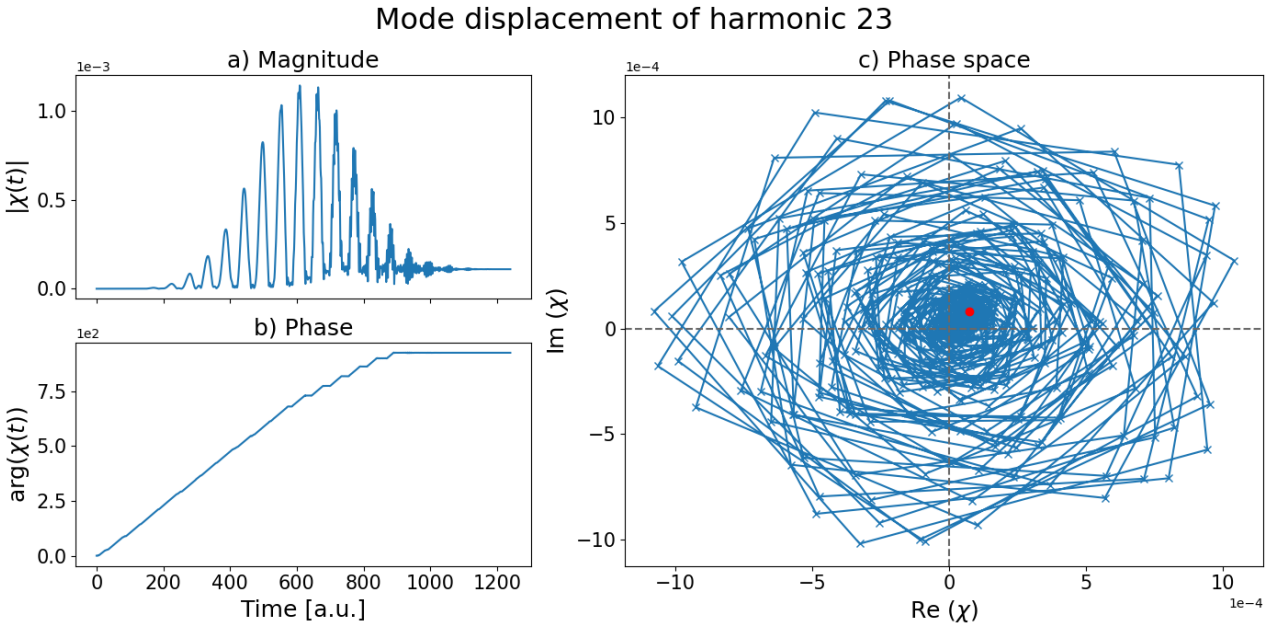

Figure C.37: a) Plot of displacement 23's magnitude as a function of time. b) Plot of displacement 23's phase as a function of time. c) Plot of displacement 23's time evolution in the optical phase space. The final displacement is marked with a red dot.

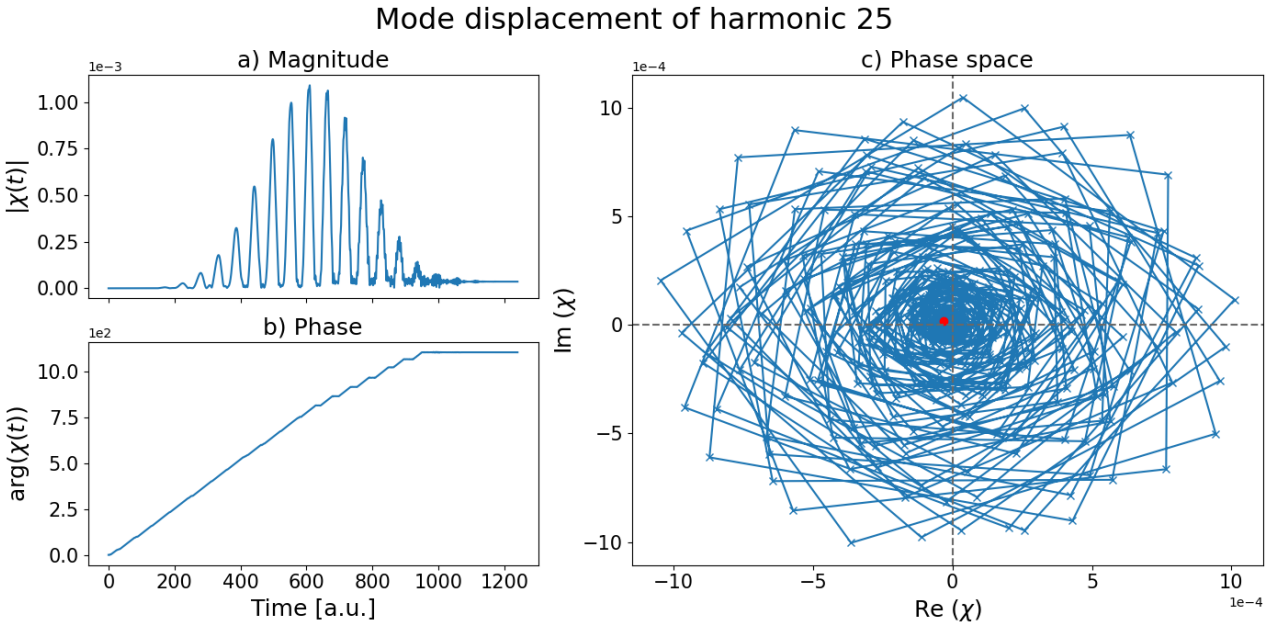

Figure C.38: a) Plot of displacement 25's magnitude as a function of time. b) Plot of displacement 25's phase as a function of time. c) Plot of displacement 25's time evolution in the optical phase space. The final displacement is marked with a red dot.

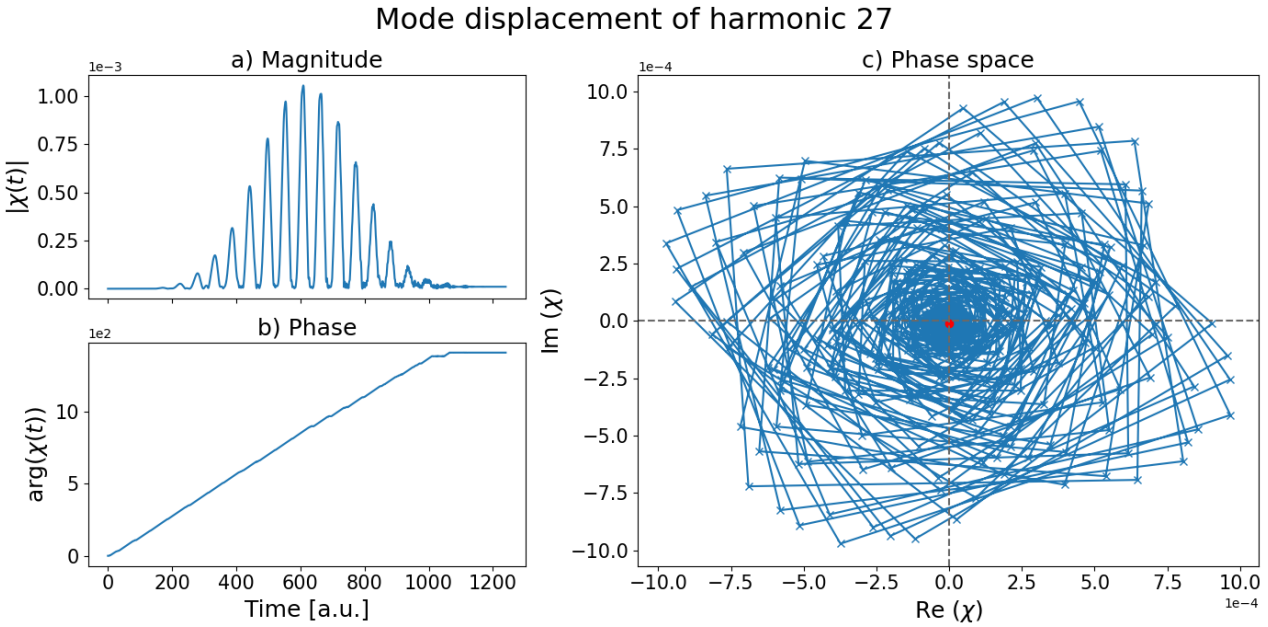

Figure C.39: a) Plot of displacement 27's magnitude as a function of time. b) Plot of displacement 27's phase as a function of time. c) Plot of displacement 27's time evolution in the optical phase space. The final displacement is marked with a red dot.

C.2.2 Density Matrices

The density matrices for harmonics 7 to 27 are shown. The phase matrices only show values corresponding to magnitudes greater than 1×10^{-55} to avoid computational errors.

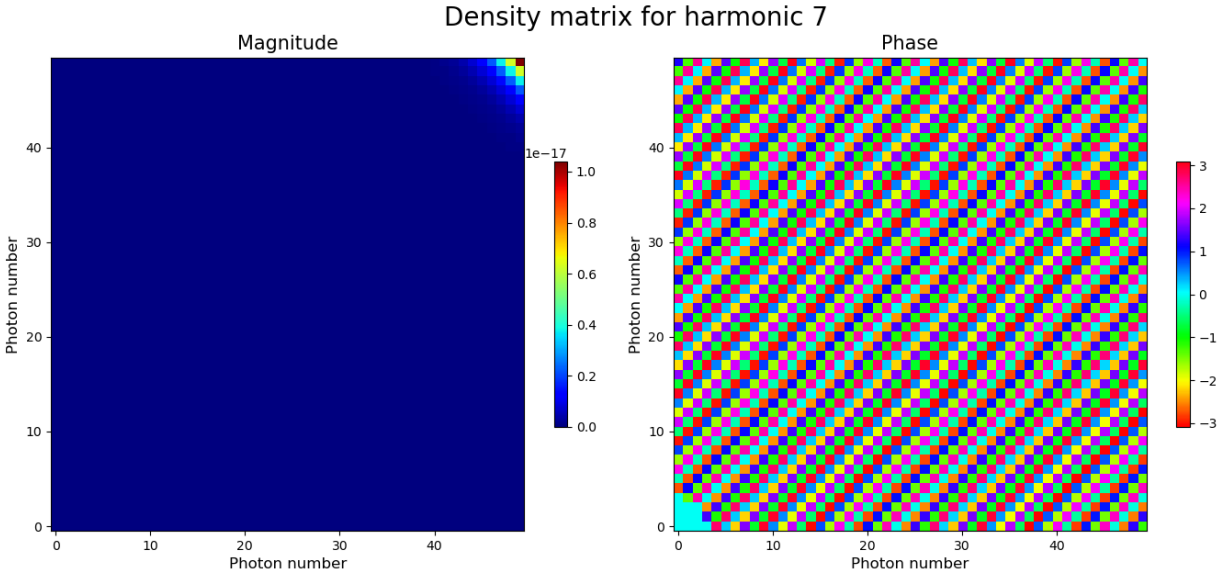

Figure C.40: a) Plot of the density matrix magnitudes. b) Plot of the density matrix phases.

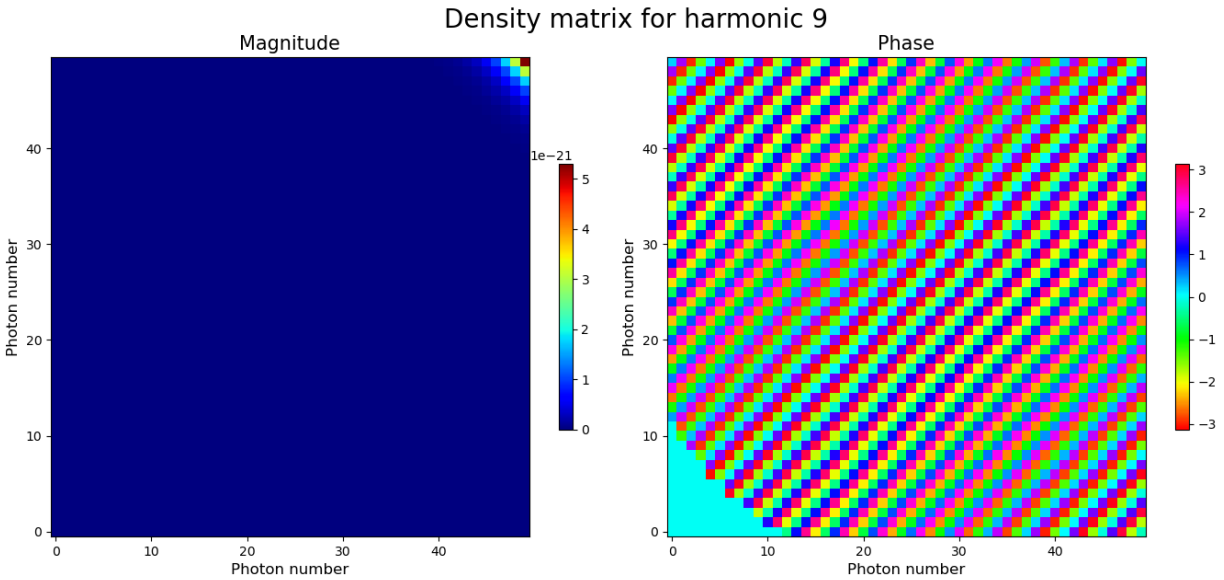

Figure C.41: a) Plot of the density matrix magnitudes. b) Plot of the density matrix phases.

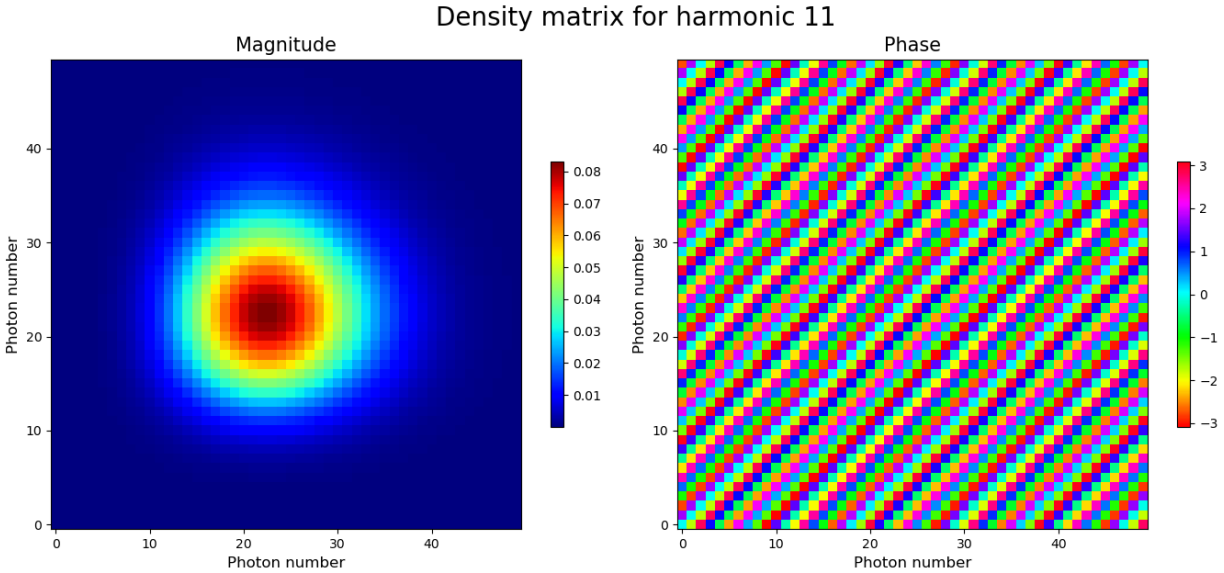

Figure C.42: a) Plot of the density matrix magnitudes. b) Plot of the density matrix phases.

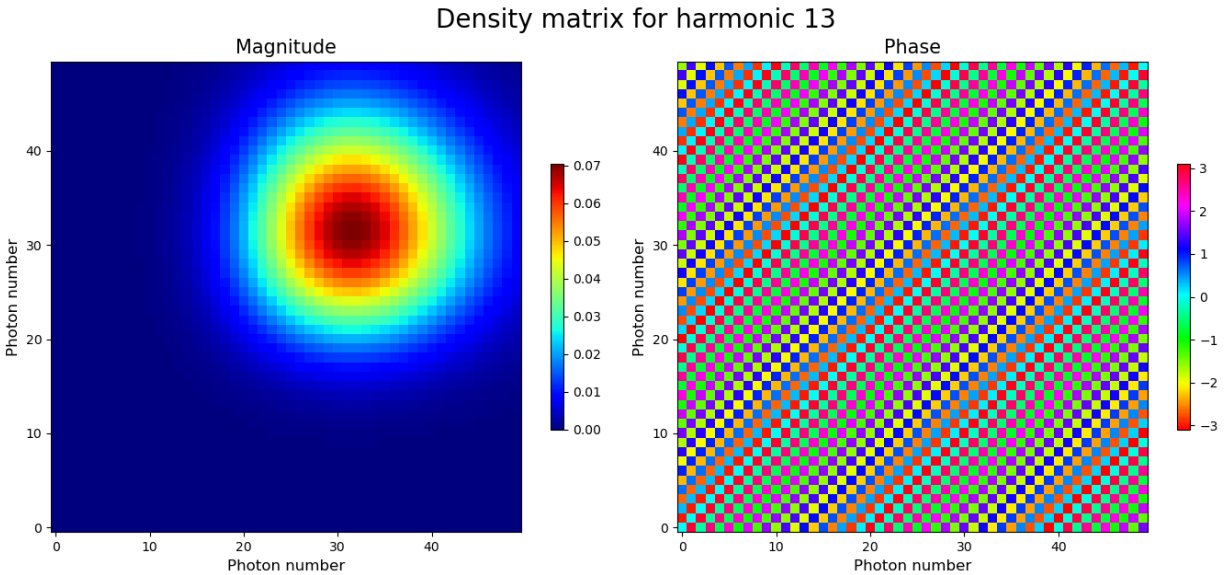

Figure C.43: a) Plot of the density matrix magnitudes. b) Plot of the density matrix phases.

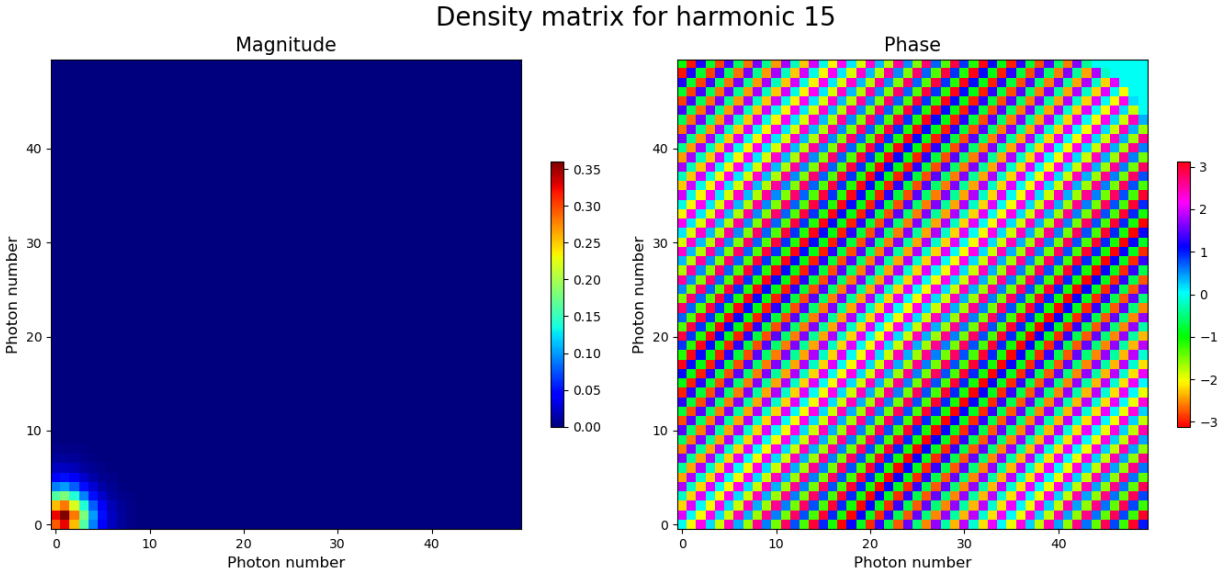

Figure C.44: a) Plot of the density matrix magnitudes. b) Plot of the density matrix phases.

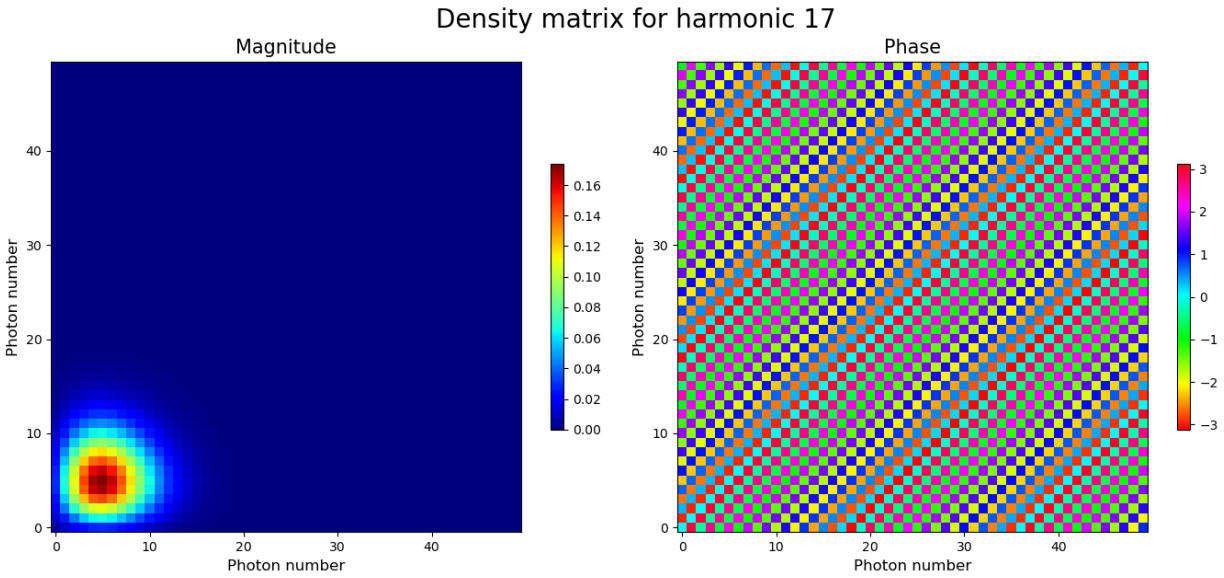

Figure C.45: a) Plot of the density matrix magnitudes. b) Plot of the density matrix phases.

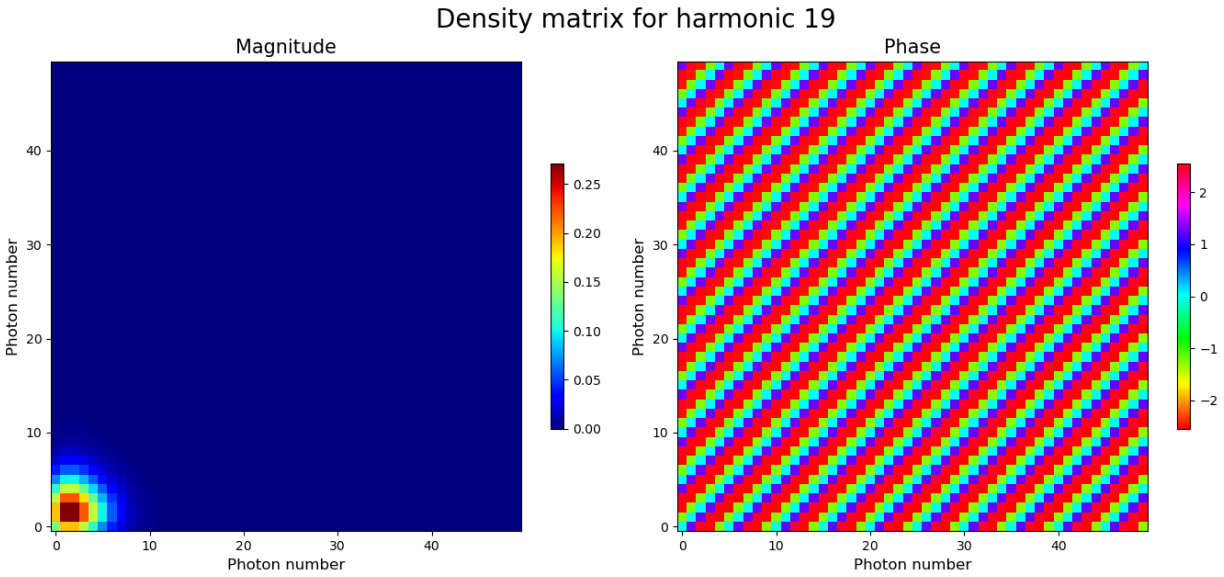

Figure C.46: a) Plot of the density matrix magnitudes. b) Plot of the density matrix phases.

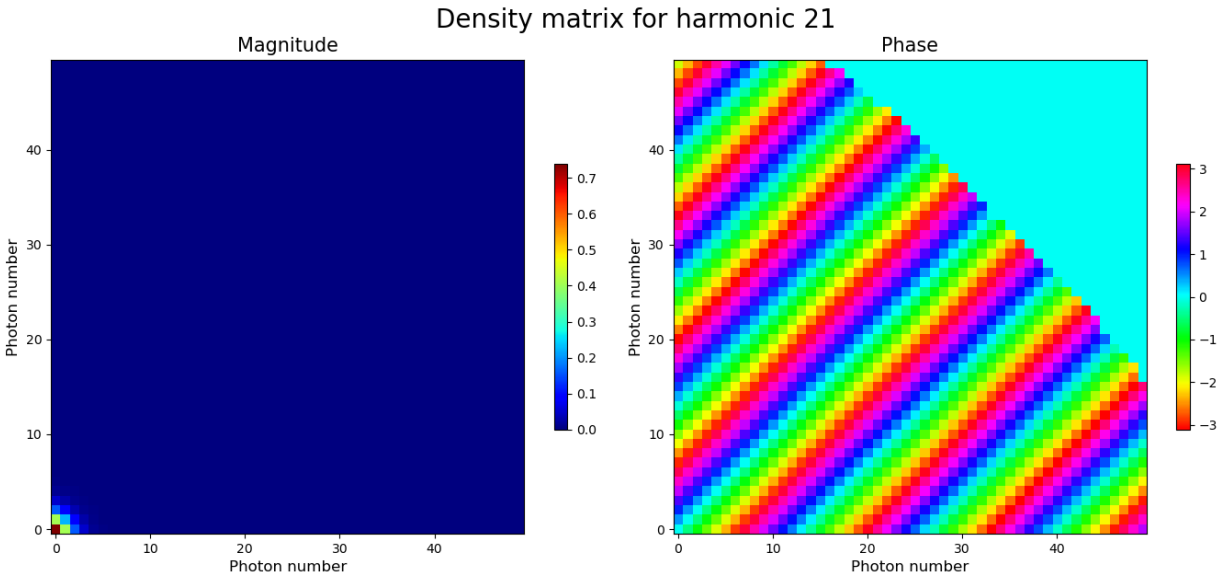

Figure C.47: a) Plot of the density matrix magnitudes. b) Plot of the density matrix phases.

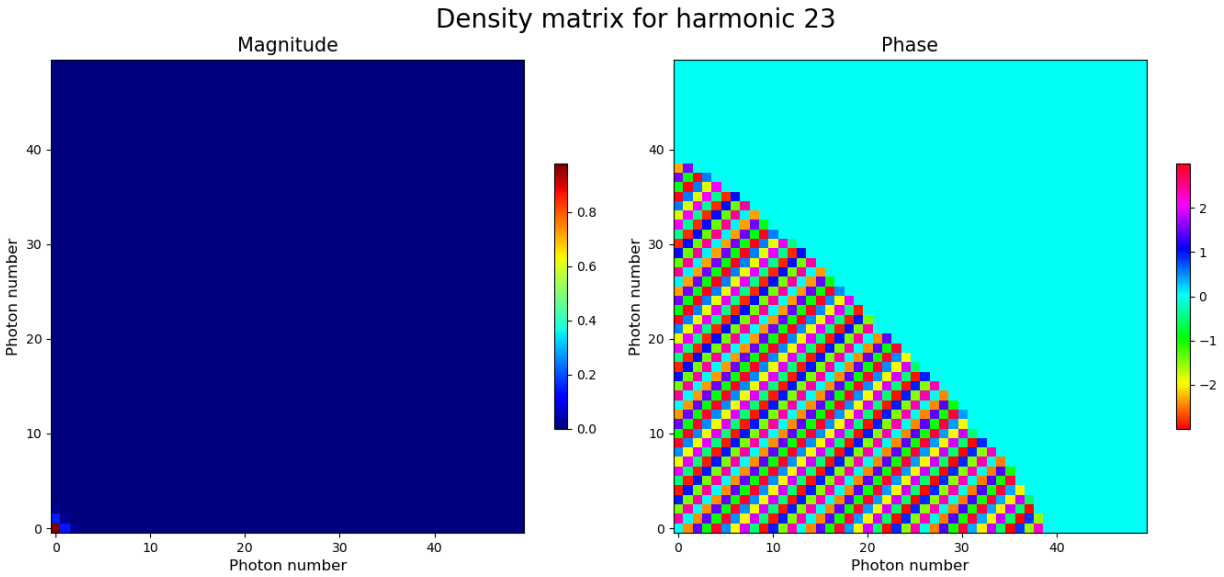

Figure C.48: a) Plot of the density matrix magnitudes. b) Plot of the density matrix phases.

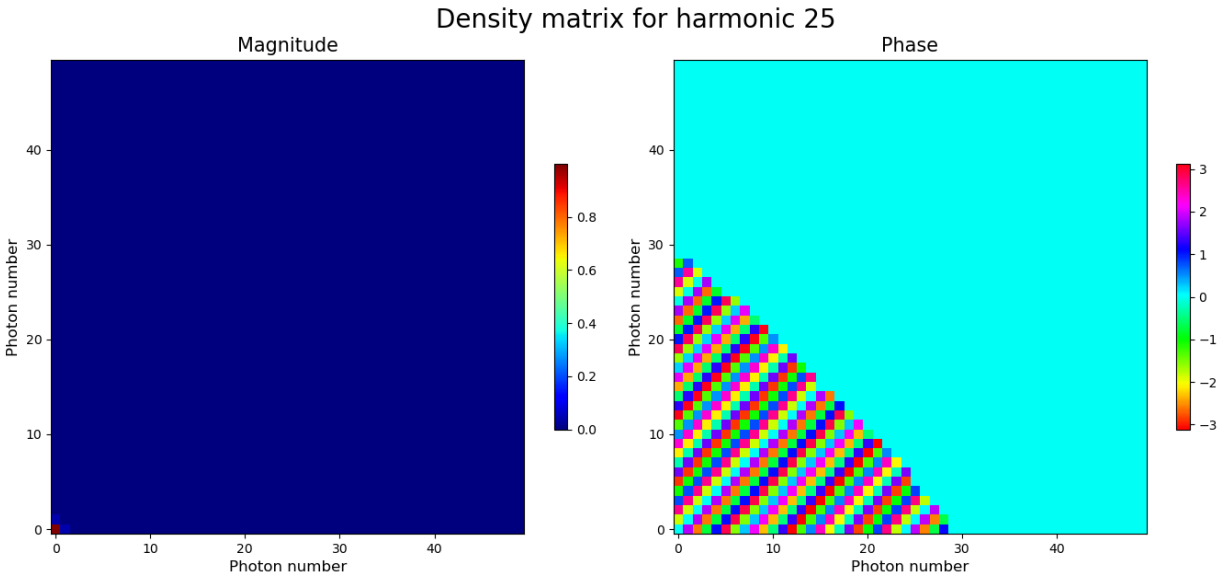

Figure C.49: a) Plot of the density matrix magnitudes. b) Plot of the density matrix phases.

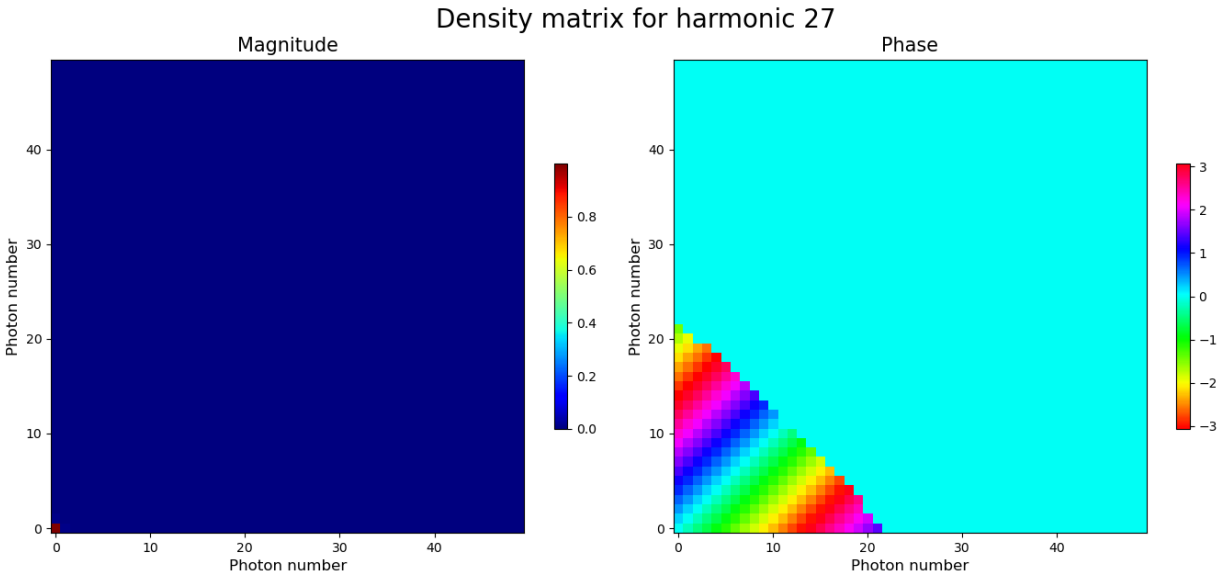

Figure C.50: a) Plot of the density matrix magnitudes. b) Plot of the density matrix phases.